THE MOTION OF IMMISCIBLE DROPS AND THE STABILITY OF ANNULAR FLOW

Thesis by

Bo Kyung Chi

In Partial Fulfillment of the Requirements

for the Degree of

Doctor of Philosophy

California Institute of Technology

Pasadena, California

1986

(Submitted May 19, 1986)

This thesis is dedicated to

my brother, Charlie.

Acknowledgment

I would like to express my sincere appreciation to my advisor Professor L. Gary Leal for suggesting this research topic and for his patient guidance and encouragement throughout the course of this investigation. I have greatly benefitted from my association with him and his research group. I wish to thank many friends for stimulating discussions and moral support during my stay in Caltech. My special thanks are due to Kathy Lewis for her excellent typing of this thesis. Finally, I would like to express my sincere gratitude to all members of my family for their never-ending support and encouragement. Without their care and sacrifice, my graduate education would have never come to a fruitful end.

Abstract

The creeping motion of a neutrally buoyant drop in Poiseuille flow is studied numerically using the boundary integral technique. The effects of the viscosity ratio, interfacial tension and drop size on steady shapes and velocities of the deformed drop are considered. Particular attention is given to cases involving large deformation which occurs when the interfacial tension becomes small. The critical value of the capillary number, for a given viscosity ratio, above which a steady shape for the drop does not exist is determined.

The stability of annular flow of two fluids of different viscosities through a circular tube is studied. The instability considered in the present study occurs at the interface between two fluids. Linear stability analysis is carried out for axisymmetric disturbances when the mechanisms of instability due to a viscosity difference between two fluids and interfacial tension are simultaneously present. The growth factor of instability is nonlinear in the viscosity ratio and the interfacial tension because the governing equations and boundary conditions are linearized with respect to a disturbance amplitude function, but not linearized with respect to the viscosity ratio and the interfacial tension. The effects of the viscosity ratio, interfacial tension, radius ratio and Reynolds number on the stability of the interface as well as the modes of maximum instability are studied.

Numerical study of the axisymmetric approach of a deformable drop toward a deformable interface under the action of a constant buoyancy force is carried out using the boundary integral technique. Unlike the previous film drainage theories, governing equations are applied in all fluids including the drop, lower bulk and upper bulk fluids. Therefore, physical properties of the drop fluid and the upper bulk fluid, which are neglected in the film drainage theories, are included in the present study. The influence of the viscosity ratio and interfacial tension is considered. Three distinct mechanisms of film drainage are identified: rapid drainage where the film between the drop and the interface is thinnest at the centerline and the film thickness increases with radial distance, uniform

drainage where the region of uniform film thickness appears and persists during further approach of the drop toward the interface, and dimpled drainage where the film is thinnest at a rim radius rather than at the centerline.

Table of Contents

Chapter I.

Numerical Studies of the Creeping Motion of a Drop in a Tube

NUMERICAL STUDIES OF THE CREEPING MOTION OF A DROP IN A TUBE

I. Introduction

The creeping motion of a neutrally buoyant drop in a straight tube is studied numerically using the boundary integral technique. The problem of droplet motion through straight or wavy-wall tubes is of general interest as one simple model for microscale phenomena in two-phase flow through a porous media. Indeed, one main motivation for the work reported here is the application to tertiary oil recovery where a micellar solution is injected into an oil reservoir to displace the residual oil left after secondary water flooding, by lowering the interfacial tension, σ, between oil droplets and the aqueous phase. We are concerned here with the limiting case in which interfacial tension is lowered to a point where the capillary number, $\mu u_c/\sigma$, characteristic of the drop motion becomes $O(1)$ or larger. Here, μ is the viscosity of the suspending fluid, u_c is the characteristic velocity of the drop, and σ is the interfacial tension between the drop and the suspending fluid.

A number of theoretical analyses of related problems have been done previously. Bretherton (1961) used the lubrication approximation to obtain the velocity of a long bubble in a tube filled with a viscous fluid. His analysis is valid for very small Ca of $O(10^{-3})$. Haberman and Sayer (1958) considered the case of a single spherical drop moving axisymmetrically in a tube. A first order correction to the shape, using the method of reflections, was obtained by Hetsroni et al. (1970). Shortly thereafter, Hyman and Skalak (1972a,b) considered an infinite row of equally spaced spherical and moderately deformed drops in an infinite, circular cylinder by numerical evaluation of a truncated infinite series of algebraic equations. However, as the ratio between the undeformed drop

radius and the tube radius, k, increases, the number of algebraic equations required for convergence becomes excessive even with the shape specified. Consequently, all of Hyman and Skalak's calculations were limited to $k \leq 0.8$. The restriction to moderate deformation in their solution restricts it to cases where $Ca < O(1)$.

On the experimental side, Ho and Leal (1975) studied the creeping motion of neutrally buoyant drops through a tube. Later, Olbricht and Leal (1982) extended the work of Ho and Leal by investigating the effect of a density difference between the drop and the suspending fluid. In both of these works, however, the range of parameters was rather limited. In particular,the viscosity ratio between the drop and the suspending fluid, λ, varied from 0.2 to 2.5 while Ca varied only from 0.1 to 0.34. Kung (1985) considered a larger range of parameters, but his studies were still limited in the sense that drops with Ca of $O(1)$ were considered for low viscosity ratios ($\lambda < 0.5$) only.

Previous experimental studies, reviewed briefly above, have shown that a drop suspended in a pressure-driven flow through a tube, becomes increasingly deformed as Ca is increased, while simultaneously its mobility relative to the fluid increases and the incremental pressure drop due to the presence of the drop decreases. However, the range of experimentally realized parameters with our flow system and readily available liquids was quite restricted. We are concerned here primarily with larger, $O(1)$, values of Ca. Our approach is to study the motion of a neutrally buoyant drop in Poiseuille flow numerically, using the boundary-integral method. Specifically, for three viscosity ratios of 0.1, 1 and 10, and several values of the drop size parameter k from 0.5 to 1.0, we investigate the effect of Ca on the deformation and mobility (velocity) of a drop for Ca as large as 4.0. One important objective is to determine whether critical value of Ca exists, for a given viscosity ratio, above which a steady shape for the drop

does not exist. The value of Ca at this critical point provides an estimate of the largest capillary number which can be attained in the motion of oil drops through porous media without risk of significant dispersion (or breakup).

II. Formulation

We consider a neutrally buoyant drop of viscosity μ_1 located concentrically in a circular tube filled with a second immiscible fluid of viscosity μ_2 (Fig. 1a). The drop moves due to a pressure-gradient driven Poiseuille flow in the tube. In the following analysis, we shall assume that the Reynolds number characteristic of the motion of the drop is very small so that the creeping motion approximation is applicable, i.e.

$$\mathrm{Re} = \frac{u_c \mathrm{Ro}}{\nu} << 1 ,$$

where a conservative estimate for u_c is the maximum Poiseuille velocity, Ro is the tube radius, and ν is the kinematic viscosity of the suspending fluid.

Thus, the equation of motion in dimensionless form reduces to

$$-\nabla p_1 + \lambda \nabla^2 \mathbf{u}_1 = 0$$

$$\text{for fluid 1} \qquad (1)$$

$$\nabla \cdot \mathbf{u}_1 = 0$$

$$-\nabla p_2 + \lambda \nabla^2 \mathbf{u}_2 = 0$$

$$\text{for fluid 2} \qquad (2)$$

$$\nabla \cdot \mathbf{u}_2 = 0$$

and these equations are to be solved subject to appropriate boundary conditions

on the drop interface and on the wall of the tube. The parameter, λ, in Eq. (1) denotes the ratio of the drop viscosity relative to the viscosity of the suspending fluid, and appears explicitly because the characteristic pressure p_c is chosen as $\mu_2 u_c/\sigma$ in both fluids.

On the drop surface, $\mathbf{x} \in S_D$, the boundary conditions can be expressed in the form

$$\mathbf{u}_1 = \mathbf{u}_2 \tag{3}$$

$$\mathbf{n}\cdot\mathbf{T}_2 - \lambda\mathbf{n}\cdot\mathbf{T}_1 = \mathbf{n}\,\frac{1}{Ca}\nabla\cdot\mathbf{n} \tag{4}$$

$$\mathbf{n}\cdot\left(\mathbf{u}_1 - \frac{dL}{dt}\,\mathbf{i}_z\right) = \mathbf{n}\cdot\left(\mathbf{u}_2 - \frac{dL}{dt}\,\mathbf{i}_z\right) = \frac{1}{|\nabla F|}\,\frac{\partial f}{\partial t}, \tag{5}$$

where Ca denotes the capillary number, $\mu_2 u_c/\sigma$. In writing Eq. (5), we have adopted a global coordinate system that is fixed relative to the tube. However, for convenience of describing the drop shape a local spherical coordinate system is utilized. The origin of this local spherical coordinate system is located at the center of mass of the drop and is related to the origin of the global coordinate system by L(t) as shown in Fig. 1a. Then, $\frac{dL}{dt}$ denotes the velocity of the center of mass of the drop. In Eq. (5), $\frac{dL}{dt}$ is included because the present problem is solved in the global coordinate system fixed on the tube. And the function f for drop shape is related to the position of its surface, as $\hat{r}_s = f(\hat{\theta},t)$. Here, $\hat{}$s denote the variables in the local spherical coordinate system. Of course, the drop shape is unknown and this must be determined as part of the solution. The quantity $\mathbf{n}$ that appears in (4) and (5) is the outer normal at the drop surface,

$$\mathbf{n} = \nabla F / |\nabla F|$$

where

$$F \equiv \hat{r}_s - f(\theta,t) .$$

On the tube surface, $\mathbf{x} \in S_T$, the no-slip boundary condition applies,

$$\mathbf{u}_2 = 0 . \tag{6}$$

Far away from the drop, $|\mathbf{x}| \to \infty$ upstream and downstream, the flow returns to its undisturbed form. Therefore,

$$\mathbf{u}_2 = \mathbf{u}_p , \quad |\mathbf{x}| \to \infty \quad \text{in the tube} \tag{7}$$

where $\mathbf{u}_p$ denotes the Poiseuille velocity profile.

Since the drop is assumed to be neutrally buoyant, a body force term does not appear in the governing equations or boundary conditions. It is important to realize that the solultion of Stokes Eqs. (1) and (2), subject to the boundary conditions (3)-(7), automatically satisfies the macroscopic condition of zero drag on the neutrally buoyant drop. In particular, the equations and boundary conditions stated above are sufficient to determine both the drop shape and the drop velocity, in addition to the velocity and pressure fields inside and outside the drop, without the necessity of explicit application of the macroscopic condition, $\mathbf{F}_o \equiv 0$. The fact that this latter condition is inherent in the basic equations and boundary conditions is demonstrated in the Appendix to this paper.

The governing equations and boundary conditions, (1)-(7), are solved using a boundary-integral method that we will describe shortly. For this procedure, the tube surface is described via a global circular cylindrical coordinate system. We have already indicated above that a local spherical coordinate system is utilized to describe the geometry of the drop surface, and this is adequate so long as the

deformation of the drop is not too extreme. When the drop becomes highly elongated, on the other hand, local spherical coordinates can be used to describe the upstream and downstream ends of the drop, but it is more convenient to adopt a local cylindrical coordinate system for description of the middle section as shown in Fig. 1b. In this case, the drop surface is described as $\hat{r} = h(\hat{z},t)$ and the outer normal at the drop surface is given as

$$\mathbf{n} = \nabla H / |\nabla H|$$

where $H = \hat{r} - h(\hat{z},t)$. The origin of all local coordinate systems is located at the center of mass of the drop and is related to the origin of the global coordinate system by L(t) as shown in Fig. 1a.

The problem, then, is to solve (1) and (2) subject to the boundary conditions (3)-(7). In addition to the two dimensionless parameters λ and Ca which appear explicitly in these equations and boundary conditions, a third dimensionless parameter of the system is

$$k = a/Ro$$

which provides a measure of drop size. The problem is both nonlinear and unsteady due to the boundary conditions (4) and (5), and the fact that the drop shape (and thus **n** and f) is unknown. However, the governing Stokes equations are linear. Therefore, we can represent a general solution of these equations in terms of a superposition of fundamental solutions corresponding to a distribution of point force singularities over the boundaries of the flow domain. Following earlier work in this group and elsewhere (cf. Lee and Leal 1982, or Geller, Lee and Leal 1985), we use the formulation of Ladyzhenskaya (1963) in which distributions of so-called single- and double-layer potentials are used at the boundaries of the fluid domain, in this case, for an arbitrary point **x** in one of the

fluids,

$$\mathbf{u}(\mathbf{x}) = \frac{1}{8\pi}\int_S \left[\frac{\mathbf{I}}{R} + \frac{(\mathbf{x}-\boldsymbol{\eta})(\mathbf{x}-\boldsymbol{\eta})}{R^3}\right]\cdot\mathbf{T}(\boldsymbol{\eta})\cdot\mathbf{n}dS_\eta$$

$$-\frac{3}{4\pi}\int_S \frac{(\mathbf{x}-\boldsymbol{\eta})(\mathbf{x}-\boldsymbol{\eta})(\mathbf{x}-\boldsymbol{\eta})}{R^5}\cdot\mathbf{u}(\boldsymbol{\eta})\cdot\mathbf{n}dS_\eta \qquad (8)$$

and

$$P(\mathbf{x}) = \frac{1}{2\pi}\int_S \left[\frac{\mathbf{I}}{R} - \frac{3(\mathbf{x}-\boldsymbol{\eta})(\mathbf{x}-\boldsymbol{\eta})}{R^5}\right]\cdot\mathbf{u}(\boldsymbol{\eta})\cdot\mathbf{n}dS_\eta$$

$$+\frac{1}{4\pi}\int_S \frac{(\mathbf{x}-\boldsymbol{\eta})}{R^3}\cdot\mathbf{T}(\boldsymbol{\eta})\cdot\mathbf{n}dS_\eta \qquad (9)$$

where $\boldsymbol{\eta}$ denotes a position on the bounding surface for the particular fluid $R = |\mathbf{x}-\boldsymbol{\eta}|$, and S represents the boundary of the fluid domain. Thus, in fluid 2, S includes both the drop and tube surfaces, while in fluid 1 S includes only the surface of the drop. As before, the outer normal to S is denoted as $\mathbf{n}$. To solve the problem posed in (1)-(7), we must determine the particular single- and double-layer distributions at the boundaries and the drop shape which satisfy the boundary conditions (3)-(7). In the Ladyzhenskaya's formula, the single- and double-layer distribution functions are just the velocity and stress components at the boundaries.

When the general solutions (8) and (9) are applied at the boundaries and the boundary conditions (3), (4), (6) and (7) are incorporated, we obtain integral equations for the velocity and stress components at the boundaries. As noted by earlier investigators, cf. Lee and Leal (1982), the double-layer potentials [the second terms in Eqs. (8) and (9)] are not continuous, but suffer a jump at the drop surface. If the double layer potential is defined by the function

$$\mathbf{W}(\mathbf{x}) = -\frac{3}{4\pi}\int_S \frac{(\mathbf{x}-\eta)(\mathbf{x}-\eta)(\mathbf{x}-\eta)}{R^5}\cdot\mathbf{u}\cdot\mathbf{n}dS_D\,, \tag{10}$$

the jump condition for the double-layer potential is expressed as

$$\mathbf{W}_i(\xi) = \frac{1}{2}\mathbf{u}(\xi) + \mathbf{W}_s(\xi) \tag{11}$$

$$\mathbf{W}_e(\xi) = -\frac{1}{2}\mathbf{u}(\xi) + \mathbf{W}_s(\xi) \tag{12}$$

where $\mathbf{W}_i(\xi)$ and $\mathbf{W}_e(\xi)$ denote, respectively, the limiting values of $\mathbf{W}(\xi)$ as $\xi\in S$ is approached from inside and outside the fluid domain, and $\mathbf{W}_s(\xi)$ is $\mathbf{W}(\xi)$ evaluated at $\mathbf{x} = \xi\in S$.

The general solutions (8) and (9) are applied at the boundaries using the jump conditions (11) and (12). First, applying (8) to fluid 1, we obtain for $\mathbf{x}\in S_D$,

$$\frac{1}{2}\lambda\mathbf{u}^D(\mathbf{x}) = \frac{1}{8\pi}\int_{S_D}\left[\frac{\mathbf{I}}{R} + \frac{\mathbf{rr}}{R^3}\right]\cdot\mathbf{T}_1^D(\eta)\cdot\mathbf{n}dS_d - \frac{3}{4\pi}\lambda\int_{S_D}\left[\frac{\mathbf{rrr}}{R^5}\right]\cdot\mathbf{u}^D(\eta)\cdot\mathbf{n}dS_d \tag{13}$$

where $\mathbf{r} = \mathbf{x} - \eta$, and subscripts and superscripts D indicate variables evaluated at the drop surface. $\mathbf{T}_1^D$ is the stress tensor evaluated as the drop surface is approached from fluid 1.

In order to apply the general solution (8) to fluid 2, it is convenient to define a disturbance velocity and stress

$$\mathbf{u}_2' = \mathbf{u}_2 - \mathbf{u}_p$$

$$\mathbf{T}_2^{T'} = \mathbf{T}_2^T - \mathbf{T}_{2p}^T\,,$$

where $\mathbf{T}_{2p}^T$ denotes the stress tensor associated with the Poiseuille velocity profile. Then, the boundary conditions (6) and (7) become

$$\mathbf{x}\in S_T\,,\quad \mathbf{u}_2' = 0 \tag{14}$$

$$|\mathbf{x}| \to \infty\,,\quad \mathbf{u}_2' = 0\,, \tag{15}$$

and it follows from (8) that the disturbance velocity for $\mathbf{x}$ in fluid 2 is

$$\mathbf{u}_2'(\mathbf{x}) = -\frac{1}{8\pi}\int_{S_D}\left[\frac{\mathbf{I}}{R}+\frac{\mathbf{rr}}{R^3}\right]\cdot\mathbf{T}_2^{D'}(\boldsymbol{\eta})\cdot\mathbf{n}dS_D - \frac{1}{8\pi}\int_{S_T}\left[\frac{\mathbf{I}}{R}+\frac{\mathbf{rr}}{R^3}\right]\cdot\mathbf{T}_2^{T'}(\boldsymbol{\eta})\cdot\mathbf{n}dS_T$$

$$+\frac{3}{4\pi}\int_{S_D}\left[\frac{\mathbf{rrr}}{R^5}\right]\cdot\mathbf{u}_2^{D'}(\boldsymbol{\eta})\cdot\mathbf{n}dS_D \tag{16}$$

where we have utilized the fact that $\mathbf{u}_2' = 0$ on the tube surface. Since $\mathbf{T}_{2p}(\mathbf{x})$ and $\mathbf{u}_p(\mathbf{x})$ have no singularity, we can apply the divergence theorem to (16) and integrate over the drop volume (Rallison and Acrivos, 1978) to obtain

$$\mathbf{u}_2(\mathbf{x}) = \mathbf{u}_{2p}(\mathbf{x}) - \frac{1}{8\pi}\int_{S_D}\left[\frac{\mathbf{I}}{R}+\frac{\mathbf{rr}}{R^3}\right]\cdot\mathbf{T}_2^{D}(\boldsymbol{\eta})\cdot\mathbf{n}dS_D - \frac{1}{8\pi}\int_{S_T}\left[\frac{\mathbf{I}}{R}+\frac{\mathbf{rr}}{R^3}\right]\cdot\mathbf{T}_2^{T}(\boldsymbol{\eta})\cdot\mathbf{n}dS_T$$

$$+\frac{3}{4\pi}\int_{S_D}\left[\frac{\mathbf{rrr}}{R^5}\right]\cdot\mathbf{u}_2^{D}(\boldsymbol{\eta})\cdot\mathbf{n}dS_D\,. \tag{17}$$

Applying the jump condition (11) to Eq. (17), we obtain for $\mathbf{x}\in S_D$,

$$\frac{1}{2}\lambda\mathbf{u}^D(\mathbf{x}) = \mathbf{u}_p^D(\mathbf{x}) - \frac{1}{8\pi}\int_{S_D}\left[\frac{\mathbf{I}}{R}+\frac{\mathbf{rr}}{R^3}\right]\cdot\mathbf{T}_2^{D}(\boldsymbol{\eta})\cdot\mathbf{n}dS_D - \frac{1}{8\pi}\int_{S_T}\left[\frac{\mathbf{I}}{R}+\frac{\mathbf{rr}}{R^3}\right]\cdot\mathbf{T}_2^{T}(\boldsymbol{\eta})\cdot\mathbf{n}dS_T$$

$$+\frac{3}{4\pi}\int_{S_D}\left[\frac{\mathbf{rrr}}{R^5}\right]\cdot\mathbf{u}_2^{D}(\boldsymbol{\eta})\cdot\mathbf{n}dS_D\,. \tag{18}$$

and for $\mathbf{x}\in S_T$,

$$0 = -\frac{1}{8\pi}\int_{S_D}\left[\frac{\mathbf{I}}{R}+\frac{\mathbf{rr}}{R^3}\right]\cdot\mathbf{T}_2^{D}(\boldsymbol{\eta})\cdot\mathbf{n}dS_D - \frac{1}{8\pi}\int_{S_T}\left[\frac{\mathbf{I}}{R}+\frac{\mathbf{rr}}{R^3}\right]\cdot\mathbf{T}_2^{T}(\boldsymbol{\eta})\cdot\mathbf{n}dS_T$$

$$+ \frac{3}{4\pi}\int_{S_D}\left[\frac{\mathbf{rrr}}{R^5}\right]\cdot\mathbf{u}_2^D(\eta)\cdot\mathbf{n}dS_D \,. \tag{19}$$

To eliminate $\mathbf{T}_1^D$, we can add (13) and (18) together and use the boundary condition (4). Then, we obtain

$$\frac{1}{2}(\lambda+1)\mathbf{u}^D(\mathbf{x}) = \mathbf{u}_p^D(\mathbf{x}) - \frac{1}{8\pi}\int_{S_D}\left[\frac{\mathbf{I}}{R}+\frac{\mathbf{rr}}{R^3}\right]\cdot\mathbf{Q}dS_D$$

$$+ \frac{3}{4\pi}(1-\lambda)\int_{S_D}\left[\frac{\mathbf{rrr}}{R^5}\right]\cdot\mathbf{u}^D(\eta)\cdot\mathbf{n}dS_D - \frac{1}{8\pi}\int_{S_T}\left[\frac{\mathbf{I}}{R}+\frac{\mathbf{rr}}{R^3}\right]\cdot\mathbf{T}_2^T(\eta)\cdot\mathbf{n}dS_T \tag{20}$$

where the function $\mathbf{Q}$ is the stress difference at the drop surface,

$$\mathbf{Q} = \mathbf{Q}(f) \equiv \mathbf{n}\cdot\mathbf{T}_2 - \lambda\mathbf{n}\cdot\mathbf{T}_1$$

$$= \mathbf{n}\,\frac{1}{Ca}\left\{\frac{K}{f}(3-K^2) - \frac{K}{f^2}\left[\frac{\cos\hat{\theta}}{\sin\hat{\theta}}\left(\frac{\partial f}{\partial\hat{\theta}}\right) + K^2\left(\frac{\partial^2 f}{\partial\hat{\theta}^2}\right)\right]\right\} \tag{21a}$$

with

$$K = \frac{1}{\left[1+\frac{1}{f^2}\left(\frac{\partial f}{\partial\hat{\theta}}\right)^2\right]^{1/2}}$$

for spherical coordinate, or

$$\mathbf{Q} = \mathbf{Q}(h) \equiv \mathbf{n}\cdot\mathbf{T}_2 - \lambda\mathbf{n}\cdot\mathbf{T}_1 = \mathbf{n}\,\frac{1}{Ca}\left\{\frac{K}{h} - K^3\left(\frac{\partial^2 h}{\partial\hat{z}^2}\right)\right\} \tag{21b}$$

with

$$K = \frac{1}{\left[1+\left(\frac{\partial h}{\partial\hat{z}}\right)^2\right]^{1/2}}$$

for cylindrical coordinate.

In order to calculate the steady-shape of the drop, we begin with an initial shape — either a sphere or the shape obtained previously with nearby values of the parameters. With the initial shape prescribed, Eq. (21) is used to evaluate the stress difference at the drop surface and Eqs. (18)-(20) are solved to obtain $\mathbf{u}^D$, $\mathbf{T}_2^D$ and $\mathbf{T}_2^T$. The resulting solution satisfies the original Stokes equations (1) and (2), plus the conditions (3) and (4) at the drop surface and (6) and (7) at the tube walls and far from the drop. All that remains is the kinematic condition (5), which can be used to increment the drop shape to a time Δt later. In the limit, as a steady solution is achieved, the left-hand side of (5), calculated using $\mathbf{u}^D$, vanishes.

The kinematic condition (5) is applied in the approximate form

$$f_{j+1} = f_j + \left[\left(\mathbf{u}_j^D - \frac{L_{j+1} - L_j}{\Delta t}\,\mathbf{i}_z\right)\cdot\mathbf{n}_j\right]\Delta t\,\frac{1}{K_j}\,. \tag{22}$$

In Eq. (22), the variables with the subscript j are known quantities at the jth time step. Of course, L_{j+1} must be known before Eq. (22) can be used to obtain a new shape. L_{j+1} is determined by the condition that the origin of the local coordinate system used to describe the drop shape is located at the center of mass of the drop at every time step. Then,

$$\hat{z}_0 = 0 = \frac{\int \rho \hat{z}\, dV_D}{\int \rho\, dV_D} \tag{23}$$

where $\hat{z}_0$ denotes the center of mass in the local coordinate system. For constant density, ρ, Eq. (23) can be stated in the form

$$0 = \int \hat{z}\, dV_D\,. \tag{24}$$

In the local spherical coordinate system, Eq. (24) becomes, integrating in azimuthal direction,

$$0 = 2\pi \int_{\hat{\theta}=0}^{\pi} \int_{\hat{r}_s=0}^{f} \hat{r}_s^3 \cos\hat{\theta}\sin\hat{\theta} d\hat{\theta} d\hat{r}_s \tag{25}$$

Letting $\hat{\eta} = \cos\hat{\theta}$, Eq. (25) becomes

$$0 = \frac{2\pi}{4} \int_{\hat{\eta}=-1}^{1} f^4 \hat{\eta} d\hat{\eta} \tag{26}$$

Equation (26) must be satisfied at every time step,

$$0 = \int_{\hat{\eta}=-1}^{1} f_j^4 \hat{\eta} d\hat{\eta} = \int_{\hat{\eta}=-1}^{1} f_{j+1}^4 \hat{\eta} d\hat{\eta} \tag{27}$$

Then, at j+1th time step,

$$0 = \int_{\hat{\eta}=-1}^{1} (f_j + \Delta f_j)^4 \hat{\eta} d\hat{\eta} \tag{28}$$

where

$$\Delta f_j = \frac{1}{K_j} \left(\mathbf{u}_j^p - \frac{L_{j+1} - L_j}{\Delta t} \mathbf{i}_z \right) \cdot \mathbf{n}_j \Delta t$$

as given by the kinematic condition in Eq. (22). Then, L_{j+1} is determined by satisfying Eq. (28).

The volume of the drop was conserved at each time step by calculating the volume of the drop and adjusting $f(\hat{\theta})$ and/or $h(\hat{t})$ to keep the constant dimensionless volume of $\frac{4}{3}\pi k^3$.

Since we are considering a concentrically located neutrally buoyant drop in a tube, the problem is axisymmetric. Thus, Eqs. (18)-(20) can be integrated analytically in the aximuthal direction, and the surface integrals transformed to the line integrals. Thus, for axisymmetric flows, Eqs. (18)-(20) become

$$\frac{1}{2} \begin{bmatrix} u_r^p(\mathbf{x}) \\ u_z^p(\mathbf{x}) \end{bmatrix} = \begin{bmatrix} 0 \\ u_p^p(\mathbf{x}) \end{bmatrix} - \frac{1}{8\pi} \int_{S_p} \mathbf{B}(\mathbf{x} - \eta) \cdot \begin{bmatrix} T_{nr}^p \\ T_{nz}^p \end{bmatrix} dl_p$$

$$- \frac{1}{8\pi} \int_{S_T} \mathbf{B}(\mathbf{x},\eta) \cdot \begin{bmatrix} T^T_{nr} \\ T^T_{nz} \end{bmatrix} dl_T + \frac{3}{4\pi} \int_{S_D} \mathbf{C}(\mathbf{x},\eta) \cdot \begin{bmatrix} u^D_r \\ u^D_z \end{bmatrix} dl_D \tag{29}$$

$$\begin{bmatrix} 0 \\ 0 \end{bmatrix} = - \frac{1}{8\pi} \int_{S_D} \mathbf{B}(\mathbf{x},\eta) \cdot \begin{bmatrix} T^D_{nr} \\ T^D_{nz} \end{bmatrix} dl_D - \frac{1}{8\pi} \int_{S_T} \mathbf{B}(\mathbf{x},\eta) \cdot \begin{bmatrix} T^T_{nr} \\ T^T_{nz} \end{bmatrix} dl_T$$

$$+ \frac{3}{4\pi} \int_{S_D} \mathbf{C}(\mathbf{x},\eta) \cdot \begin{bmatrix} u^D_r \\ u^D_z \end{bmatrix} dl_D \tag{30}$$

$$\frac{1}{2}(\lambda + 1) \begin{bmatrix} u^D_r(\mathbf{x}) \\ u^D_z(\mathbf{x}) \end{bmatrix} = \begin{bmatrix} 0 \\ u^D_p(\mathbf{x}) \end{bmatrix} - \frac{1}{8\pi} \int_{S_D} \mathbf{B}(\mathbf{x},\eta) \cdot \begin{bmatrix} Q_r \\ Q_z \end{bmatrix} dl_D$$

$$- \frac{1}{8\pi} \int_{S_T} \mathbf{B}(\mathbf{x},\eta) \cdot \begin{bmatrix} T^T_{nr} \\ T^T_{nz} \end{bmatrix} dl_T + \frac{3}{4\pi}(1 - \lambda) \int_{S_D} \mathbf{C}(\mathbf{x},\eta) \cdot \begin{bmatrix} u^D_r \\ u^D_z \end{bmatrix} dl_D \,. \tag{31}$$

where

$$dl_D = f\sin\hat{\theta}\left[f^2 + \left(\frac{\partial f}{\partial \hat{\theta}}\right)^2\right]^{1/2} d\hat{\theta} \quad \text{for spherical coordinate}$$

$$= h\left[1 + \left(\frac{\partial h}{\partial \hat{z}}\right)^2\right]^{1/2} d\hat{z} \quad \text{for cylindrical coordinate}$$

and

$$dl_T = dz \,.$$

Here, **B** and **C** are tensors whose elements consist of elliptic integrals.

$$\mathbf{B}(\mathbf{x},\eta) = \begin{bmatrix} B_{rr} & B_{rz} \\ B_{zr} & B_{zz} \end{bmatrix} \quad \mathbf{C}(\mathbf{x},\eta) = \begin{bmatrix} C_{rr} & C_{rz} \\ C_{zr} & C_{zz} \end{bmatrix} .$$

The elements of **B** and **C** are given by Lee and Leal (1982).

Examination of (29)-(31) shows that there are six linear integral equations, (29)-(30), for six unknown functions, u^D_r, u^D_z, T^D_{nr}, T^D_{nz}, T^T_{nr} and T^T_{nz}.

As in the works of Lee and Leal (1982) and Geller, Lee and Leal (1985), a collocation method was used to convert the integral equations to a system of linear algebraic equations. In particular, the drop and tube surfaces were divided into small elements, with $\mathbf{u}^D$, $\mathbf{T}^D$ and $\mathbf{T}^T$ approximated in an element by their values at the center of the element. By this means, we obtain a system of $(4N_D + 2N_T)$ linear algebraic equations where N_D and N_T denote the number of elements on the drop surface and the tube surface, respectively. The integral coefficients which result from Eqs. (29)-(31) were evaluated by Gaussian quadrature, and the resulting system of linear algebraic equations was solved by Gaussian elimination. When $\mathbf{x} = \boldsymbol{\eta}$, the integrands in (18)-(20) become singular. However, finite values for the integrals were obtained by analytically integrating over a small neighborhood of $\mathbf{x} = \boldsymbol{\eta}$ using a linear expansion of the integrands about $\mathbf{x} = \eta$.

III. Preliminary Calculations

When the collocation method is applied to the integral Eqs. (23)-(25), the domain must be truncated at some large, but finite distance from the center of mass of the drop. A similar truncation was used earlier by Lee and Leal (1982) for the case of a solid sphere approaching an infinite plane interface to limit the collocation to a large but finite region of the interface around the centerline that passes through the center of mass of the solid sphere. To illustrate the effect in the present case of truncating the domain at different distances, z_0, from the center of the drop, we ran a number of test calculations for the representative case of a spherical drop in a tube with k = 0.7, Ca = 0.2 and λ = 10.0. It can be seen in Fig. 2 that $\left\| \left(\mathbf{u}^D - \frac{dL}{dt} \mathbf{i}_z \right) \cdot \mathbf{n} \right|_{max}$ at the drop surface does not vary significantly beyond $z_0 = 9$. For larger drops, i.e. for larger k, larger values of z_0 were used to insure comparable accuracy. In addition, as the drop became elongated due to viscous forces for finite values of Ca, larger values of z_0

were used in the calculation. Typically, z_0 was assigned values between 9 and 13.

As noted earlier, the tube surface and the drop surface were discretized into small elements in which $\mathbf{u}^D$,$\mathbf{T}_D$ and $\mathbf{T}^{T'}$ are assumed to be constant. On the tube wall, the region close to the drop was discretized with smaller elements, and larger elements were used as the distance from the drop increased. Non-uniform elements were also employed on the drop surface depending on its shape. For an initial spherical drop, uniform elements in θ were used, but as the drop deformed, more elements were employed in regions where $\mathbf{u}^D$,$\mathbf{T}^D$ varied most rapidly with position. Taking a spherical drop with k = 0.95, Ca = 0.2 and λ = 10, the effect of varying N_D is shown in Fig. 3 where $\left|\left(\mathbf{u}^D - \frac{dL}{dt}\mathbf{i}_z\right)\cdot\mathbf{n}\right|_{max}$ at the drop surface is plotted against N_D. It can be seen that N_D = 20 is sufficient to give accurate results in this case. Starting with N_D = 20, more elements were added as the drop became significantly deformed.

We have indicated earlier, that the drop shape was changed using the kinematic condition (22) in the form

$$f_{j+1} = f_j + \left[\left(\mathbf{u}_j^D - \frac{L_{j+1} - L_j}{\Delta t}\mathbf{i}_z\right)\cdot\mathbf{n}_j\right]\frac{1}{K_j}\Delta t \qquad (26)$$

The time increment Δt was chosen so that $(f_{j+1} - f_j)/f_j < 0.005$ for each time step in order to avoid large changes in the shape for any one step. The above criterion was found empirically to insure the stability of the numerical method. Typically Δt varied from 0.02 at the initial stage of a calculation to 0.2 as a steady shape was approached. The calculation was terminated, and the shape was assumed to have reached steady-state when $\left|\left(\mathbf{u}^D - \frac{dL}{dt}\mathbf{i}_z\right)\cdot\mathbf{n}\right| < 10^{-3}$ everywhere on the drop surface.

IV. Comparison with Previous Results

Calculations were initially done for a solid sphere and a spherical drop suspended in Poiseuille flow to compare the velocities obtained via the present numerical technique with existing theoretical results. In Fig. 4, the velocity of a solid sphere is plotted against k. As the sphere size increases, its velocity decreases due to the increase of the wall effect. The calculated result agrees very well with the theoretical results of Haberman and Sayer (1958) and Wang and Skalak (1969). Similarly, in Fig. 5, the velocity of a spherical drop is plotted against k for λ = 1, 10 and 40. Comparison between the current results and the theoretical results of Hyman and Skalak (1972a) is again very good. The case of λ = 40 nearly coincides with the results for the solid sphere in Fig. 4. It can also be seen that less viscous drops move faster than more viscous drops for the same value of k.

Two calculations were also done to compare current results with existing experimental results. First, in Fig. 6a, we show a comparison between the predicted steady-state drop shape and a photographic result of Ho and Leal (1975) for the case k = 0.726, Ca = 0.356, λ = 0.93. It can be seen from the figure that the comparison between the shapes is quite good. The calculated velocity of the drop is 0.768 which is also in good agreement with the experimental value, 0.765, reported by Ho and Leal. Second, in Fig. 6b, the shape predicted in the current calculation for k = 0.7, Ca = 3, λ = 0.1 is compared with a photograph from Kung (1985) for which k = 0.7, Ca = 2.6, λ = 0.047. Again the agreement is excellent.

V. Results

In the current study, our goal is to determine the effects of Ca, λ and k on drop shapes and drop velocities. As mentioned previously, we are particularly concerned with cases for which Ca $\geq$ O(1). In Fig. 7, calculated drop shapes are

shown for various values of Ca and λ= 0.1, 1, 10 for k = 0.7. Taking a sphere as the initial shape for Ca = 0, the steady shape for Ca = 0.2 was calculated using the procedure described above. Then, the steady shape for Ca = 0.5 was calculated using the result for Ca = 0.2 as an initial condition, and so on. Drop shapes for various values of k with Ca = 1 and λ = 1 are shown in Fig. 11. In this case, each solution was obtained using the shape for the next smaller value of k as an initial condition. The effect of varying k for a number of additional values of Ca is shown in Fig. 12 where drop shapes are drawn for k = 0.7 and 0.95 with Ca = 0.2, 1.0, 2.0 and 3.0. Drop shapes in Fig. 12 for k = 0.95 and k = 0.7 were obtained by increasing Ca starting from a spherical shape for each value of k.

A. Drop Shape

In the following part of this section, we consider the effects of Ca and λ on the drop shape in more detail.

1. Effect of Ca

As can be seen in Fig. 7, the drop elongates in the axial direction and consequently the maximum width of the drop decreases as Ca increases for all λ. This elongation of the drop is a consequence of the increase in viscous forces relative to interfacial forces as Ca increases. A similar elongation of the drop was also observed in the experiments of Ho and Leal (1975) for Ca up to a maximun value of 0.34. As Ca increases beyond 1.0, an indentation appears at the back of the drop which becomes increasingly significant as Ca increases. Since the detailed modes of deformation are somewhat different for the different viscosity ratios, it is useful to consider each of the three values λ = 0.1, 1 and 10 separately.

The case λ = 1.0 is considered first. In this case, as Ca increases, the drop elongates and the rear of the drop flattens until the indentation occurs at the rear of the drop for Ca > 1.0. As the drop elongates the maximum width occurs

at the rear of the drop, not at the middle section of the drop as for an undeformed spherical drop. In fact, the middle section of the drop becomes almost straight and parallel to the tube wall, while the front of the drop becomes more pointed as Ca is increased. *Perhaps the most important fact, however, is that no steady shape could be obtained for Ca > 3.2.* For larger values of Ca, the drop was found to elongate continuously in the axial direction with a waist developing in the middle.

The velocity distribution in the suspending fluid is shown in Fig. 8 in a frame of reference that moves with the drop for k = 0.7, Ca = 2.0 and λ = 1.0. The fluid sufficiently far from the drop flows almost unidirectionally. The drop moves slower than the maximum velocity of Poiseille flow. Therefore, in a frame of reference moving with the drop, the axial velocity is in the positive z-direction in the center core of the tube and is in the negative z-direction for the rest of the tube. It is this forward velocity at the center core of the tube which leads to the indentation at the rear of the drop when the interfacial force can no longer resist viscous forces as Ca increases.

When λ = 0.1, the drop also elongates as Ca increases, like the case of λ = 1.0. In this case, however, the drop shape beyond Ca ~ 1.0 becomes approximately prolate spheroidal with an indentation at the rear of the drop. In particular, the maximum width of the drop moves toward the middle of the drop as the drop becomes increasingly elongated. As Ca increases, the curvature of the rim at the rear becomes increasingly large. As a consequence, the calculation was terminated at Ca = 4.0. In this case, however, the termination point does not correspond to a critical point for loss of steady state solutions as was true for λ = 1, but exists because of resolution difficulties in the region of high curvature for large values of Ca. The predicted indentation at the rear of the drop was also observed experimentally by Kung (1985) for λ = 0.047. Reproductions of

three of their photographs are shown in Fig. 9. Since the photographs were taken with a side view, the indentation at the rear is difficult to discern for Ca < 2.6. But the shape of the drop coincides well with the shape obtained numerically. The experimental pictures of Kung (1985) for Ca = 4.4 and 5.4 show that the drops lose axisymmetry as Ca is increased to these values. Due to the loss of axisymmetry, the indentation at the rear is more rapidly apparent. It is not clear whether this experimental loss of axisymmetry is an intrinsic property of the flow at such high Ca or is caused by slight deviations in matching the densities of the drop and suspending fluid.

Finally, for $\lambda = 10$, the series of shapes shown in Fig. 7 is qualitatively similar to those for $\lambda = 1$, though the degree of deformation is somewhat greater for Ca = 0.8 and 1.0. *Indeed, in this case, the calculation was terminated at Ca = 1 because we were not able to obtain a steady shape for larger values of Ca.* Attempts to obtain such solutions showed that the drop simply continued to elongate in the axial direction, with a waist developing in the middle like the case of $\lambda = 1.0$. It is evident, then, that a critical value of Ca exists beyond which the drop can no longer exist in a steady configuration. The critical value of Ca appears to decrease monotonically with increase of the viscosity ratio, λ, at least based upon the three values 0.1, 1.0 and 10 that we studied here. It may be expected that the critical values of Ca will also depend upon the drop size, k.

2. Effect of λ

The effect of λ on the drop shape can be discerned qualitatively from Fig. 7. A more quantitative indication of the effect of λ is shown in Fig. 10 where we plot the drop length of the deformed drops against λ for Ca = 0.2, 0.5, 0.8 and 1.0. For Ca = 0.2 and 0.5, the drop length exhibits a weak maximum near $\lambda = 1.0$. However, for Ca = 0.8, 1.0, the drop length increases monotonically as λ

increases over the range of values of λ that we have considered. The implication of these limited results is that the critical λ, λ_e, where the drop length is a maximum must increase with increase of Ca. For the larger values of Ca, the drop becomes increasingly elongated as λ increases and consequently the maximum width becomes smaller. This effect of λ on the elongation of the drop was also observed in the experiment of Ho and Leal (1975).

3. Effect of k

The effects of variations in the drop size parameter k on the drop shapes are shown in Figs. 11 and 12 for Ca = 1, λ = 1 and Ca = 0.2, 1, 2, 3 and λ = 0.1, respectively. When there is no wall effect, i.e. k $\rightarrow$ 0, the drop remains as a sphere as shown by Hadamard (1911) and Rybczynski (1911) for creeping flow of a drop in an unbounded uniform flow. However, as k increases, the increase in the wall effect causes the drop to become increasingly deformed. The drop shapes for Ca = 1, λ = 1 are shown in Fig. 11 as k increases from 0.5 to 1.0. The drop becomes more elongated in the axial direction as k increases. Beyond k=0.7, however, the maximum width of the drop remains constant and the upstream and downstream sections of the drop retain the same shapes. Thus, the effect of increasing k is to simply increase the length of the straight section in the middle of the drop. For the cases with higher Ca (Ca > 1), shown in Fig. 12 for λ = 0.1, the drop becomes more elongated as k increases as in the case of Ca = 1 and λ = 1, and the indentation at the rear becomes more significant.

B. Drop Velocity

The effect of k on the drop velocity is shown in Fig. 13 for Ca = 1 and λ = 1 as k varies from 0.5 to 1.0. The drop velocity decreases monotonically as k increases from 0.5 up to 0.7. However, with further increase of k, the drop velocity becomes independent of k because, as Fig. 13 shows, the maximum width of

the drop becomes almost constant for $k > 0.7$. This apparent correlation between the drop velocity and the maximum width of the drop was also observed by Ho and Leal (1975), who noted that the velocity of the drop with the largest experimental value of Ca (0.34) became practically independent of k as k increased beyond 0.9 because the maximum width of the drop did not change beyond $k \sim 0.9$.

The effect of Ca and λ on the drop velocity is shown in Fig. 14 for $k = 0.7$. As λ increases, the drop velocity decreases. This effect of λ on the drop velocity is in agreement with the experimental results of Ho and Leal (1975). The variation of the drop velocity with Ca is more interesting. For $\lambda = 0.1$, as Ca increases, the drop velocity approaches an asymptotic limit of about 1, the maximum of the Poiseuille flow. For $\lambda = 1$, on the other hand, the same trend can be seen in the sense that the velocity of the drop approaches an asymptotic value for sufficiently large Ca, but in this case the limiting value is about 0.91. As Ca increases for fixed λ, the rate of the decrease in the maximum width of the drop decreases in all cases as can be seen in Fig. 15. Thus, although a clear asymptote was only found for $\lambda = 0.1$ (and perhaps $\lambda = 1.0$), it is obvious that maximum width of the drop will approach some asymptotic value in all cases. Since the drop velocity depends on the maximum width of the drop, as mentioned earlier, the drop velocity also approaches an asymptotic value as Ca increases.

VI. Conclusions

The creeping motion of a neutrally buoyant drop in a tube has been studied using the boundary integral technique. Steady shapes and velocities of the deformed drop are presented as Ca, λ and k vary. Particular attention is given to cases involving large deformation which occurs when $Ca = O(1)$.

We have shown that the modes of deformation are different for different viscosity ratios. When $\lambda = 0.1$, as Ca increases beyond $\sim$ 1.0, the drop shape becomes approximately prolate spheroidal with an indentation at the rear of the drop which becomes more significant as Ca increases. The curvature of the rim at the rear correspondingly increases as Ca increases further up to 4.0, the maximum value we could achieve due to difficulty with numerical resolution in the region of high curvature. For $\lambda = 1.0$ and 10.0, on the other hand, the drop elongates as Ca increases, and the rear of the drop flattens with the indentation occurring at the rear of the drop for $Ca > 1.0$. However, in these cases, the middle section becomes straight as Ca increases until a waist develops for $Ca > 3.2$ and $Ca > 1.0$, respectively, for $\lambda = 1.0$ and 10.0, and no further steady shapes are possible. As Ca increases for fixed λ, the maximum width of the drop approaches some asymptotic value, and consequently the drop velocity approaches an asymptotic value.

Acknowledgement: This work was supported by a grant from the Fluid Mechanics program of the National Science Foundation.

Appendix

In dimensional form, Eq. (4) is

$$\mathbf{n}\cdot\mathbf{T}_2 - \mathbf{n}\cdot\mathbf{T}_1 = \gamma\nabla\cdot\mathbf{n}\mathbf{I}\cdot\mathbf{n} \tag{A1}$$

Rearranging Eq. (A1), we obtain

$$\mathbf{n}\cdot\mathbf{T}_2 = \mathbf{n}\cdot\mathbf{T}_1 + \gamma\nabla\cdot\mathbf{n}\mathbf{n} \tag{A2}$$

The drag force on the drop is

$$\mathbf{F}_D = \int \mathbf{n}\cdot\mathbf{T}_2 dS_D = \int \mathbf{n}\cdot\mathbf{T}_1 dS_D + \int \gamma\nabla\cdot\mathbf{n}\mathbf{n} dS_D . \tag{A3}$$

Applying the divergence theorem to the first term on the RHS of Eq. (A3), it may be shown that

$$\int \mathbf{n}\cdot\mathbf{T}_1 dS_D = \int \nabla\cdot\mathbf{T}_1 dV_D = 0 \tag{A4}$$

because

$$\nabla\cdot\mathbf{T}_1 = 0$$

for the Stokes approximation.

The second term on the RHS of Eq. (A3) can be evaluated by means of the surface divergence theorem which states that for any scalar function φ on a surface S

$$\int \varphi(\nabla\cdot\mathbf{n})\mathbf{n} dS = \int \nabla\varphi dS - \int_c \varphi\mathbf{t} dl \tag{A5}$$

where c denotes any closed curve on the surface S, and $\mathbf{t}$ denotes the unit vector that is normal to the curve c and tangent to the surface at each point. Then, by applying the surface divergence theorem, the second term on the RHS of Eq. (A3)

$$\int \gamma(\nabla \cdot \mathbf{n})\mathbf{n} dS_D = \int \nabla \gamma dS_D - \int_c \gamma \mathbf{t} dl \ . \tag{A6}$$

The first term of the RHS of Eq. (A6) is zero because $\nabla \gamma = 0$ for constant γ, and the second term of the RHS of Eq. (A6) is zero because

$$\int_c \gamma \mathbf{t} dl = 0$$

for a closed volume. Therefore, the above result confirms the fact that solutions of Stokes equations subject to the stress conditions in Eq. (4) will automatically satisfy the condition of zero drag force on the drop.

References

Bretherton, F. P. 1961 The motion of long bubbles in tubes. J. Fluid Mech. **10**, 537.

Geller, A. W., Lee, S. H. and Leal, L. G. 1985 The creeping motion of a spherical particle to a deformable interface. J. Fluid Mech. (accepted).

Haberman, W. L. and Sayer, R. M. 1958 Motion of rigid and fluid spheres in stationary and moving liquids inside cylindrical tubes. David Taylor Model Basin Report No. 1143, Washington, D.C.

Hadamard, J. S. 1911 Compt. Rend. Acad. Sci. **152**, 1735.

Hetsroni, G., Haber, S. and Wacholder, E. 1970 The flow field in and around a droplet moving axially within a tube. J. Fluid Mech. **41**, 689.

Ho, B. P. and Leal, L. G. 1975 The creeping motion of liquid drops through a circular tube of comparable diameter. J. Fluid Mech. **71**, 361.

Hyman, W. A. and Skalak, R. 1972a Viscous flow of a suspension of liquid drops in a cylindrical tube. Appl. Sci. Res. **26**, 27.

Hyman, W. A. and Skalak, R. 1972b Non-Newtonian behavior of a suspension of liquid drops in a tube flow. A.I.Ch.E. **18**, 149.

Kung, D. 1985 PhD Thesis, Cornell University.

Ladyzhenskaya, O. A. 1963 The mathematical theory of viscous incompressible flow. Gordon and Breack, New York.

Lee, S. H. and Leal, L. G. 1982 Motion of a sphere in the presence of a deformable interface. Part 2: Numerical study of the translation of a sphere normal to an interface. J. Coll. Int. Sci. **87**, 81.

Olbricht, W. L. and Leal, L. G. 1982 The creeping motion of liquid drops through a circular tube of comparable diameter: The effect of density difference between fluids. J. Fluid Mech. **115**, 187.

Rallison, J. M. and Acrivos, A. 1978 A numerical study of the deformation and burst of a viscous drop in an extensional flow. J. Fluid Mech. **89**, 191.

Rybczynski, W. 1911 Bull. Acad. Sci. Cracovi, A 40.

Wang, H. and Skalak, R. 1969 Viscous flow in a cylindrical tube containing a line of spherical particles. J. Fluid Mech. **38**, 75.

Figure Captions

Figure 1a: Description of the coordinate systems. O_L, origin of the local coordinate systems; O_G, origin of the global coordinate systems.

Figure 1b: Description of the drop shape for an elongated drop.

Figure 2: Maximum absolute value of the dimensionless normal velocity on the drop, $\left|\left(\mathbf{u}^D - \frac{dL}{dt}\mathbf{i}_z\right)\cdot\mathbf{n}\right|_{max}$, as a function of the truncated dimensionless distance on the tube from the center of mass of the drop z_D.

Figure 3: Maximum absolute value of the dimensionless normal velocity on the drop, $\left|\left(\mathbf{u}^D - \frac{dL}{dt}\mathbf{i}_z\right)\cdot\mathbf{n}\right|_{max}$, as a function of the number of elements on the drop surface, N_D.

Figure 4: Dimensionless particle velocity as a function of the dimensionless particle radius for a spherical particle in a tube.

Figure 5: Dimensionless drop velocity as a function of the dimensionless drop radius for a spherical drop in a tube.

Figure 6: Comparison of the calculated drop shapes with the experimental photographs.

Figure 7: Comparison drop shapes for various values of Ca and λ = 0.1, 1, 10 for k = 0.7.

Figure 8: Velocity distribution in the suspending fluid for k = 0.7, Ca = 2.0, λ = 1.0.

Figure 9: Experimental photographs of Kung (1985) for k = 0.7, λ = 0.047 and Ca = 2.6, 4.4 and 5.4.

Figure 10: Dimensionless maximum length of the drop as a function of the viscosity ratio, λ.

Figure 11: Calculated drop shapes for various values of k for Ca = 1, λ = 1.

Figure 12: Calculated drop shapes λ = 0.1, Ca = 0.2, 1, 2 and 3; ---- for k = 0.7; —— for k = 0.95.

Figure 13: Dimensionless maximum width of the drop and the dimensionless drop velocity, $\frac{dL}{dt}$, as a function of the dimensionless drop size k for Ca = 1, λ = 1.

Figure 14: Dimensionless drop velocity $\frac{dL}{dt}$ as a function of the Capillary number Ca for = 0.7.

Figure 15: Dimensionless maximum width of the drop as a function of the Capillary number Ca for k = 0.7.

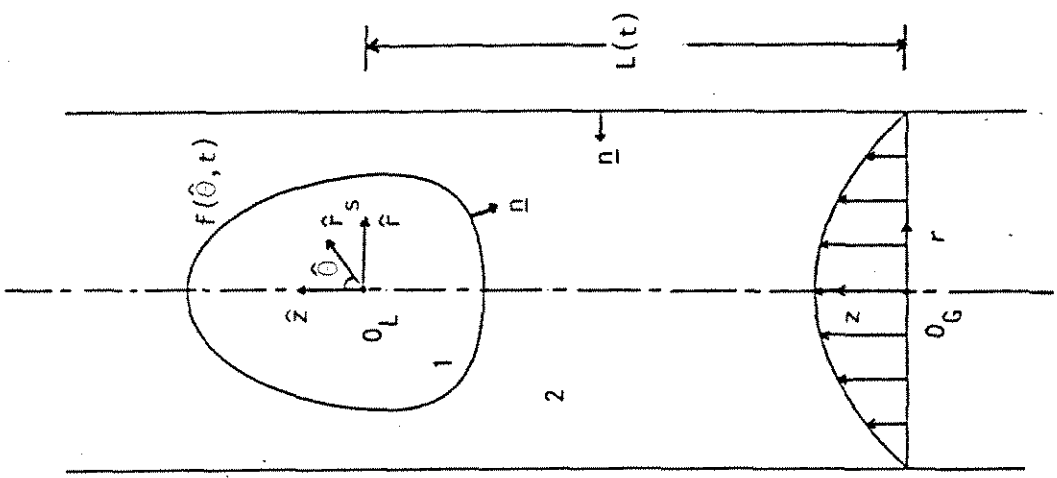

Figure 1a

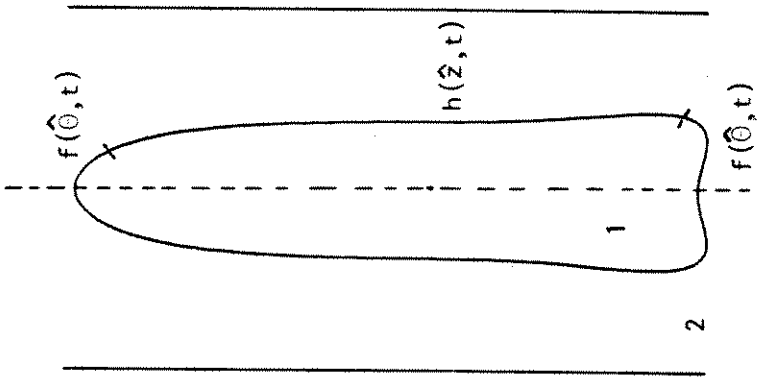

Figure 1b

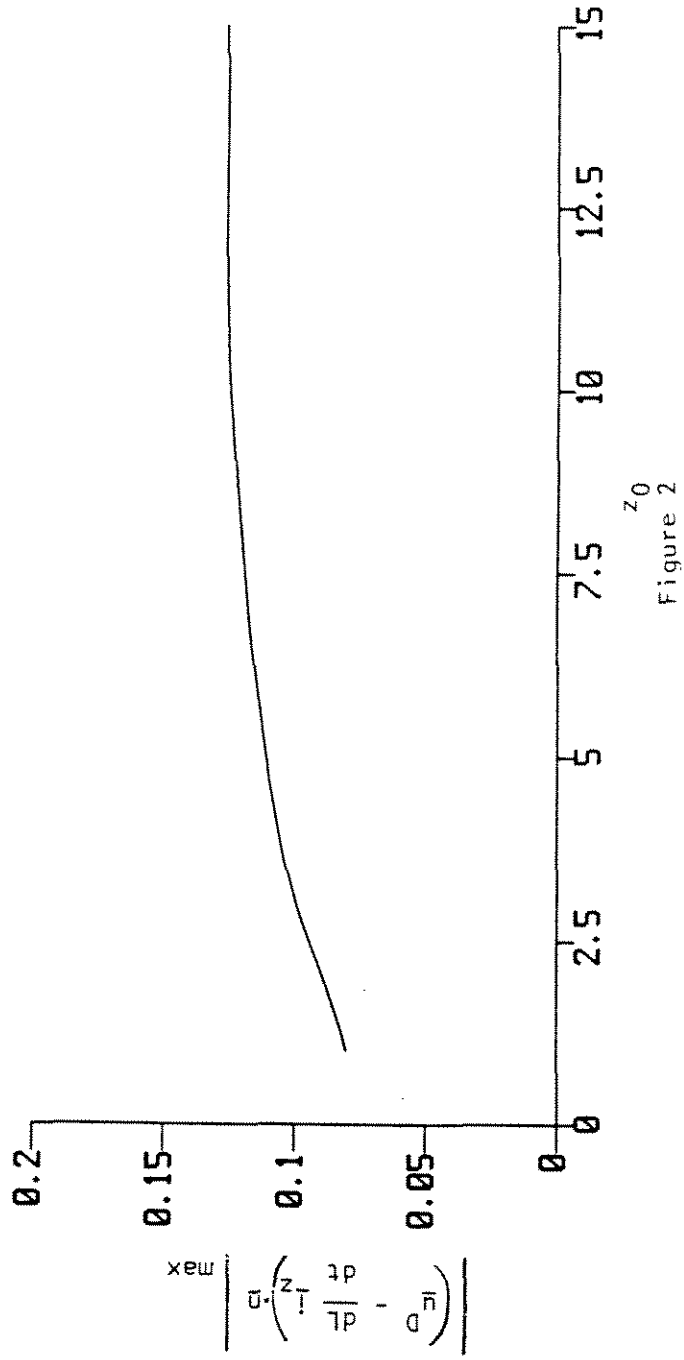
$\left| \left(\mu^D - \frac{dL}{dt} \, i_z \right) \cdot n \right|_{max}$
0.2
0.15
0.1
0.05
0
0
2.5
5
7.5
10
12.5
15
z_0

Figure 2


$\left| \left(i_{cD} - \frac{dL}{dt} i_Z \right) \cdot i_D \right|_{max}$
0.2
0.15
0.1
0.05
0
0
5
10
15
20
25
30
N_D

Figure 3

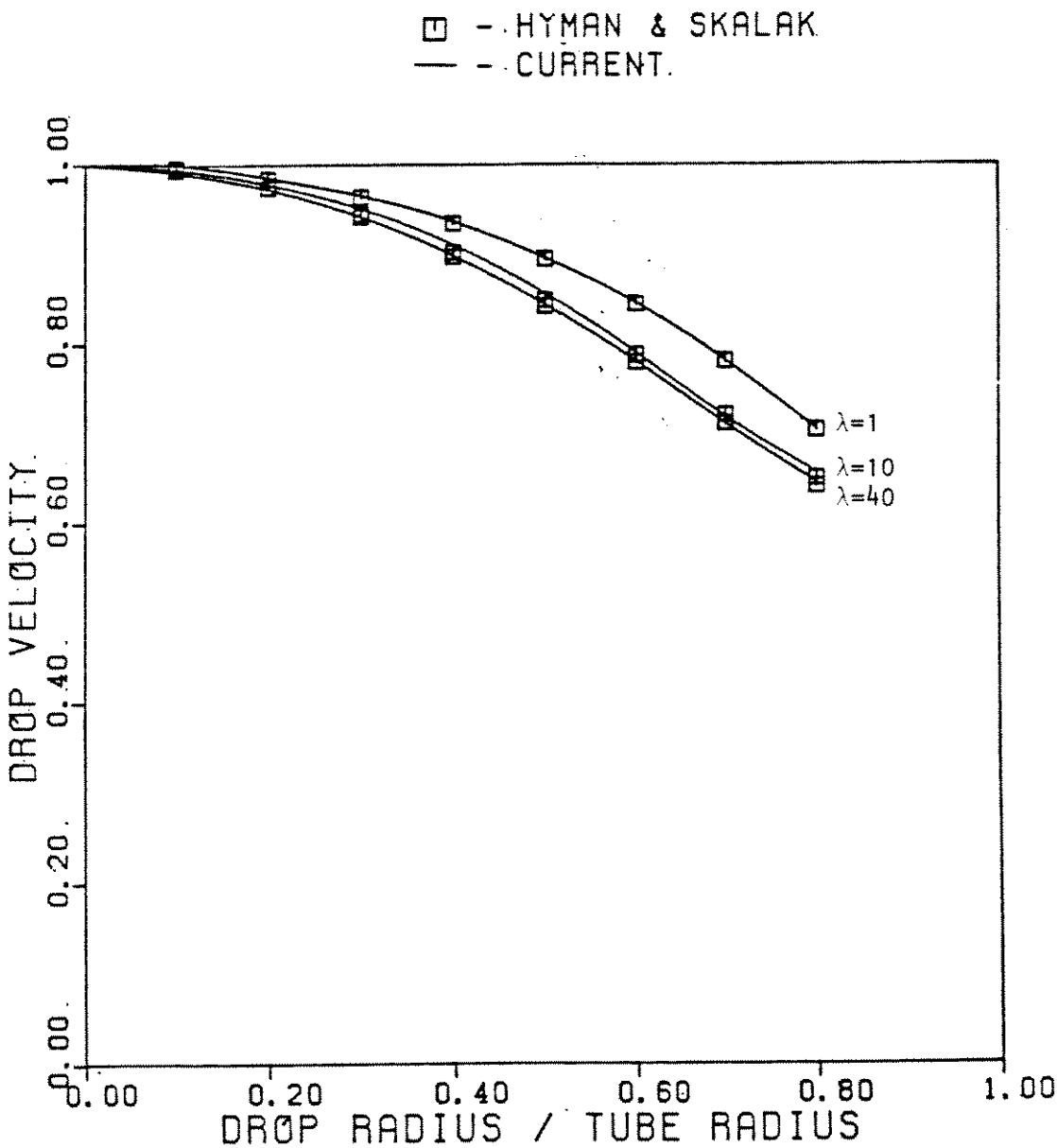
SPHERICAL DROP IN POISEUILLE FLOW
□ - HYMAN & SKALAK
— - CURRENT
DROP VELOCITY
1.00
0.80
0.60
0.40
0.20
0.00
λ=1
λ=10
λ=40
0.00
0.20
0.40
0.60
0.80
1.00
DROP RADIUS / TUBE RADIUS

Figure 5

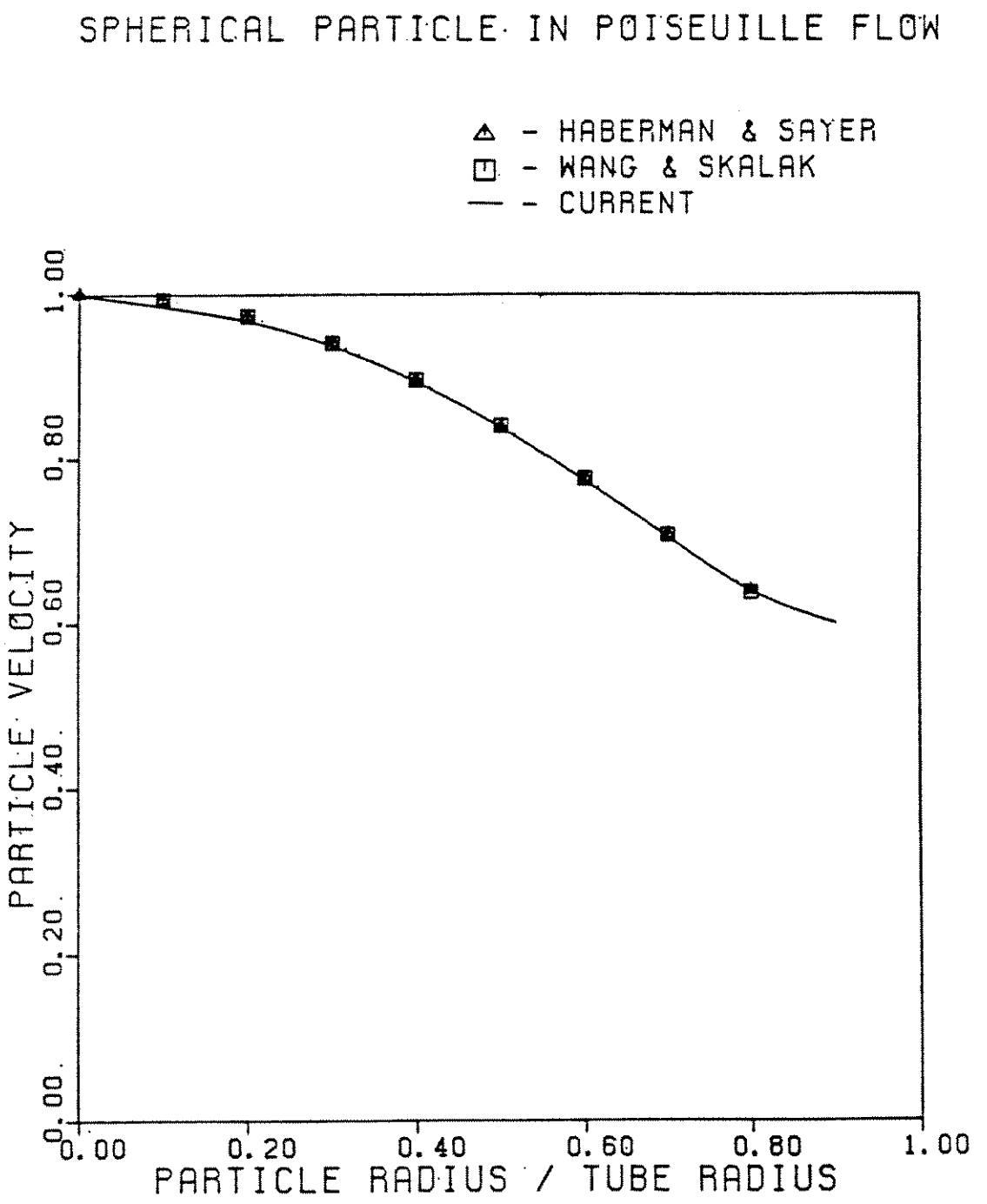
SPHERICAL PARTICLE IN POISEUILLE FLOW
△ - HABERMAN & SAYER
□ - WANG & SKALAK
— - CURRENT
PARTICLE VELOCITY
0.00
0.20
0.40
0.60
0.80
1.00
0.00
0.20
0.40
0.60
0.80
1.00
PARTICLE RADIUS / TUBE RADIUS

Figure 4

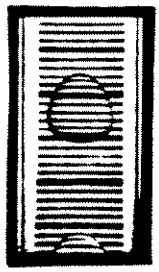

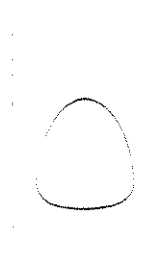

Ho and Leal (1975)
k = 0.726
Ca = 0.356
λ = 0.93

Calculated Result
k = 0.726
Ca = 0.356
λ = 0.93

(a)

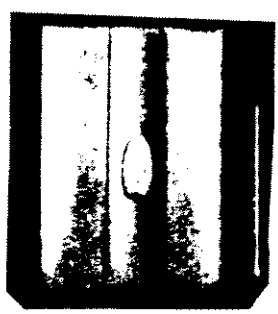

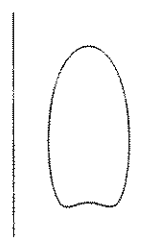

Kung (1985)
k = 0.7
Ca = 2.6
λ = 0.047

Calculated Result
k = 0.7
Ca = 3
λ = 0.1

(b)

Figure 6

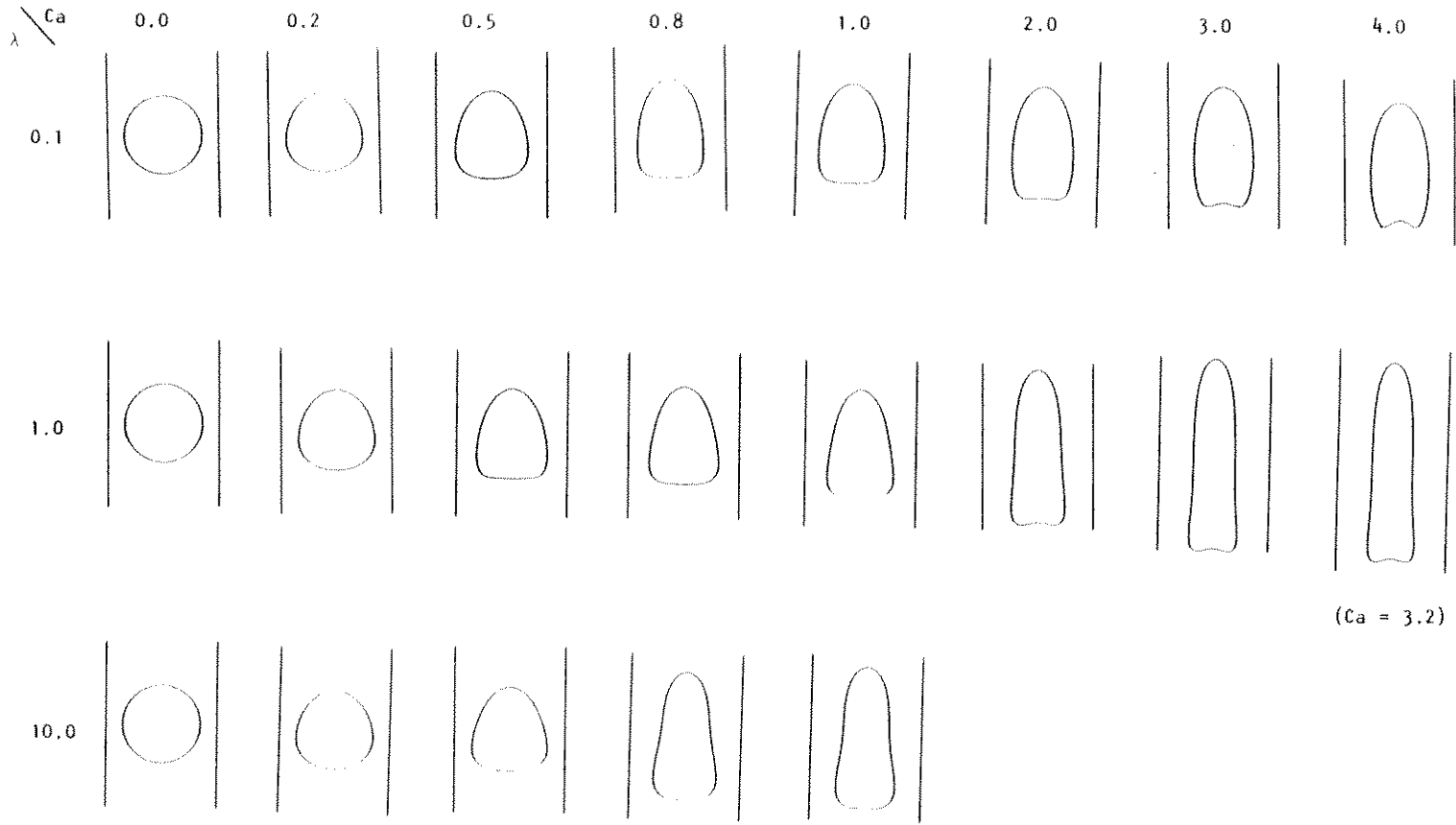

k = 0.7

Figure 7

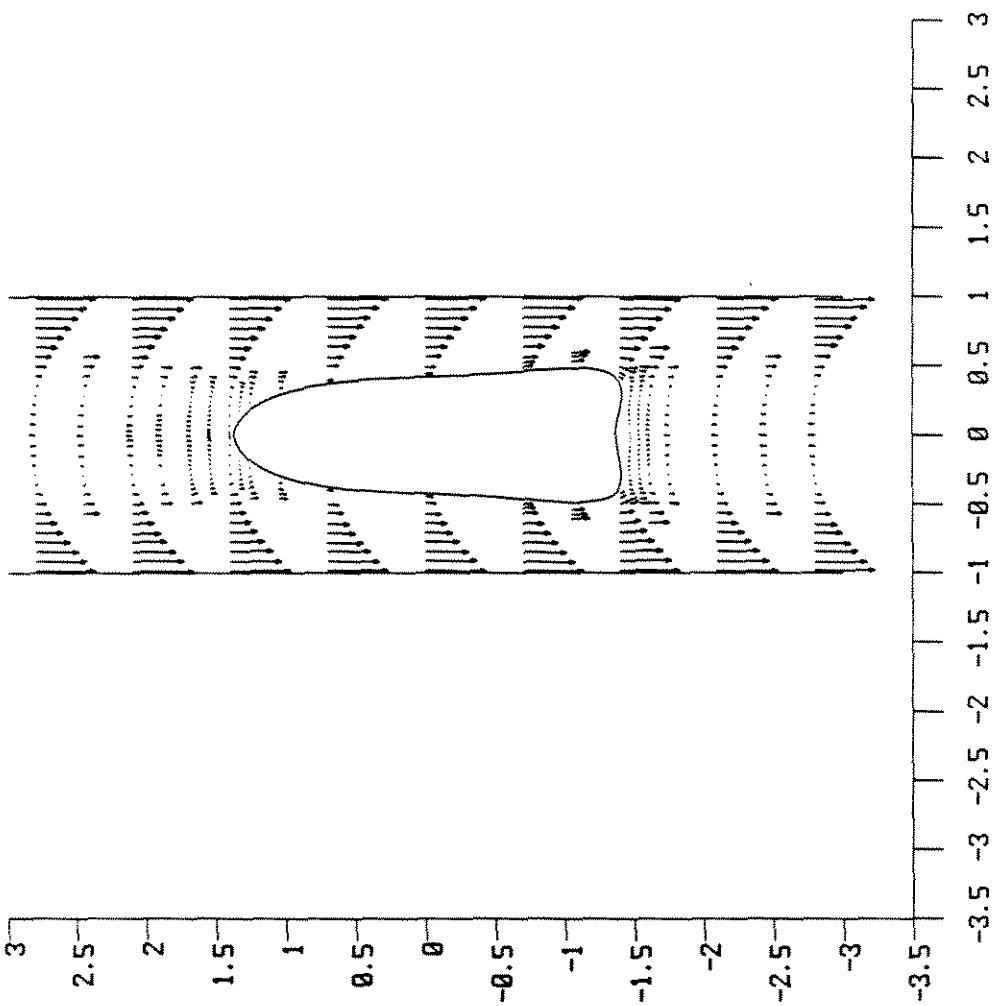

Figure 8

$k = 0.7 \quad \lambda = 0.047$

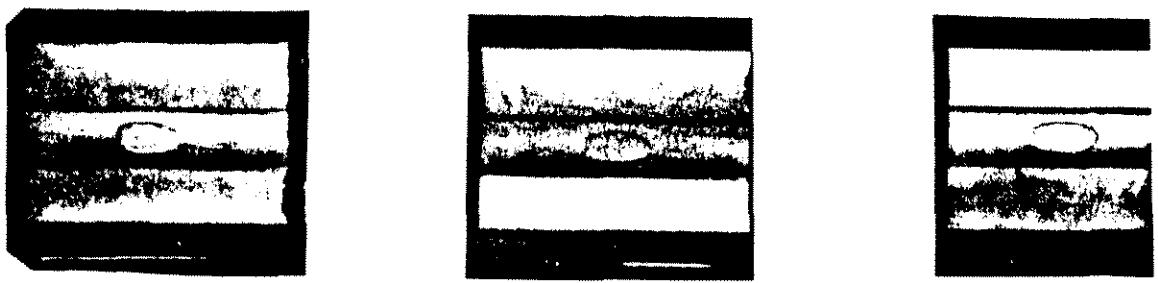

Ca = 2.6 Ca = 4.4 Ca = 5.4

Kung (1985)

Figure 9

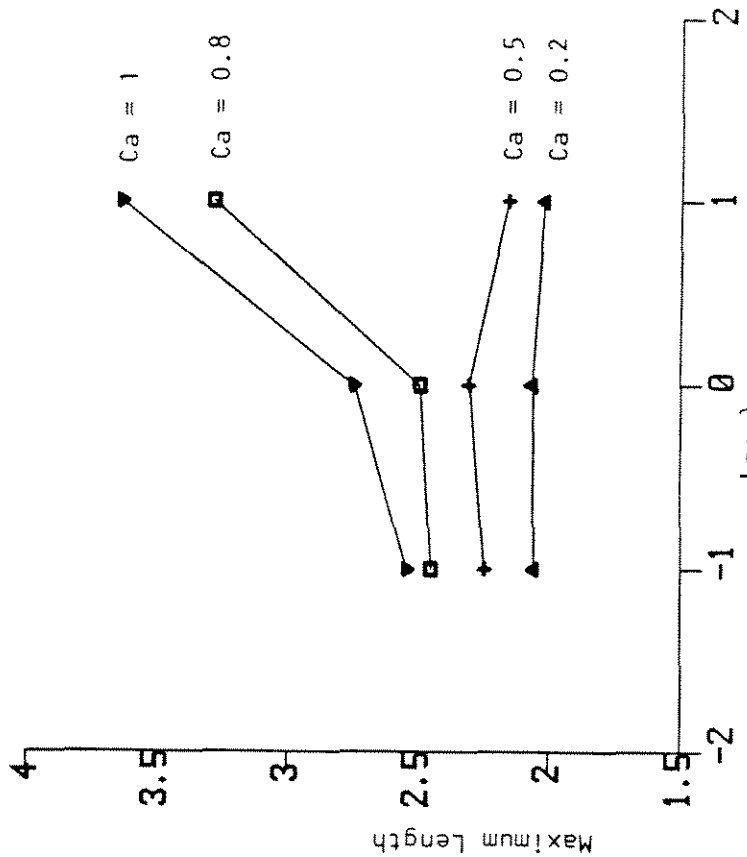

Figure 10

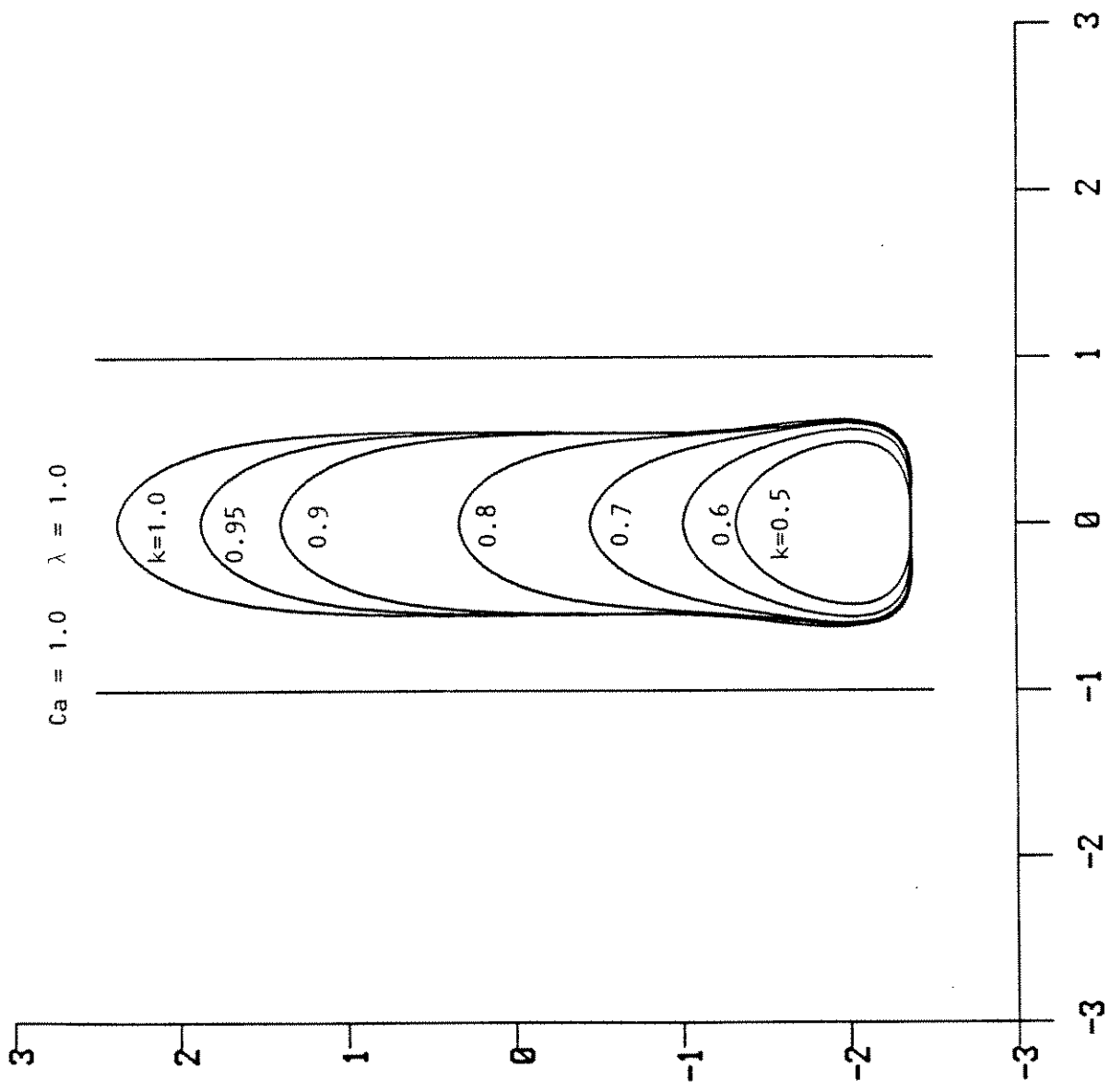

Figure 11

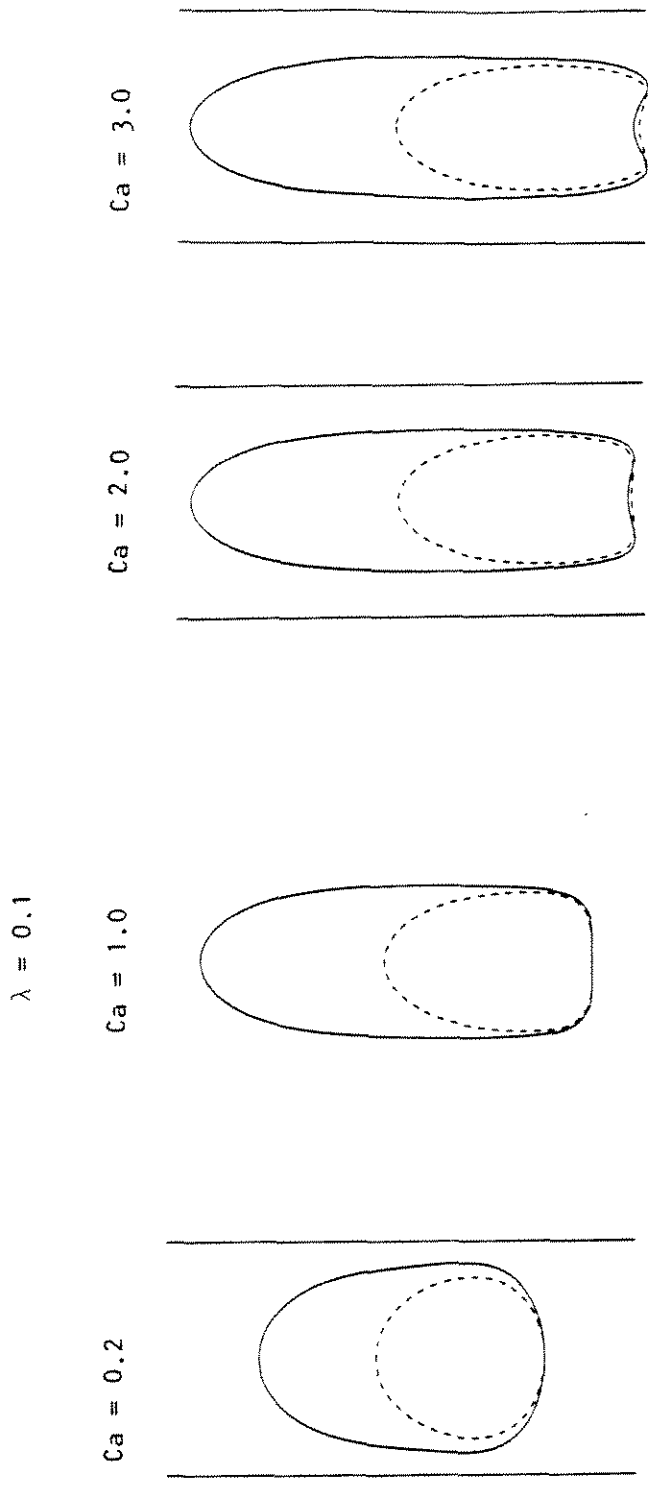

Figure 12

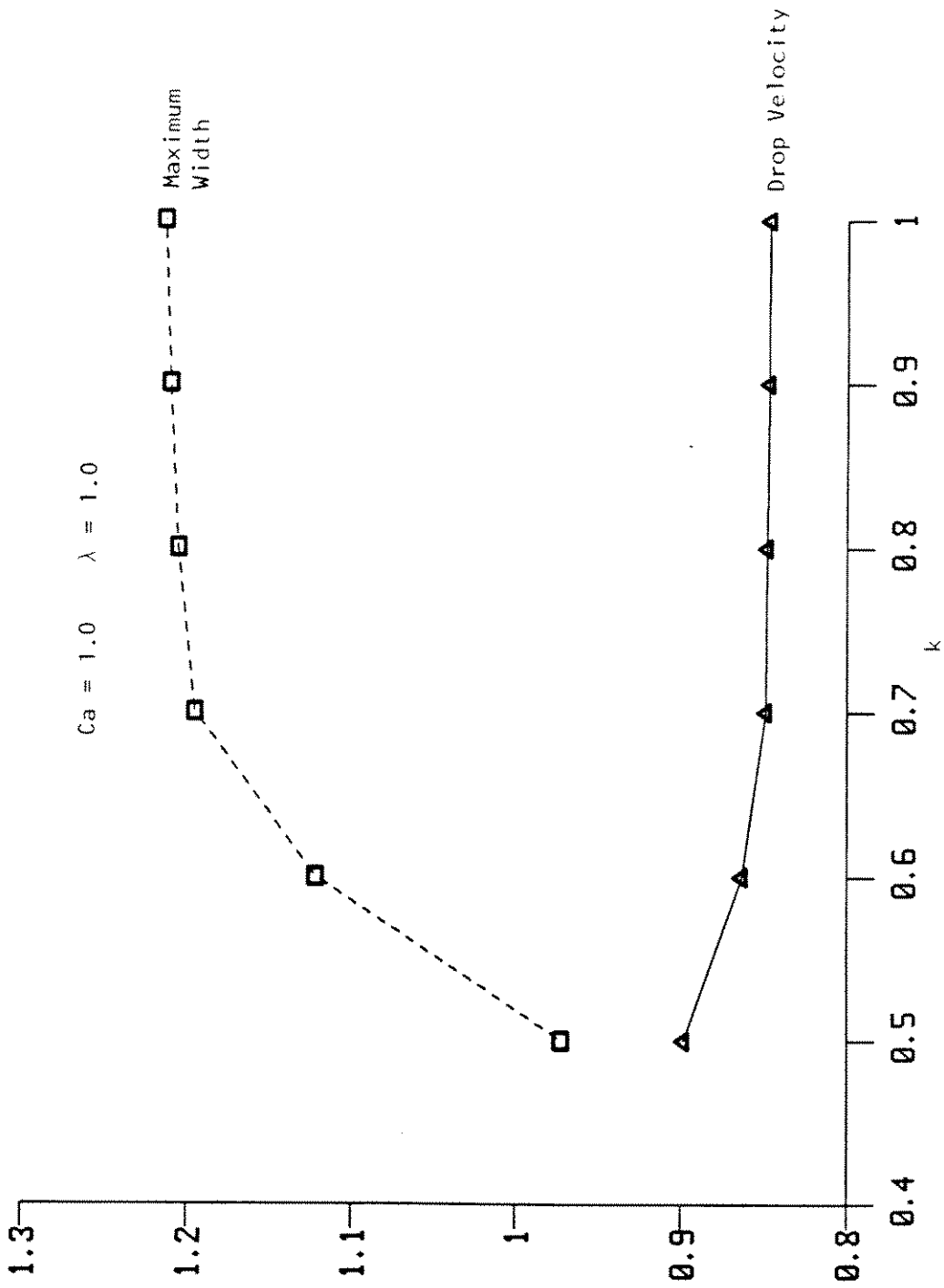
Ca = 1.0 λ = 1.0
Maximum Width
Drop Velocity
1.3
1.2
1.1
1
0.9
0.8
0.4
0.5
0.6
0.7
0.8
0.9
1
k

Figure 13

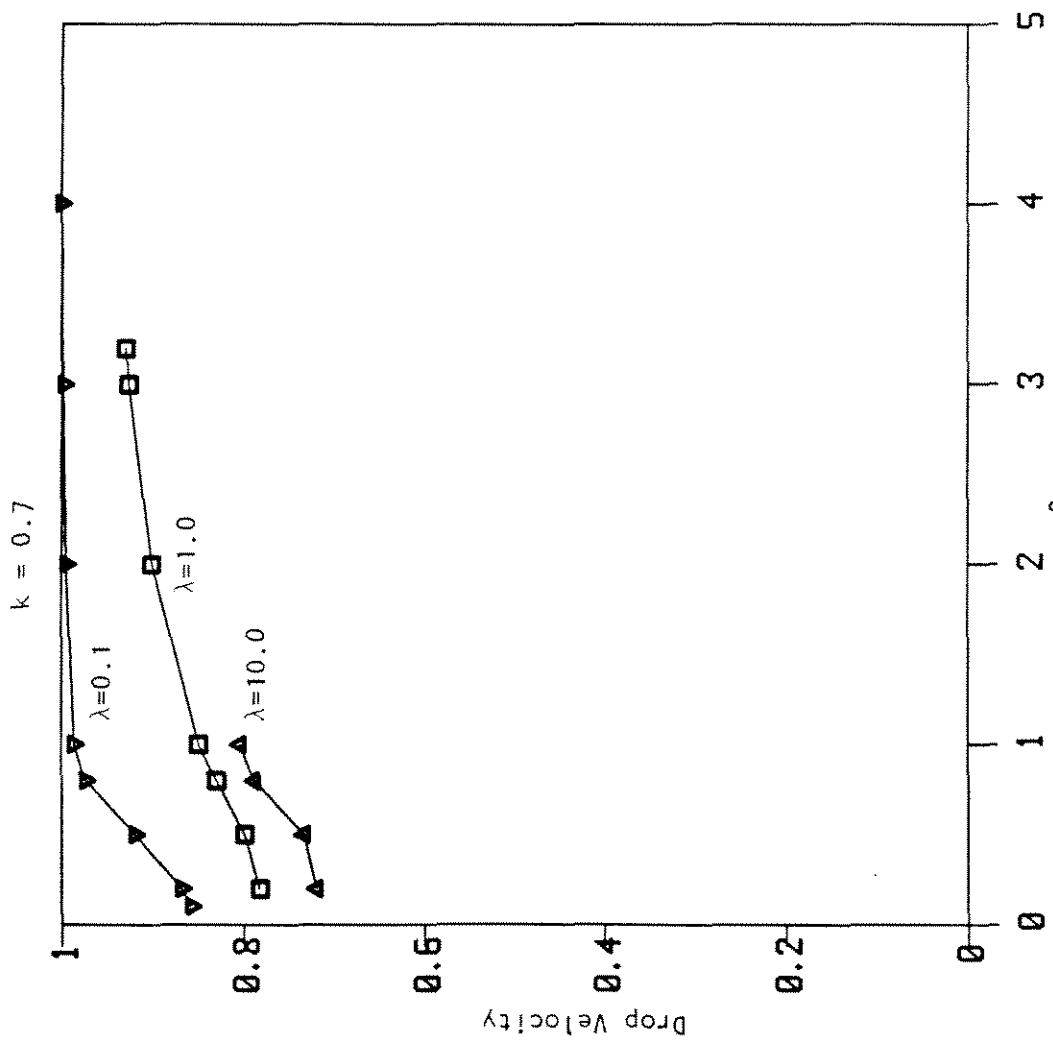

Figure 14

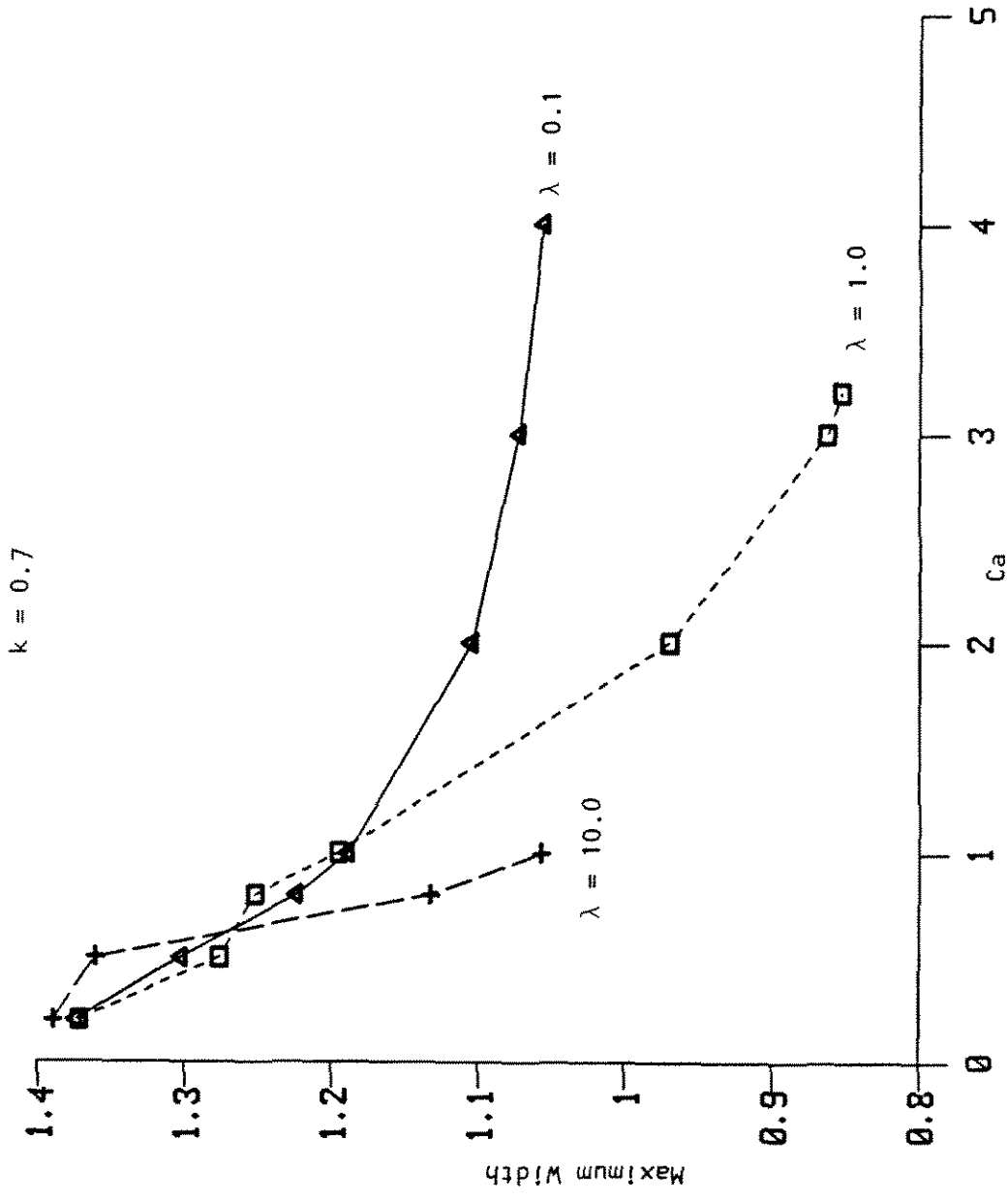

Figure 15

Chapter II.

Stability of Annular Flow

STABILITY OF ANNULAR FLOW

I. Introduction

The stability of two fluid systems in the presence of a primary flow constitutes an important class of problems. In particular, the stability of a long liquid droplet has received much attention because of its relevance to many industrial areas of chemical and polymer processing. For example, in the spinning of bicomponent fibers, two polymers are extruded together through a tube and then breakup of the inner fluid must be prevented. On the other hand, if formation of emulsions is the main concern, breakup of droplets must be encouraged to obtain a well dispersed two-phase systems. Tertiary oil recovery processes are more efficient if crude oil droplets coalesce to form an oil bank (Wasan et al., 1979). In this context, breakup of "oil ganglia" should be prevented.

In the present work, we consider the stability of annular flow of two Newtonian fluids through a circular cylindrical tube under the action of an applied pressure gradient. Specifically, we consider interface-driven instabilities that are unique to the two-fluid configuration. There are two mechanisms by which instability can develop at the interface. First, as shown originally by Yih (1967), the viscosity difference between two fluids can lead to instability when a primary flow is imposed. Second, the existence of finite surface tension can lead to instability via the growth of capillary waves.

The capillary instability of an infinitely long liquid cylinder was first recognized by Plateau (1873), and analyzed by Rayleigh (1892) who developed a linearized stability theory for a stationary viscous cylindrical liquid thread under the action of surface tension forces, but without a second suspending fluid. Tomotika (1935) extended Rayleigh's work to include the effect of a second viscous

fluid. His results show that the inner liquid thread is stable to disturbances with wavenumber ka > 1 and unstable when ka < 1. Between ka = 0 and ka = 1, there is a fastest growing linear mode near which breakup of the inner liquid into small droplets would most likely occur. The case of a stationary viscous liquid cylinder in a second stationary viscous liquid in a cylindrical tube was considered by Mikami and Mason (1975). Their results are similar to Tomotika's except that the effect of the tube is to make the interface less unstable. In all of the above works, instability arises solely from capillary forces, and the viscosity difference does not play a role in generating the instability. It only modifies the effect of capillary instability by decreasing the growth rate of unstable modes as the inner fluid becomes more viscous.

Yih (1967) seems to have been the first to recognize that an interface can be unstable at any Reynolds number, in laminar flow, due to the viscosity difference between two fluids. Yih carried out a linear analysis of the stability of long wave disturbances for two superposed fluids of different viscosities in plane Couette and Poiseuille flow including the effect of inertia. Hickox (1971) utilized Yih's long wavelength technique to consider annular flow. However, he considered only the case when the less viscous fluid is at the core, which is unstable at all Re. Joseph et al. (1983,1984) carried out a numerical study of the stability of annular flow at all wavelengths, but neglecting surface tension. They found that the flow is unstable to long waves if the less viscous fluid is at the core, in agreement with Hickox's result. When the more viscous fluid is at the core, the stability depends on the volume ratio of the two fluids. If a large volume of more viscous fluid is at the core, the flow is stable to long waves. On the other hand, the flow is unstable to long waves if a small volume of the more viscous fluid is at the core. In Joseph's work, however, modes of maximum instability were not determined because the numerical analysis was carried out for a few selected values

of ka, the dimensionless wavenumber.

In a related study, Hooper and Boyd (1983) considered the linear stability of the shear flow of two fluids of different viscosities in an infinite region. They found that the interface is unstable to short wavelength disturbances. In a continuation of this work, however, to consider the stability of the interface between two viscous fluids when the lower fluid is bounded by a solid boundary and the upper fluid is of infinite extent, Hooper (1985) found that the flow is unstable to long-wavelength disturbances when the lower fluid is more viscous than the upper fluid. Renardy (1985) extended the work of Hooper (1985) by numerically evaluating the growth factor of linear stability for plain Couette flow composed of two immiscible fluids in layers of arbitrary depths.

Our current study considers the linear stability of axisymmetric disturbances in annular flow through a circular tube when the mechanisms of instability due to a viscosity difference and to surface tension are simultaneously present, but with the restriction to small values of the Reynolds number [i.e. $Re \leq O(1)$]. The results of Joseph et al. (1983) indicate that for small Re (< 1) axisymmetric disturbances and non-axisymmetric disturbances show similar qualitative behavior, and this suggests that our analysis of axisymmetric disturbances in the small Re range will exhibit the general stability characteristics of the flow. The range of Re is limited in the present work due to the convergence requirements of the series type solution which we pursue. The objective of the current work is to study the effects of viscosity ratio, surface tension, radius ratio, and Reynolds number on the stability of the interface as well as on the modes of maximum instability. There is no intrinsic restriction placed on the disturbance wavenumber (i.e. wavelength).

II. Formulation and Solution

We consider two fields of equal density, but differing viscosities μ and $\hat{\mu}$, flowing through a tube of radius R_1 with the inner fluid occupying a cylindrical region of radius R_2 (Fig. 1). The primary flow is then given in dimensionless form as

$$W(r) = \frac{1}{1 - a^2}(1 - r^2) \tag{1}$$

$$\hat{W}(r) = \frac{1}{1 - a^2}\left(1 - \frac{1}{m}r^2\right) - \frac{a^2}{1 - a^2}\left(1 - \frac{1}{m}\right) \tag{2}$$

where $a = R_2/R_1$ and $m = \hat{\mu}/\mu$. Now, we assume that the steady Poiseuille flow given by (1) and (2) is subject to an infinitesimal disturbance at $t = 0$. Then the altered flow can be expressed as a sum of the primary and disturbance flows. For example, in fluid 1,

$$u = u'$$

$$w = W(r) + w'$$

$$p = P(z) + p'$$

where u and w are the radial and axial velocity components, respectively. Restricting attention to axisymmetric disturbances, the disturbance velocities are expressed in terms of a stream function in the form $\varphi(r)e^{i(nt+kz)}$ where φ is the amplitude function, k is the wavenumber (real), and n is the complex eigenvalue $n = n_r + in_i$. The flow is unstable if $n_i < 0$ and stable if $n_i > 0$. Substituting the above form of the disturbance stream function into the linearized Navier-Stokes equations, we obtain the Orr-Sommerfeld equation in cylindrical coordinates with the primary Poiseuille flow in fluid 1 given by Eq. (1).

$$L_1 L_2 \varphi = 0 \tag{3}$$

where

$$L_1 = \frac{d^2}{dr^2} - \frac{1}{r}\frac{d}{dr} - k^2 \tag{4}$$

$$L_2 = L_1 - in - Re\,\frac{1 - r^2}{1 - a^2}\,ik \tag{5}$$

and Re denotes the Reynolds number, $l_c u_c/\nu$. In deriving these equations, we utilize the following characteristic variables for nondimensionalization:

$$l_c = R_1 \tag{6}$$

$$u_c = \frac{G}{4\mu}(R_1^2 - R_2^2) \tag{7}$$

$$p_c = \frac{\mu u_c}{l_c} \tag{8}$$

$$t_c = \frac{l_c^2}{\nu} \tag{9}$$

where G is the applied pressure gradient, and ν is the kinematic viscosity μ/ρ. Similar equations apply also to fluid 2 with $\hat{\varphi}$ denoting the amplitude function for fluid 2. Same characteristic variables are utilized in fluid 2 as in fluid 1 for nondimensionalization. The operators in Eq. (3) are commutative with each other. Therefore, φ can be separated into two parts

$$\varphi = \varphi_1 + \varphi_2 \tag{10}$$

with φ_1 and φ_2 satisfying

$$L_1 \varphi_1 = 0 \tag{11}$$

and

$$L_2\varphi_2 = 0, \tag{12}$$

respectively. The linearized stability analysis thus reduces to the solution of (11) and (12) for φ_1 and φ_2.

A general solution for Eq. (11) can be expressed in the form

$$\varphi_1 = A_1 r I_1(kr) + B_1 r K_1(kr)$$

where A_1 and B_1 are constants, and I_1 and K_1 are modified Bessel functions of first order. Equation (12) does not yield a solution of simple form in terms of well-known functions. However, a general solution can be obtained in terms of a Frobenius series. If we rewrite Eq. (12) so that the independent variable is kr, then Eq. (12) becomes

$$x \frac{d^2\varphi_2}{dx^2} - \frac{d\varphi_2}{dx} - \frac{\alpha}{k^2} x\varphi_2 + \frac{\beta}{k_4} x^3\varphi_2 = 0 \tag{13}$$

where

$$x = kr$$

$$\alpha = k^2 + in + \frac{Re}{1 - a^2} ik \tag{14}$$

$$\beta = \frac{Re}{1 - a^2} ik .$$

Assuming a solution in terms of a Frobenius series

$$\varphi_2 = x^s \sum_{n=0}^{\infty} A_n x^n , \tag{15}$$

we obtain the general solution of Eq. (13) in the form

$$\varphi_2 = A_2 y_a(x) + B_2 y_b(x) \tag{16}$$

where A_2 and B_2 are constants, and y_a and y_b are infinite series of the form

$$y_a = \sum_{n=0}^{\infty} b_n x^n \tag{17}$$

in which

$$b_0 = 0$$

$$b_1 = b_3 = b_5 = \cdots = 0$$

$$b_2 = 1$$

$$b_n = -\frac{1}{n(n-2)} \frac{\beta}{k^4} b_{n-4} + \frac{1}{n(n-2)} \frac{\alpha}{k^2} b_{n-2} \quad \text{for} \quad n \geq 4$$

and

$$y_b = \log x \cdot y_a(x) + \sum_{n=0}^{\infty} a_n x^n \tag{18}$$

in which

$$a_1 = a_3 = a_5 = \cdots = 0$$

$$a_0 = 2 \frac{k^2}{\alpha} b_2$$

$$a_2 = 1$$

$$a_n = -\frac{\beta}{k^4} \frac{1}{n(n-2)} a_{n-4} + \frac{\alpha}{k^2} \frac{1}{n(n-2)} a_{n-2} - \frac{2(n-1)}{n(n-2)} b_n \quad \text{for} \quad n \geq 4$$

and

$$\alpha = k^2 + in + Re\left(\frac{1}{1-a^2}\right) ik$$

$$\beta = Re\left(\frac{1}{1-a^2}\right) ik .$$

Then, a general solution of Eq. (3) is

$$\varphi = A_1 r I_1(kr) + B_1 r K_1(kr) + A_2 y_a(kr) + B_2 y_b(kr) . \tag{19}$$

A similar analysis for fluid 2 yields a solution of the same form

$$\hat{\varphi} = \hat{A}_1 r I_1(kr) + \hat{B}_1 r K_1(kr) + \hat{A}_2 \hat{y}_a(kr) + \hat{B}_2 \hat{y}_b(kr) . \tag{20}$$

where

$$\hat{y}_a = \sum_{n=0}^{\infty} \hat{b}_n x^n \tag{21}$$

$$\hat{b}_0 = 0$$

$$\hat{b}_1 = \hat{b}_3 = \hat{b}_5 = \cdots = 0$$

$$\hat{b}_2 = 1$$

$$\hat{b}_n = -\frac{1}{n(n-2)} \frac{\hat{\beta}}{k^4} \hat{b}_{n-4} + \frac{1}{n(n-2)} \frac{\hat{\alpha}}{k^2} \hat{b}_{n-2} \quad \text{for } n \geq 4$$

$$\hat{y}_b = \log x \cdot \hat{y}_a(x) + \sum_{n=0}^{\infty} \hat{a}_n x^n \tag{22}$$

$$\hat{a}_1 = \hat{a}_3 = \hat{a}_5 = \cdots = 0$$

$$\hat{a}_0 = 2 \frac{k^2}{\hat{\alpha}} \hat{b}_2$$

$$\hat{a}_2 = 1$$

$$\hat{a}_n = -\frac{\hat{\beta}}{k^4}\frac{1}{n(n-2)}\hat{a}_{n-4} + \frac{\hat{\alpha}}{k^2}\frac{1}{n(n-2)}\hat{a}_{n-2} - \frac{2(n-1)}{n(n-2)}\hat{b}_n \quad \text{for } n \geq 4$$

and

$$\hat{\alpha} = k^2 + \frac{in}{m} + \frac{Re}{m}\left[1 + \frac{a^2}{(1-a^2)m}\right]ik$$

$$\hat{\beta} = \frac{Re}{m}\left[\frac{1}{(1-a^2)m}\right]ik$$

At $r = 0$, the velocity components $\hat{u}$, $\hat{w}$ must be finite. Therefore,

$$\hat{\varphi} = \hat{A}_1 r I_1(kr) + \hat{A}_2 \hat{y}_a(kr) \,. \tag{23}$$

All that remains is to apply boundary conditions in order to determine the constants A_1, A_2, B_1 B_2, $\hat{A}_1$ and $\hat{A}_2$.

In deriving the boundary conditions, second and higher order terms in disturbance quantities are neglected. In the following discussion, primes on φ and $\hat{\varphi}$ denote differentiation with respect to r. The position of the interface is denoted as $r = a + \eta$ where η denotes a small deviation from the steady shape of the interface (Fig. 1). Since u' at the interface is

$$u'\Big|_{r=a+\eta} = \frac{\partial \eta}{\partial t} + W(a)\,\frac{\partial \eta}{\partial z} = \frac{1}{a}\,\varphi(a)e^{i(nt+kz)}\cdot ik, \tag{24}$$

solving Eq. (24), η is found to be

$$\eta = \frac{1}{a}\,\frac{\varphi(a)}{c}\,e^{i(nt+kz)} \tag{25}$$

where

$$c = \frac{n}{k} + W(a) .$$

The boundary conditions are then

1. No-slip at the tube wall, r = 1.

$$u' \Big|_{r=1} = 0 \quad \text{or} \quad \varphi(1) = 0 \tag{26}$$

and

$$w' \Big|_{r=1} = 0 \quad \text{or} \quad \varphi'(1) = 0 \tag{27}$$

2. Continuity of radial velocity at the interface, $r = a + \eta$.

$$u' \Big|_{r=a} = \hat{u}' \Big|_{r=a} \quad \text{or} \quad \varphi(a) = \hat{\varphi}(a) . \tag{28}$$

3. Continuity of axial velocity at the interface.

$$\left(w' + \eta \frac{\partial W}{\partial r} \right)_{r=a} = \left(\hat{w}' + \eta \frac{\partial \hat{W}}{\partial r} \right)_{r=a} \quad \text{or}$$

$$-\varphi'(a) + \frac{\varphi(a)}{c} \frac{\partial W}{\partial r} \Big|_{r=a} = -\hat{\varphi}'(a) + \frac{\hat{\varphi}(a)}{c} \frac{\partial \hat{W}}{\partial r} \Big|_{r=a} . \tag{29}$$

4. Continuity of tangential stress at the interface.

$$\left(\frac{\partial u'}{\partial z} + \frac{\partial w'}{\partial r} + \eta \frac{\partial^2 W}{\partial r^2} \right)_{r=a} = m \left(\frac{\partial \hat{u}'}{\partial z} + \frac{\partial \hat{w}'}{\partial r} + \eta \frac{\partial^2 \hat{W}}{\partial r^2} \right)_{r=a}$$

or

$$-\frac{1}{a} \varphi''(a) + \frac{1}{a^2} \varphi'(a) + \left(-\frac{k^2}{a} + \frac{1}{ac} \frac{\partial^2 W}{\partial r^2} \right) \varphi(a)$$

$$= m \left\{ -\frac{1}{a} \hat{\varphi}''(a) + \frac{1}{a^2} \hat{\varphi}'(a) + \left(-\frac{k^2}{a} + \frac{1}{ac} \frac{\partial^2 \hat{W}}{\partial r^2} \right) \hat{\varphi}(a) \right\} . \tag{30}$$

5. Balance of the normal stress difference across the interface and the capil-

lary force due to surface curvature.

$$\left[-p' + 2\frac{\partial u'}{\partial r} - 2\frac{\partial W}{\partial r}\frac{\partial \eta}{\partial z}\right]_{r=a} - \left[-\hat{p}' + 2m\frac{\partial \hat{u}'}{\partial r} - 2m\frac{\partial \hat{W}}{\partial r}\frac{\partial \eta}{\partial z}\right]_{r=a}$$

$$= \frac{1}{Ca}\left[-\frac{\eta}{a^2} - \frac{\partial^2 \eta}{\partial z^2}\right] \tag{31}$$

In Eq. (31), Ca denotes the capillary number, $\mu u_c/\sigma$, where σ is the interfacial tension.

In order to apply (31), it is necessary to express p' and $\hat{p}'$ in terms of φ and $\hat{\varphi}$. Since it is assumed that the motions are proportional to $e^{i(nt+kz)}$. Thus, letting

$$p' = f(r)e^{i(nt+kz)} \tag{32}$$

$$\hat{p}' = \hat{f}(r)e^{i(nt+kz)}, \tag{33}$$

the z-component of the governing equations for fluids 1 and 2 give

$$f = -\frac{1}{ikr}\varphi''' + \frac{1}{ikr^2}\varphi'' + \left[-\frac{1}{ikr^3}\frac{k}{ir} + \frac{n}{kr} + \frac{ReW}{r}\right]\varphi' - \frac{Re}{r}\frac{\partial W}{\partial r}\varphi \tag{34}$$

$$\hat{f} = -\frac{1}{ikr}\hat{\varphi}''' + \frac{m}{ikr^2}\hat{\varphi}'' + \left[-\frac{m}{ikr^3} + \frac{mk}{ir} + \frac{n}{kr} + \frac{Re\hat{W}}{r}\right]\hat{\varphi}' - \frac{Re}{r}\frac{\partial \hat{W}}{\partial r}\hat{\varphi} \tag{35}$$

Then, in terms of φ and $\hat{\varphi}$, the interface boundary condition (31) becomes

$$-\frac{i}{ka}\varphi''' + \frac{i}{ka^2}\varphi'' + \left[-\frac{i}{ka^3} + \frac{3ik}{a} - \frac{n}{ka} - \frac{ReW}{a}\right]\varphi'$$

$$+\left[-\frac{2ik}{a^2} - \frac{2ik}{ac}\frac{\partial W}{\partial r} + \frac{Re}{a}\frac{\partial W}{\partial r}\right]\varphi$$

$$-\left\{-\frac{mi}{ka}\hat{\varphi}''' + \frac{mi}{ka^2}\hat{\varphi}'' + \left[-\frac{mi}{ka^3} + \frac{3mik}{a} - \frac{n}{ka} - \frac{Re\hat{W}}{a}\right]\hat{\varphi}'\right.$$

$$+\left(-\frac{2mik}{a^2}-\frac{2mik}{ac}\frac{\partial\hat{W}}{\partial r}+\frac{Re}{a}\frac{\partial\hat{W}}{\partial r}\right)\hat{\varphi}\Bigg\}=\frac{1}{Ca}\left(-\frac{1}{a^3c}+\frac{k^2}{ac}\right)\varphi \qquad (36)$$

Substituting the general solutions φ and $\hat{\varphi}$ into the boundary conditions of Eqs. (26)-(30) and (36), we obtain six simultaneous algebraic equations for the six unknown coefficients, A_1, A_2, B_1, B_2, $\hat{A}_1$ and $\hat{A}_2$,

$$\mathbf{Fx} = 0$$

with $\mathbf{x}$ denoting the vector of unknown coefficients $[A_1, A_2, B_1, B_2, \hat{A}_1, \hat{A}_2]^T$. The elements of the matrix $\mathbf{F}$ are given in the Appendix. Since Eq. (37) is a system of linear homogeneous equations, it has a nontrivial solution vector if and only if $\det\mathbf{F} = 0$. The problem here then is to find the eigenvalue n that satisfies the characteristic equation $\det\mathbf{F} = 0$ given a, k, m, Ca and Re. So far, we have placed no restrictions on any of these parameters.

III. Results

Numerical calculations using Newton's method were carried out to evaluate the complex eigenvalue n which satisfies $\det\mathbf{F} = 0$. The series y_a, y_b and y_c were truncated at the 40th term. The initial guess for n in each case was the value of n from the calculations of Mikami and Mason (1975) who considered the corresponding stability problem when both liquids are stationary.

In view of the fact that the stability analysis is linear in the magnitude of the disturbance amplitude functions, φ and $\hat{\varphi}$, it might seem at first that the growth factor $-n_i$ (and the criteria for instability) could be obtained as a superposition of the separate results for capillary instability in the absence of flow (Mikami and Mason, 1975) and for instability due to a viscosity difference with pressure driven-flow in the absence of capillary forces ($\gamma = 0$ or $Ca \to \infty$). However, this is not possible because the growth factor is nonlinear in m and Ca. The governing

equations and boundary conditions are linearized with respect to disturbance amplitude function φ and $\hat{\varphi}$, but not linearized with respect to m and Ca. One indication of the problem can be seen by considering results for m = 1, where only the capillary instability is present at the interface, and for Ca = ∞, when instability is due solely to the viscosity difference between the two fluids. An attempt to obtain the growth factors due to the simultaneous presence of the viscosity difference and surface tension by a linear combination of the growth factors for capillary instability and for instability due to the viscosity difference clearly does not work in this case Mikami and Mason (1975) have shown that the growth factors for capillary instability alone is a nonlinear function of the viscosity ratio. In particular, one cannot obtain the growth factors for m $\neq$ 1 from the growth factors for m = 1 by multiplying by a factor that is independent of ka. The results of Mikami and Mason (1975) show that the multiplication factor depends on m as well as ka. The fundamental "nonlinearity" of the dependence of n_i on m and Ca can also be demonstrated by considering our own numerical results. For example, in Fig. 8, we consider the general problem with a = 0.7, m = 2.0 and Ca = 1.0. The solid lines represent the growth factors for a = 0.7, m = 2.0, Ca = 1.0 when both surface tension and a viscosity difference exist simultaneously, and the broken lines represent the growth factors obtained by adding the growth factors for a = 0.7, m = 2.0, Ca = ∞ in the presence of Poiseuille flow and those for a = 0.7, m = 2.0, Ca = 1.0 with no primary flow. In other words, the broken lines are obtained by adding the the growth factors due to the viscosity difference alone (Ca = ∞) and due to capillary instability alone (no primary flow). As can be seen in Fig. 8, when Re = 0.0 the broken line coincides with the solid line. However, for Re = 0.4 simple addition of the two separate instabilities does not yield the overall instability represented by the solid line. In general, for the cases of finite Re in Fig. 8, the growth factors due

to the simultaneous presence of the viscosity difference and surface tension cannot be obtained by adding the separate growth factors due to the viscosity difference and surface tension.

Our current study exhibits the simultaneous effects of surface tension and the viscosity difference between two fluids for finite but small Re. Since there is no restriction on ka, neutral stability points and modes of maximum instability are also studied in the present work. The ranges of parameters considered are as follows: viscosity ratio from 0.5 to 2.0, capillary number from 0.1 to ∞, Reynolds number from 0 to 0.4, and radius ratio from 0.1 to 0.9. There is no intrinsic restriction on the range of ka; however, the range of ka considered in this study is between 0 and 2 because instabilities occur in this range of ka. Current calculations are done for small Re because the series in Eqs. (17), (18) and (21) diverges for Re > O(1).

A. Effect of m and Ca

In Figs. 2, 3 and 4, the negative growth factor, n_i, is plotted against ka for m = 0.5, 1.0 and 2.0 with Ca = ∞, 1.0 and 0.1, respectively, for the case when a = 0.7 and Re = 0.1. When Ca = ∞, the surface tension is zero and it is evident, as shown in Fig. 2, that the existence of stable or unstable modes is determined solely by the viscosity difference between the two phases. In particular, when there is no viscosity difference between the two fluids, i.e. m = 1 the interface is neutrally stable for all ka. This result not only agrees with the result of Yih (1967), but is obvious physically since no mechanism for instability then exists at the interface. The flow is unstable for the long wavelength disturbances considered in the current study when m = 0.5. However, as can be seen in Fig. 2, the magnitude of the growth factor decreases as ka increases beyond 1.30 and it can therefore be surmised that the interface would be stable for sufficiently

short wavelength disturbances. The interface is stable for all ka considered when m = 2.0, and the interface becomes more stable as ka increases. Then, by extrapolating the above trend, the interface is expected to be stable for short wavelength disturbances as well. Therefore, in the absence of surface tension, the configuration with the less viscous liquid on the inside is unstable to long wavelength disturbances, while that with the more viscous liquid on the inside is stable to all wavelengths. This behavior is consistent with the results obtained by Joseph et al. (1983) for higher values of Re, and is therefore presumably true over the whole range.

The effect of surface tension can be seen in Fig. 3 for Ca = 1.0. The flow is now unstable to long wavelength disturbances for all three viscosity ratios considered, including m = 2.0 which is stable when Ca = ∞, but is stable to short wavelength disturbances. It can also be seen in Fig. 3 that the neutral stability point occurs for ka greater than 1 if m < 1, equal to 1 if m = 1, and less than 1 if m > 1. Specifically, the flow becomes unstable at ka = 0.85, 1.0, 1.1 for m = 2.0, 1.0, 0.5, respectively. In other words, the unstable range of wavenumbers is decreased as the viscosity of the inner fluid is increased relative to the other fluid, and the growth factor is decreased. Similar effects of surface tension are shown in Fig. 4 for Ca = 0.1 except that the flow is more unstable compared to the case of Ca = 1.0. It is interesting to compare ka for neutral stability for the two cases Ca = 1.0 and Ca = 0.1. When Ca = 0.1 and m = 0.5, neutral stability occurs at ka = 1.02 which is smaller than the critical value for Ca = 1.0 and m = 0.5. On the other hand, neutral stability for m = 2.0 occurs at ka = 0.98 which is larger than the critical value for Ca = 1.0 and m = 2.0. However, for m = 1, neutral stability occurs at ka = 1 for all values of Ca. Therefore, the influence of increasing surface tension is to destabilize the flow to long wave disturbances and to make the wavenumbers for neutral stability for various m's concentrate

around ka = 1.

The effect of m and Ca on modes of maximum instability, i.e. ka for highest growth rate, is further illustrated in Fig. 5. Here, ka_{max} is plotted against Ca for m = 0.5, 1.0 and 2.0 when a = 0.7 and Re = 0.1. When m = 1, ka_{max} does not shift as Ca varies. So without the viscosity stratification, the effect of surface tension is to increase the growth rates without shifting ka_{max}. For m = 0.5, maximum instability occurs at larger ka (i.e. smaller wavelengths) than for m = 1, but the shift of ka_{max} becomes smaller as Ca decreases (i.e. surface tension increases). And for m = 2.0, on the other hand maximum instability occurs at smaller ka (i.e. larger wavelengths) than for m = 1. Again, the shift of ka_{max} becomes less as Ca decreases.

As seen above, maximum instability occurs for $0 < ka < 1$, which means that breakup occurs for disturbances whose wavelengths are greater than the circumference of the inner liquid cylinder. Also, we see that maximum instability occurs at larger values of ka as m increases from 1 and at smaller values of ka as m decreases from 1. Breakup of the cylindrical liquid produces drops whose size is of the order of λ_{max}, the wavelength for maximum instability (Levich, 1962, p. 633). Thus, a more viscous inner liquid would tend to yield larger drops when it breaks up. The effect of surface tension is to modify the viscosity effect by suppressing the shift of the modes of maximum instability relative to those for m = 1.0.

B. Effect of Re

The effect of Re is illustrated in Figs. 6, 7 and 8. In Fig. 6, the effect of Re on the stability of the interface is shown for a = 0.7, m = 2.0, Ca = ∞. Since Ca = ∞, there exists only the instability due to the viscosity difference between inner and outer fluids. It can be seen that the effect of increasing Re is to increase the

growth rates. Figure 7 shows the effect of Re when only the capillary instability is present on the interface for a = 0.7, m = 1.0, Ca = 1.0. The interface becomes more unstable as Re increases. However, the neutral stability points remain fixed at ka = 1 for all Re, and the wavenumber ka for maximum growth rate does not vary as Re increases. This means that as Re increases the effect of inertia on the capillary instability is to increase the growth rate of already unstable disturbances, without the shift of the ka for neutral stability or maximum stability.

When both surface tension and viscosity difference affect the stability of the interface simultaneously, as shown in Fig. 8 for a = 0.7, m = 2.0, Ca = 1.0, the interface becomes more unstable as Re increases. In addition, ka for neutral stability increases so that the interface becomes unstable to shorter wavelength disturbances. As Re increases, the disturbance with fastest growth rate occurs at larger ka (i.e. smaller wavelength). This result shows that as more inertia effect is present, the inner fluid will tend to break into smaller (shorter wavelength) fragments.

C. Effect of a

The effect of a on the stability of the interface is discussed for Re = 0.1. There are two mechanisms that affect the stability of the interface as the radius of the inner cylindrical core fluid varies: one is associated with the relative volume changes of the inner and outer fluid, and the other is a result of hydrodynamic influence of the tube wall. The effect of the volume change is such that an increase of a has a stabilizing effect for $m > 1$ and a destabilizing effect for $m < 1$. The influence of the wall as a increases is to stabilize the system, in a manner that longer wavelength disturbances are stabilized more than shorter wavelength disturbances. This latter behavior is illustrated in Fig. 9, for which

the effect of the relative volume change is absent because m = 1.

When the only instability is due to the viscosity difference at the interface, as shown in Fig. 10 for m = 0.5, Ca = ∞, Re = 0.1, the interface at first becomes more unstable as a increases from 0.3 due to the volume increase of the less viscous inner fluid, but beyond some critical value of a the growth factor begins to decrease with further increase of a due to the stabilizing effect of the wall. This critical value of a depends on ka. When a = 0.5, the interface is less unstable than a = 0.4 for long wavelength disturbances, but for short wavelength disturbances the interface for a = 0.5 is more unstable than for a = 0.4. This behavior is caused by the fact that the wall interaction stabilizes the long wavelength disturbances more than short wavelength disturbances as mentioned previously. The effect of varying a on the instability generated by the viscosity difference for several m's is shown in Fig. 11 for ka = 0.2, Ca = ∞, Re = 0.1. When m = 0.5, as mentioned above, the interface becomes more unstable as a increases up to about 0.4 but then becomes less unstable as a increases beyond about 0.4. When m = 1, the interface is neutrally stable because Ca = ∞ in this case. When m = 2.0, the interface is unstable for small a and the interface becomes less unstable as a increases and becomes stable beyond a = 0.23.

In Fig. 13, the effect of varying a on capillary instability is shown for m = 1.0, Ca = 1.0, Re = 0.1. For capillary instability, only the wall effect influences the stability of the interface as a varies because m = 1. Therefore, as a increases the interface becomes less unstable, but neutral stability always occurs at ka = 1. Since the wall effect stabilizes longer wavelength disturbances more than shorter wavelength disturbances, maximum instability occurs at a larger ka as a increases.

The effect of varying a when both surface tension and viscosity difference

simultaneously generate instability at the interface is shown in Figs. 12 and 14. As a increases, the interface becomes less unstable for long wavelength disturbances. It is interesting to note that for m = 0.5, neutral stability occurs at ka > 1 and increases with a while neutral stability occurs at ka < 1 when m = 2.0 and decreases with a.

As a increases, ka for maximum instability increases for all cases mentioned above except the case when m = 2.0, Ca = 1.0, Re = 0.1 (Fig. 12). In this case, when a = 0.7 the interface is unstable only for small wavenumbers so that the maximum instability occurs at a small wavenumber.

III. Conclusion

The stability of annular flow of two fluids through a circular tube has been studied. The instability considered in the present study occurs at the interface between two fluids. Linear stability analysis was carried out for axisymmetric disturbances when the mechanisms of instability due to a viscosity difference between two fluids and surface tension are simultaneously present. The effects of parameters, a, m, Ca and Re, on neutral stability points and modes of maximum instability are also reported.

When surface tension is zero and viscosities of two fluids are same, the interface is neutrally stable because there is no mechanism that generates instability for the interface-driven instability. Instabilities develop when surface tension is finite and/or viscosities of two fluids are different. When viscosities are same, only capillary instability is present for finite surface tension. And only the instability due to the viscosity difference is present when surface tension is zero and $m \neq 1$. The instability developed by the simultaneous presence of surface tension and the viscosity difference were compared with the capillary instability and the instability due to the viscosity difference. The effect of varying the

radius ratio between inner and outer fluids and Reynolds number is to modify the instability developed by the viscosity difference and surface tension.

The instability due to the viscosity difference alone was studied by Joseph et al. (1983). Unfortunately, quantitative comparison of current results with the results of Joseph et al. (1983) is not readily done because our calculations are done for small Re due to the convergence requirement of the series type solution of the Orr-Sommerfeld equation and Joseph et al. (1983) encountered numerical problems for small Re(< 1). However, qualitative comparisons between the current results and those of Joseph et al. (1983) indicate general agreement.

Appendix

The elements of the matrix **F** in Eq. (45) are given below.

$A_{11} = I_1(k)$

$A_{12} = y_a(k)$

$A_{13} = K_1(k)$

$A_{14} = y_b(k)$

$A_{15} = 0$

$A_{16} = 0$

$A_{21} = kI_0(k)$

$A_{22} = y_a'(k)$

$A_{23} = -kK_0(k)$

$A_{24} = y_b'(k)$

$A_{25} = 0$

$A_{26} = 0$

$A_{31} = aI_1(ka)$

$A_{32} = y_a(ka)$

$A_{33} = aK_1(ka)$

$A_{34} = y_b(ka)$

$A_{35} = -aI_1(ka)$

$A_{36} = -\hat{y}_a(ka)$

$$A_{41} = -kaI_0(ka) + \frac{a}{c}\left[\frac{\partial W}{\partial r}\right]_{r=a} I_1(ka)$$

$$A_{42} = -y'_a(ka) + \frac{1}{c}\left(\frac{\partial W}{\partial r}\right)_{r=a} y_a(ka)$$

$$A_{43} = kaK_0(ka) + \frac{a}{c}\left(\frac{\partial W}{\partial r}\right)_{r=a} K_1(ka)$$

$$A_{44} = -y'_b(ka) + \frac{1}{c}\left(\frac{\partial W}{\partial r}\right)_{r=a} y_b(ka)$$

$$A_{45} = kaI_0(ka) - \frac{a}{c}\left(\frac{\partial \hat{W}}{\partial r}\right)_{r=a} I_1(ka)$$

$$A_{46} = \hat{y}_a'(ka) - \frac{1}{c}\left(\frac{\partial \hat{W}}{\partial r}\right)_{r=a} \hat{y}_a(ka)$$

$$A_{51} = \left[-2k^2 + \frac{1}{c}\left(\frac{\partial^2 W}{\partial r^2}\right)_{r=a}\right] I_1(ka)$$

$$A_{52} = \left[\frac{1}{ac}\left(\frac{\partial^2 W}{\partial r^2}\right)_{r=a} - \frac{2k^2}{a} - \frac{in}{a} - \frac{Reik}{a}\right] y_a(ka)$$

$$A_{53} = \left[-2k^2 + \frac{1}{c}\left(\frac{\partial^2 W}{\partial r^2}\right)_{r=a}\right] K_1(ka)$$

$$A_{54} = \left[\frac{1}{ac}\left(\frac{\partial^2 W}{\partial r^2}\right)_{r=a} - \frac{2k^2}{a} - \frac{in}{a} - \frac{Reik}{a}\right] y_b(ka)$$

$$A_{55} = -m\left[-2k^2 + \frac{1}{c}\left(\frac{\partial^2 \hat{W}}{\partial r^2}\right)_{r=a}\right] I_1(ka)$$

$$A_{56} = \left[-\frac{m}{ac}\left(\frac{\partial^2 \hat{W}}{\partial r^2}\right)_{r=a} + \frac{m}{a}2k^2 + \frac{in}{a} + \frac{Re}{a}ik\right] \hat{y}_a(ka)$$

$$A_{61} = [2ik^2 - n - Re\,k] J_0(ka) + \left[-\frac{2ik}{a} - \frac{2ik}{c}\left(\frac{\partial W}{\partial r}\right)_{r=a} + Re\left(\frac{\partial W}{\partial r}\right)_{r=a}\right] I_1(ka)$$

$$A_{62} = \left[\frac{2ik}{a}\right] y'_a(ka)$$

$$+ \left[-\frac{2ik}{a^2} - \frac{2ik}{ac}\left(\frac{\partial W}{\partial r}\right)_{r=a} + \frac{2Re}{a}\left(\frac{\partial W}{\partial r}\right)_{r=a}\right] y_a(ka)$$

$$A_{63} = \left[-2ik^2 + n + Re\cdot k\right]K_0(ka)$$

$$+ \left[-\frac{2ik}{a} - \frac{2ik}{c}\left(\frac{\partial W}{\partial r}\right)_{r=a} + Re\left(\frac{\partial W}{\partial r}\right)_{r=a}\right]K_1(ka)$$

$$A_{64} = \left[\frac{2ik}{a}\right]y'_b(ka)$$

$$+ \left[-\frac{2ik}{a^2} - \frac{2ik}{ac}\left(\frac{\partial W}{\partial r}\right)_{r=a} + \frac{2Re}{a}\left(\frac{\partial W}{\partial r}\right)_{r=a}\right]y_b(ka)$$

$$A_{65} = \left[-2mik^2 + n + Re\cdot k\right]I_0(ka)$$

$$+ \left[\frac{2mik}{a} + \frac{2mik}{c}\left(\frac{\partial \hat{W}}{\partial r}\right)_{r=a} - Re\left(\frac{\partial \hat{W}}{\partial r}\right)_{r=a}\right.$$

$$\left. - \frac{1}{Ca}\left(-\frac{1}{a^2c} + \frac{k^2}{c}\right)\right]I_1(ka)$$

$$A_{66} = -m\left[\frac{2ik}{a}\right]\hat{y}_a'(ka) + \left\{-m\left[-\frac{2ik}{a^2} - \frac{2ik}{ac}\left(\frac{\partial \hat{W}}{\partial r}\right)_{r=a}\right.\right.$$

$$\left.\left. - \frac{1}{Ca}\left[-\frac{1}{a^3c} + \frac{k^2}{ac}\right] - \left[\frac{2Re}{a}\left(\frac{\partial \hat{W}}{\partial r}\right)_{r=a}\right]\right\}\hat{y}_a(ka)$$

References

Hickox, C. E. 1971 Instability due to viscosity and density stratification in axisymmetric pipe flow. Phys. Fluids **14**, 251.

Hooper, A. P. and Boyd, W. G. C. 1983 Shear flow instability at the interface between two viscous fluids. Phys. Fluids **28**, 1613.

Hooper, A. P. 1985 Long-wave instability at the interface between two viscous fluids: thin layer effects. Phys. Fluids **28**, 1613.

Joseph, D. D., Renardy, M. and Renardy, Y. 1983 Mathematics Research Center Technical Summary Report #2503.

Joseph, D. D., Renardy, M. and Renardy, Y. 1984 Instability of the flow of two immiscible liquids with different viscosities in a pipe. J. Fluid Mech. **141**, 309.

Levich, V. G. 1962 "Physicochemical Hydrodynamics", Prentice-Hall, N.J.

Mikami, T. and Mason, S. G. 1975 The capillary breakup of a binary liquid column inside a tube. Can. J. Chem. Eng. **53**, 372.

Plateau, M. 1873 Statique experimentale et theorique des liquides soumis aux seulea forces moleculaires, Paris.

Rayleigh, Lord 1892 On the instability of a cylinder of viscous liquid under capillary force. Phil. Mag. **34**, 145.

Renardy, Y. 1985 Instability at the interface between two shearing fluids in a channel. Phys. Fluids **28**, 3441.

Tomotika, S. 1935 On the instability of a cylindrical thread of a viscous liquid surrounded by another viscous fluid. Proc. R. Soc. London A **150**, 322.

Wason, D. T., McNamara, J. J. Shah, S. M., Sampath, K. and Aderangi, N. 1979 The role of coalescence phenomena and interfacial rheological properties in enhanced oil recovery: an overview. J. Rheol. **23**, 181

Yih, C. S. 1967 Instability due to viscosity stratification. J. Fluid Mech. **27**, 337.

Figure Captions

Figure 1: Schematic sketch of the system.

Figure 2: Dimensionless negative growth rate, n_i, as a function of the dimensionless wavenumber ka for a = 0.7, Re = 0.1, Ca = ∞.

Figure 3: Dimensionless negative growth rate, n_i, as a function of the dimensionless wavenumber ka for a = 0.7, Re = 0.1, Ca = 1.0.

Figure 4: Dimensionless negative growth rate, n_i, as a function of the dimensionless wavenumber ka for a = 0.7, Re = 0.1, Ca = 0.1.

Figure 5: Dimensionless wavenumber for maximum growth rate, $(ka)_{max}$, as a function of the capillary number Ca for a = 0.7, Re = 0.1.

Figure 6: Dimensionless negative growth rate, n_i, as a function of the dimensionless wavenumber ka for a = 0.7, m = 2.0, Ca = ∞.

Figure 7: Dimensionless negative growth rate, n_i, as a function of the dimensionless wavenumber ka for a = 0.7, m = 1.0, Ca = 1.0.

Figure 8: Dimensionless negative growth rate, n_i, as a function of the dimensionless wavenumber ka. —— for a = 0.7, m = 2.0, Ca = 1.0 with Poiseuille flow. ---- addition of growth factors for a = 0.7, m = 2.0, Ca = ∞ with Poiseuille flow and for a = 0.7, m = 2.0, Ca = 1.0 without Poiseuille flow.

Figure 9: Change in dimensionless negative growth rate with respect to the dimensionless inner radius, dn_i/da, normalized with the absolute value of the dimensionless growth rate, $|n_i|$, as a function of the dimensionless inner radius a.

Figure 10: Dimensionless negative growth rate, n_i, as a function of the dimen-

sionless wavenumber ka for m = 0.5, Ca = ∞, Re = 0.1.

Figure 11: Dimensionless negative growth rate, n_i, as a function of the dimensionless inner radius a for ka = 0.2, Ca = ∞, Re = 0.1.

Figure 12: Dimensionless negative growth rate, n_i, as a function of the dimensionless wavenumber ka for m = 2.0, Ca = 1.0, Re = 0.1.

Figure 13: Dimensionless negative growth rate, n_i, as a function of the dimensionless wavenumber ka for m = 1.0, Ca = 1.0, Re = 0.1.

Figure 14: Dimensionless negative growth rate, n_i, as a function of the dimensionless wavenumber ka for m = 0.5, Ca = 1.0, Re = 0.1.

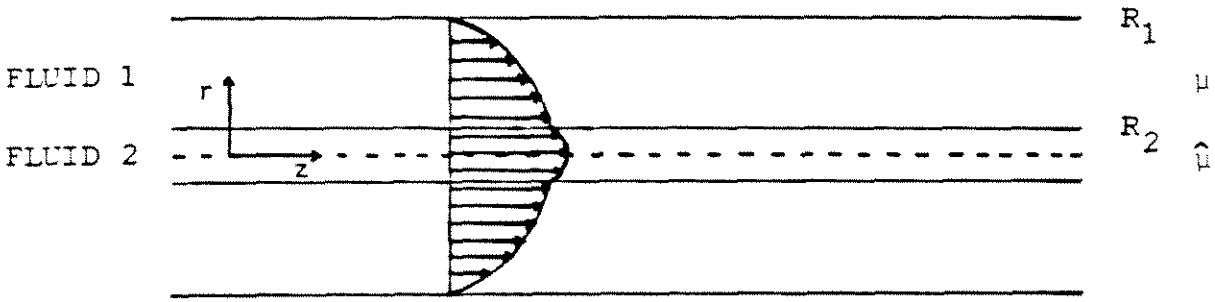

Figure 1

EFFECT OF m

a = 0.7 Re = 0.1

Ca = ∞

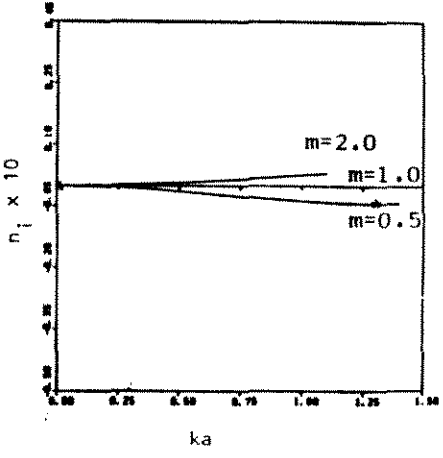

Figure 2

Ca = 1.0

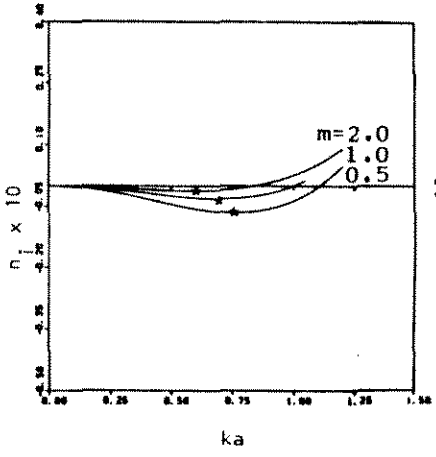

Figure 3

Ca = 0.1

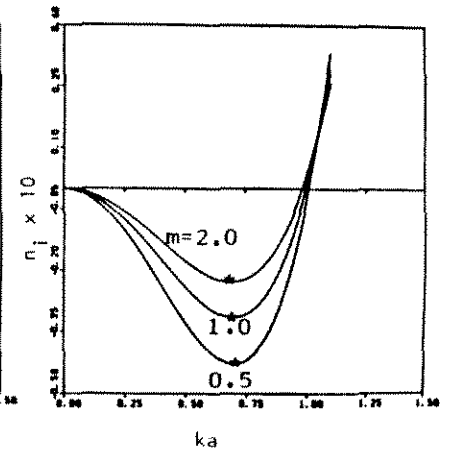

Figure 4

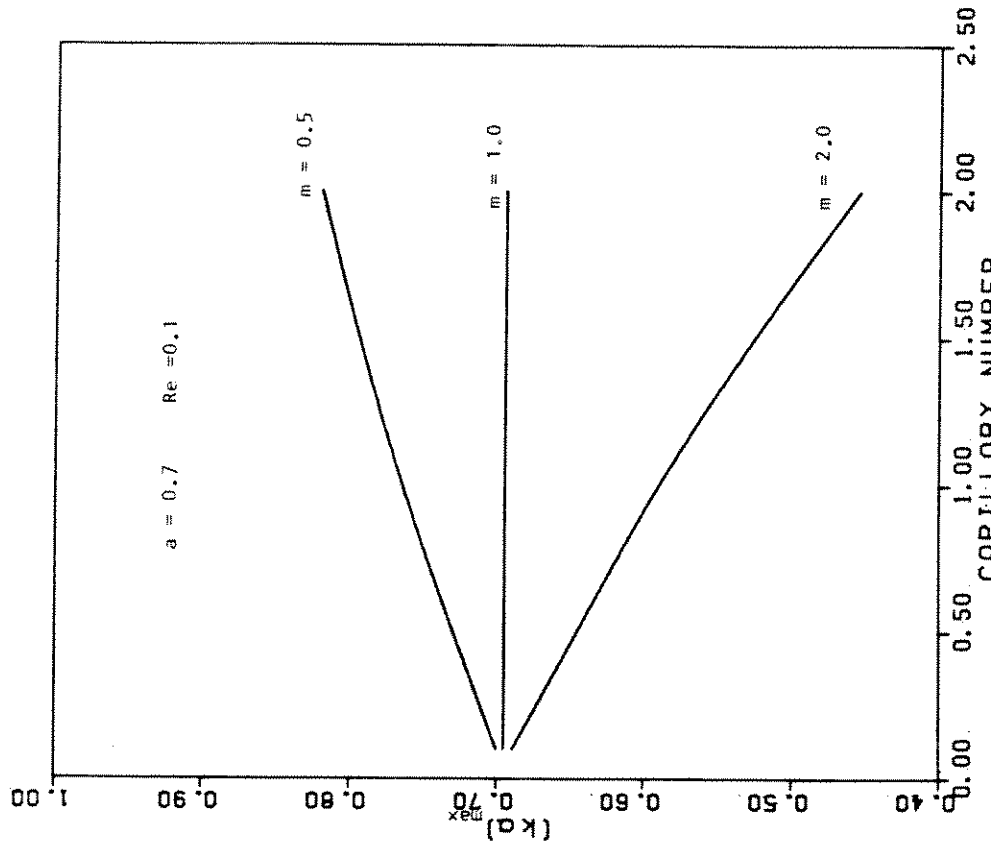
m = 0.5
m = 1.0
m = 2.0
a = 0.7
Re =0.1
CAPILLARY NUMBER
0.00
0.50
1.00
1.50
2.00
2.50
(k a)max
0.40
0.50
0.60
0.70
0.80
0.90
1.00

Figure 5

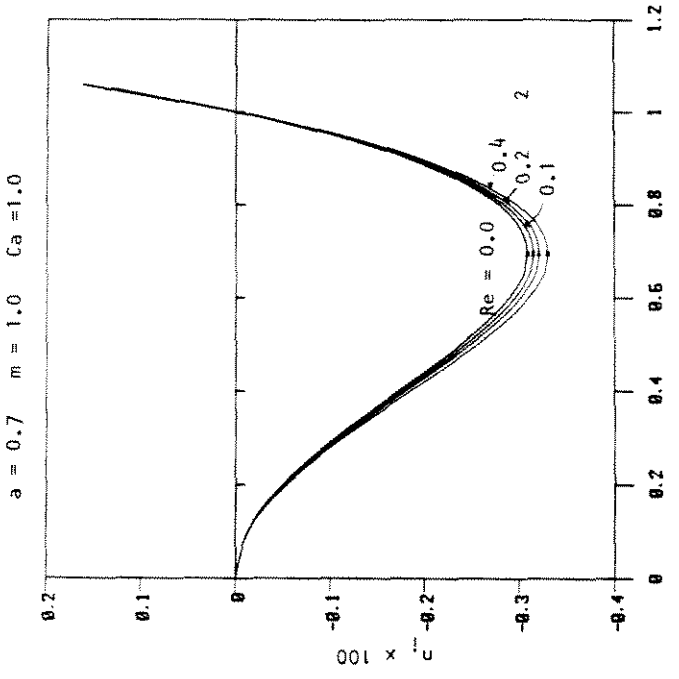

Figure 7

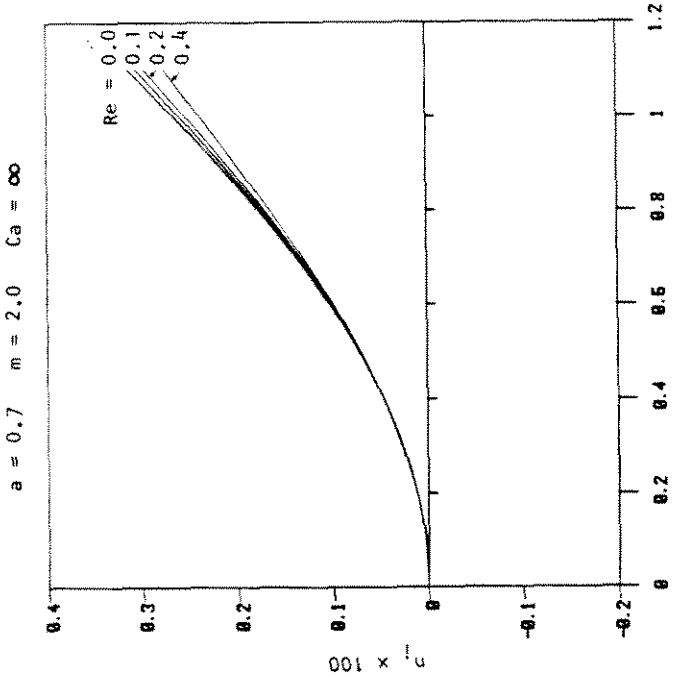

Figure 6

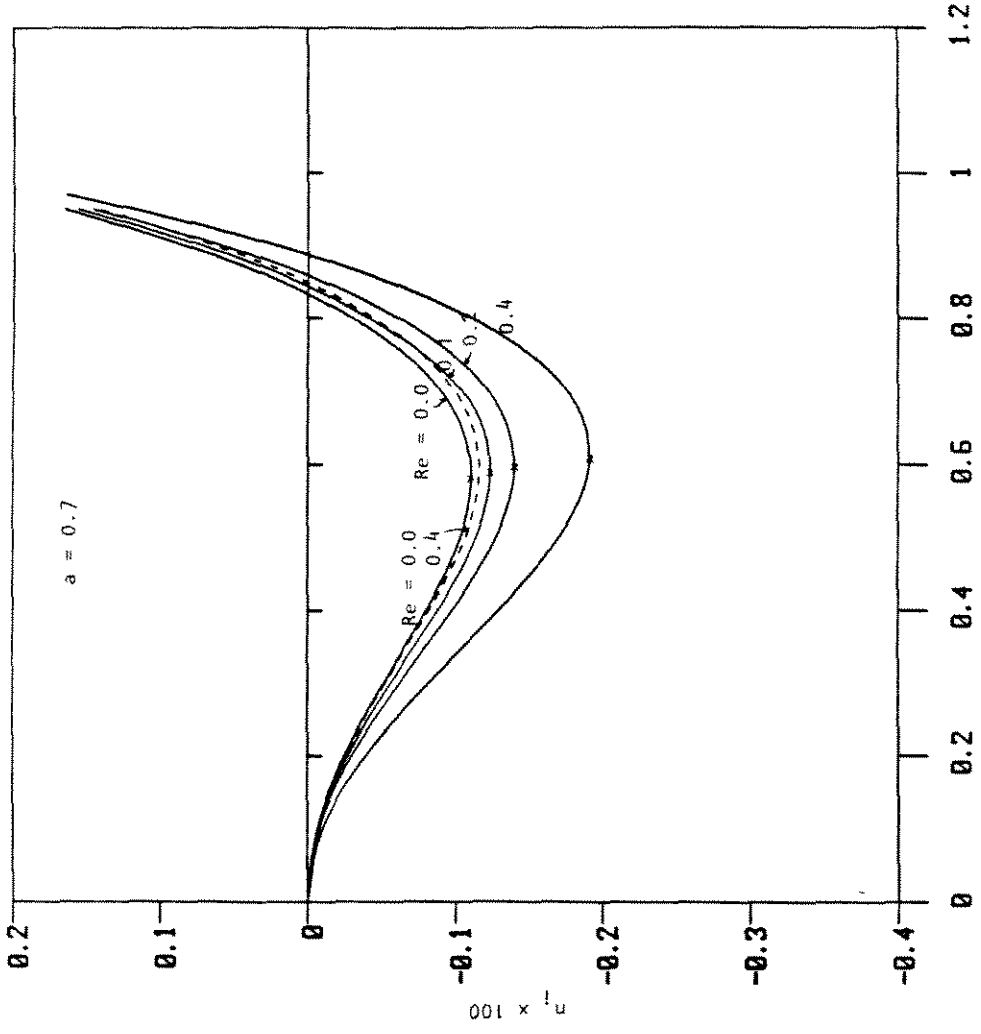
a = 0.7
Re = 0.0
0.4
Re = 0.0
0.4
0.2
0.4
$\eta_i \times 100$
ka
0.2
0.1
0
-0.1
-0.2
-0.3
-0.4
0
0.2
0.4
0.6
0.8
1
1.2

Figure 8

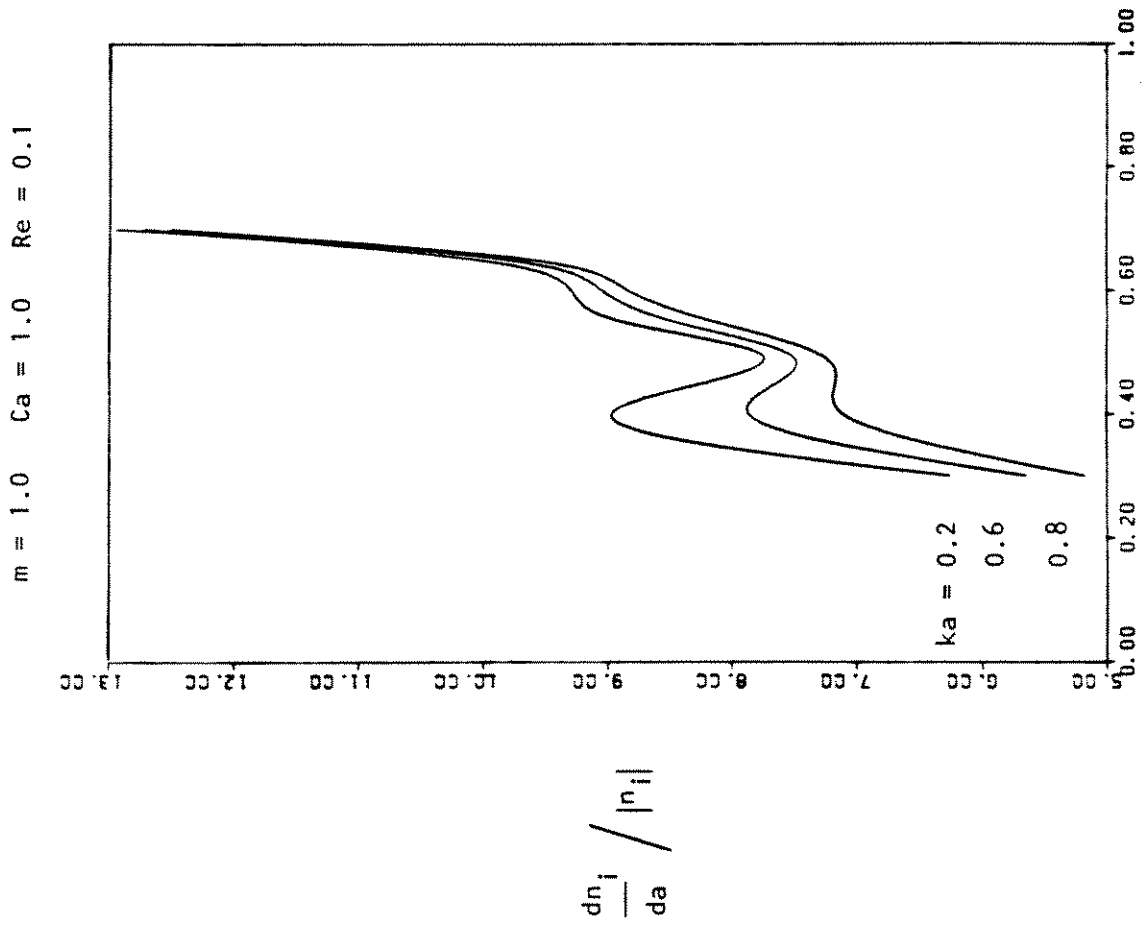
m = 1.0 Ca = 1.0 Re = 0.1
ka = 0.2
0.6
0.8
$\frac{dn_i}{da} / |n_i|$
a
0.00
0.20
0.40
0.60
0.80
1.00
5.00
6.00
7.00
8.00
9.00
10.00
11.00
12.00
13.00

Figure 9

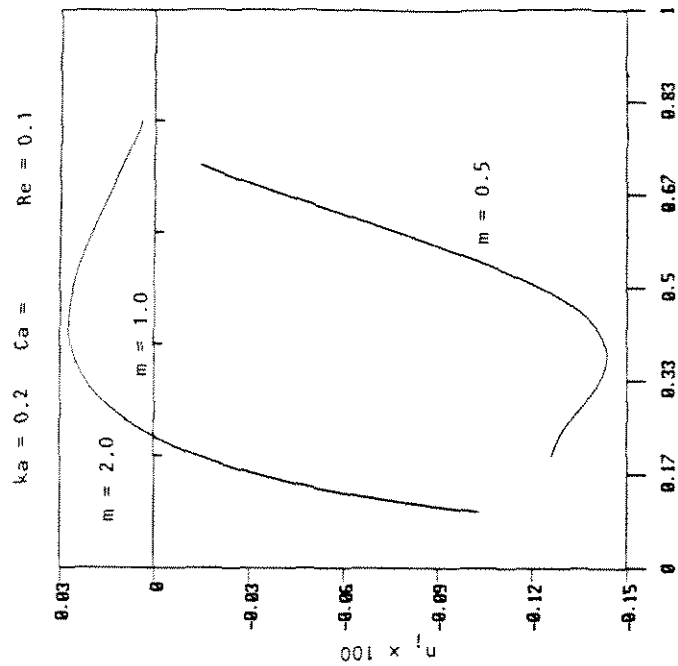

Figure 11

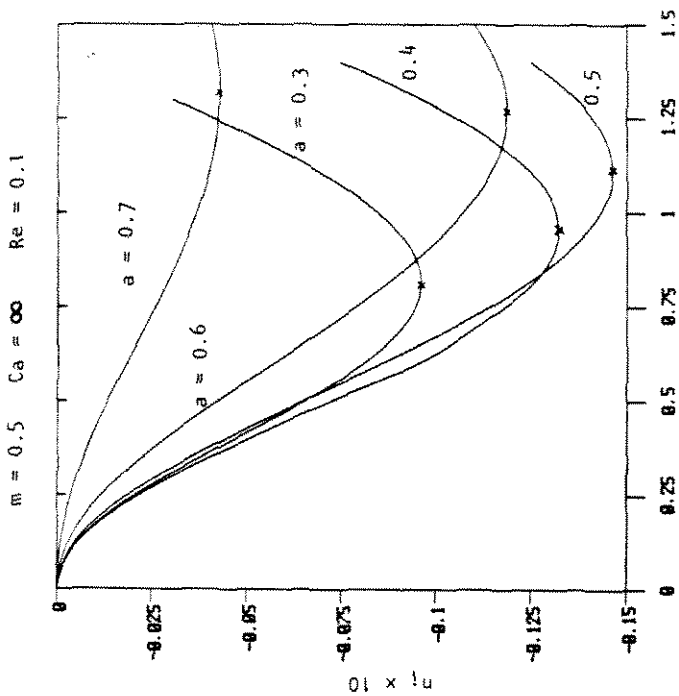

Figure 10

Ca = 1.0 Re = 0.1

m = 2.0

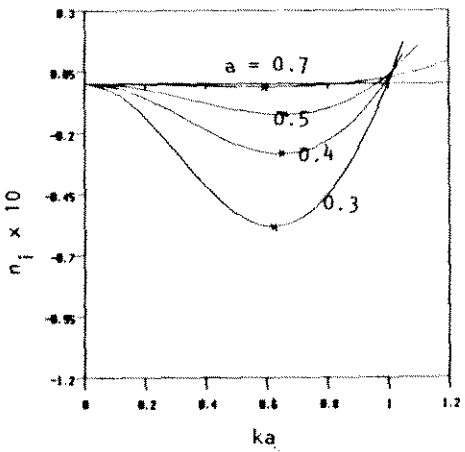

Figure 12

m = 1.0

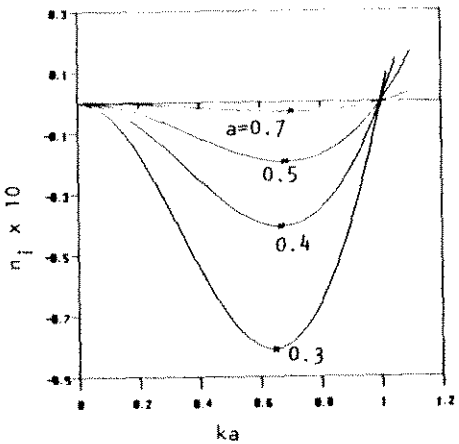

Figure 13

m = 0.5

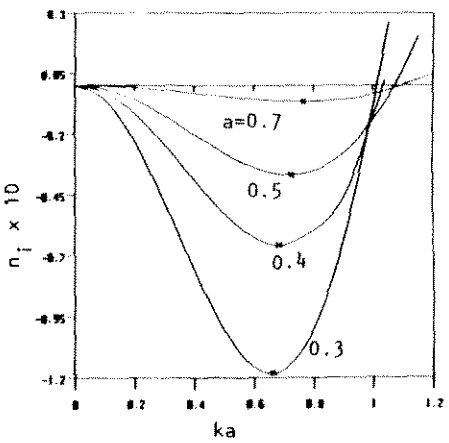

Figure 14

Chapter III.

Creeping Motion of a Deformable Drop toward a Deformable Interface

CREEPING MOTION OF A DEFORMABLE DROP TOWARD A DEFORMABLE INTERFACE

I. Introduction

When a droplet of a light liquid rises through an immiscible heavy liquid toward an interface, separating the heavy liquid and a large body of the light liquid, the droplet decelerates and the heavy liquid between the drop and the interface drains until the film ruptures and the drop coalesces with its homophase. This process is depicted in Fig. 1. The problem of a drop of a heavy liquid in a light bulk phase can be obtained by simply inverting the configuration of Fig. 1. The coalescence problem described above is of particular interest in the final separation stages of liquid-liquid extraction processes where droplets of light liquid rise through heavy liquid and droplets of heavy liquid fall through light liquid toward the common interface between the bulk phases.

When fluid 1 is the same as fluid 3 (see Fig. 1), i.e. $\rho_1 = \rho_2$, it is generally assumed that the rate determining step in the coalescence process is film drainage. The result of the current calculation indeed shows that this is true. The velocity of the drop obtained in the present calculation reaches almost zero abruptly, as the drop approaches the interface as if the drop really does come to rest. Indeed, the rate of coalescence is frequently characterized via a so-called "rest time", defined as the time interval between arrival of the drop at the interface and coalescence, Charles and Mason (1960). The rest time is dependent upon the rate at which the thin liquid film between the drop and the interface drains as a function of time.

Most theoretical attempts to model coalescence have been concerned with the film drainage step alone, with te goal of determining the "rest time" for

assumed initial shapes of the interface and the drop. Provided that physically correct initial shapes are used, such models can give predictions for the "rest time". Attempts to model the film drainage step are summarized by Woods and Burrill (1972). Charles and Mason (1960) estimated the rate of thinning by considering two rigid parallel disks. In the film of liquid between the two parallel discs, a parabolic profile was assumed with no-slip on the surfaces of the discs. Their work was extended by Frankel and Mysels (1962) and Princen (1963) who allowed for curvature of the interfaces, and either a mobile or immobile surface/interface on the drop surface and the interface. For a mobile interface, the shear stress on the interface was assumed to be zero, while the tangential velocity was set to zero for an immobile interface. Burrill and Woods (1969) attempted to predict the shape of the interface and the drop a posteriori by assuming an empirical correlation for the pressure distribution in the film region. This empirical correlation was included in equilibrium force balances on the drop surface and the interface in the film region, and coefficients of the empirical correlation were determined by trial and error by comparing the experimental film thickness with the predicted film thickness between the calculated interface and drop shapes. Using an experimental profile of the draining film, i.e. the interface and drop shapes, as an initial condition, Hartland (1970) developed an analysis to predict the interface shape and the drop shape as a function of time for small variations of the drop surface and the interface from spherical shapes. Jones and Wilson (1978) carried out an asymptotic analysis for the drop and interface shapes using the ratio of film thickness to radius of a spherical drop as the small parameter. However, they were not able to solve the resulting integro-differential equations. Lin and Slattery (1982) recently considered the case when the drop surface and interface are immobile, for which the tangential components of velocity are zero due to the possible existence of

surfactant gradients. The dependence of the drop surface and the interface upon the radial direction is assumed to be weak. Chen, Hahn and Slattery (1984) later extended Lin and Slattery's (1982) analysis to include the effect of London-van der Waals forces.

In all of the above theoretical developments, the investigators considered only the motion in the thin film region, and either no-slip (immobile interface) and zero tangential stress (mobile interface) as boundary conditions on the drop surface and the interface. Therefore, the physical properties of the drop fluid (and the upper bulk fluid) were not included in the analyses. Also, a certain initial shape was assumed for the drop surface and the interface, either "a priori" or taken from experiments, and the lubrication approximation is applied to the very thin film region for which the ratio of the film thickness to the radius of a spherical drop is very small. One recent departure from this pattern, however, was reported by Chervenivanova and Zapryanov (1985) who used a domain perturbation technique to study the shapes of the drop and of the interface, including the physical properties of the drop fluid (upper bulk fluid). However, their results are restricted to the cases when the drop is relatively far away from the interface because they considered only small deviations from a spherical drop and a flat interface.

The majority of experimental investigations of drop coalescence were performed by releasing a drop formed at the tip of a needle very near an interface. Allan, Charles and Mason (1961), MacKay and Mason (1963), and Princen and Mason (1965) used a light interference technique to measure the film thickness and rest time. Hartland (1967a-d,1969) used a capacitance technique to measure the film thickness and also presented experimental pictures of overall shapes of the drop near the interface. For a pure interface and interfaces with controlled addition of surfactants, Hodgson and Woods (1969) and Burrill and

Woods (1973) also used the light interference technique to study film drainage. For the pure systems, the interface was cleaned very carefully by removing the contamination from the interface. They found that for pure systems symmetrical drainage occurred, but that unsymmetrical drainage occurred when a moderate concentration of surfactants exists on the interface. If the concentration of surfactants was increased to still higher values, the film again drained symmetrically.

Lee and Leal (1982) and Geller, Lee and Leal (1985) carried out numerical studies of a rigid sphere moving normal to an initially flat but deformable interface. In this paper, we report on a complementary numerical study of the approach of a deformable drop toward a deformable interface using the same boundary integral technique. We restrict our solutions for drop and interface shape to an axisymmetric form, and thus limit our solutions to the so-called symmetric drainage mode, as is relevant if the interface is uncontaminated (assumed implicitly in the boundary conditions for our numerical solution). The objective of the present work is to calculate the shapes of the drop and the interface and the velocity of the drop as it approaches the interface. In the current work, unlike the film drainage theories, we consider the complete problem, starting with a drop at some distance from the interface, and including motion both within the drop and in the upper bulk fluid. Furthermore, no restriction is imposed on the deformation of the interface and the drop. The initial configuration has the drop several radii (usually three radii) from an undeformed flat interface. This initial configuration enables the observation of the evolution of the shapes of the drop and the interface as the drop approaches the interface. As the film between the drop and the upper bulk fluid becomes thin, the time step must become smaller, and current computation is terminated when the cost of further calculation becomes unacceptably large.

Consequently, the drainage of a very thin film is not studied in the current work. However, the calculation could be continued using the film drainage theory with the final shape obtained from the current computation as an initial shape for the film drainage theory. Eventually, instability must be considered to complete our understanding of the coalescence phenomenon. We consider gravity, interfacial and viscous forces. London-van der Waal's forces and electrostatic forces are neglected, but will be the subject of a subsequent study. These forces become significant only when the film thickness becomes very thin (1000 Å).

II. Formulation

We consider the approach of a droplet of a light liquid (fluid 1), through an immiscible heavy liquid (fluid 2), normal to an initially flat interface which separates the heavy bulk fluid (fluid 2) and another light bulk fluid (fluid 3), as indicated in Fig. 1. All fluids are Newtonian. In the calculation reported later in this paper, we will restrict our attention to systems for which the drop and the upper bulk fluid are the same, i.e. fluid 1 = fluid 3. Here, however, the formulation is carried out for the light drop rising through the heavy fluid toward a second light fluid. The governing equations and boundary conditions for the case when a heavy drop falls through a light fluid are identical.

We assume that the creeping motion approximation is applicable to the motion of the drop, and thus all inertial effects are neglected. The resulting solutions are therefore valid when

$$\mathrm{Re} = \frac{u_c l_c \rho_2}{\mu_2} << 1 \tag{1}$$

where u_c is chosen as the velocity of a spherical drop in an unbounded fluid 2, U_∞, and l_c is the undeformed drop radius a. Since the drop moves as a consequence of buoyancy,

$$U_\infty = \frac{2}{9} \frac{ga^2(\rho_2 - \rho_1)}{\mu_2} \frac{1}{\beta}$$

where

$$\beta = \left(1 + \frac{2}{3\lambda_1}\right) \Big/ \left(1 + \frac{1}{\lambda_1}\right) \text{ and } \lambda_1 = \frac{\mu_1}{\mu_2}.$$

This characteristic velocity is an upper bound on the actual velocity of the drop, because the drop velocity decreases as the drop approaches the interface. Therefore Eq. (1) represents a conservative estimate of the conditions necessary to neglect inertial effects.

The governing differential equations in dimensionless form are then

$$-\nabla p_1 + \lambda_1 \nabla^2 \mathbf{u}_1 = 0$$

$$\nabla \cdot \mathbf{u}_1 = 0 \quad \text{for fluid 1} \tag{3}$$

$$-\nabla p_2 + \nabla^2 \mathbf{u}_2 = 0$$

$$\nabla \cdot \mathbf{u}_2 = 0 \quad \text{for fluid 2} \tag{4}$$

$$-\nabla p_3 + \lambda_3 \nabla^2 \mathbf{u}_3 = 0$$

$$\nabla \cdot \mathbf{u}_3 = 0 \quad \text{for fluid 3} \tag{5}$$

with the following characteristic variables

$$u_c = U_\infty$$

$$l_c = a$$

$$p_c = \frac{\mu_2 U_\infty}{a} .$$

In Eq. (5), $\lambda_3 = \mu_3/\mu_2$.

We have adopted a global coordinate system that is fixed at the undeformed flat interface, as indicated in Fig. 1, with z = 0 corresponding to the plane of the undeformed interface. Then, the boundary conditions at large distances from the drop are

$$\mathbf{u}_2, \mathbf{u}_3 \to 0 \quad \text{as} \quad |\mathbf{x}| \to \infty . \tag{6}$$

On the interface surface, $\mathbf{x} \in S_I$, we require

$$\mathbf{u}_2 = \mathbf{u}_3 \tag{7}$$

$$\mathbf{n}_3 \cdot \mathbf{T}_2 - \lambda_3 \mathbf{n}_3 \cdot \mathbf{T}_3 = \mathbf{n}_3 \frac{1}{Ca_3} \nabla \cdot \mathbf{n}_3 - \frac{1}{Cg_3} h \mathbf{n}_3 \tag{8}$$

$$\mathbf{n}_3 \cdot \mathbf{u}_2 = \mathbf{n}_3 \cdot \mathbf{u}_3 = \frac{1}{|\nabla H|} \frac{\partial h}{\partial t} \tag{9}$$

where the interface shape is described as z = h(r,t), and $\mathbf{n}_3$ denotes the unit normal vector into fluid 2 at the interface, $\mathbf{n}_3 = -\nabla H/|\nabla H|$ with $H \equiv z - h(r,t)$. In Eq. (8), Ca_3 dentes the capillary number for the interface, $\mu_2 U_\infty/\gamma_{23}$ and $Cg_3 = \mu_2 U_\infty/ga^2(\rho_2 - \rho_3)$ where γ_{23} is the interfacial tension between fluids 2 and 3. The stress $\mathbf{T}_i$ is the total stress minus the hydrostatic contribution, and therefore the body force term appears explicitly in the boundary condition (8), rather than appearing in the governing differential equations. On the drop surface, $\mathbf{x} \in S_D$,

$$\mathbf{u}_1 = \mathbf{u}_2 \tag{10}$$

$$\mathbf{n}_1 \cdot \mathbf{T}_2 - \lambda_1 \mathbf{n}_1 \cdot \mathbf{T}_1 = \mathbf{n}_1 \frac{1}{Ca_1} \nabla \cdot \mathbf{n}_1 - \frac{1}{Cg_1} (f - L)\cos\theta \mathbf{n}_1 \tag{11}$$

$$\mathbf{n}_1 \cdot \left(\mathbf{u}_1 + \frac{\partial L}{\partial t} \mathbf{i}_z \right) = \mathbf{n}_1 \cdot \left(\mathbf{u}_2 + \frac{\partial L}{\partial t} \mathbf{i}_z \right) = \frac{1}{|\nabla F|} \frac{\partial f}{\partial t} \tag{12}$$

In writing the boundary conditions (10)-(12), we again utilized the global coordinate system that is fixed at the undeformed flat interface. However, it is convenient to describe the drop shape in terms of a local spherical coordinate system. The origin of this local coordinate system is located at the center of mass of the drop and is related to the origin of the global coordinate system by L(t) as shown in Fig. 1. Then, dL/dt denotes the velocity of the center of mass of the drop. In Eq. (12), dL/dt is included because the present problem is solved in the global coordinate system fixed at the undeformed flat interface. The function f for drop shape is related to the position of its surface, as $\hat{r}_s = f(\hat{\theta},t)$. Here, $\hat{}$s denote the variables in the local spherical coordinate system.. In Eqs. (11) and (12), $\mathbf{n}_1$ is the outer normal at the drop surface,

$$\mathbf{n}_1 = \nabla F / |\nabla F|$$

where

$$F \equiv \hat{r}_s - f(\hat{\theta},t) .$$

In Eq. (11), Ca_1 denotes the capillary number based upon the interfacial tension at the drop surface, $\mu_2 U_\infty / \gamma_{12}$, and $Cg_1 = \mu_2 U_\infty / g a^2 (\rho_2 - \rho_1)$, where γ_{12} is the interfacial tension between fluids 1 and 2. Using the definition of U_∞ in Eq. (2), Cg_1 can be expressed as $2/9\beta$. Then Eq. (11) becomes

$$\mathbf{n}_1 \cdot \mathbf{T}_2 - \lambda_1 \mathbf{n}_1 \cdot \mathbf{T}_1 = \mathbf{n}_1 \frac{1}{Ca_1} \nabla \cdot \mathbf{n}_1 - \frac{9}{2} \beta (f - L) \cos\hat{\theta} \mathbf{n}_1 . \tag{11a}$$

Equation (11) includes both the continuity of tangential stress and the normal stress jump condition at the drop surface. It is important to note that a solution of the creeping flow Eqs. (3)-(5) satisfying the boundary conditions in Eq.

(11) will automatically satisfy a macropscopic force balance on the drop. In particular in the present problem, the drag force on the drop will equal the buoyancy force at all times. The equations and boundary conditions (3)-(11) are sufficient to completely determine the velocity and pressure fields in the three fluids, as well as the shapes of the interface and the drop and the velocity of the center of mass of the drop, without need to impose the macroscopic force balance on the drop. Indeed, the macroscopic force balance is not independent of these equations and boundary conditions. In the Appendix, the macroscopic force balance on the drop is derived from the stress conditions in Eq. (11), and the equations of motion.

Independent dimensionless parameters in the present problem are

$$Ca_1 = \frac{\mu_2 U_\infty}{\gamma_{12}}$$

$$Ca_3 = \frac{\mu_2 U_\infty}{\gamma_{23}}$$

$$Cg_3 = \frac{\mu_2 U_\infty}{ga^2(\rho_2 - \rho_3)}$$

$$\lambda_1 = \frac{\mu_1}{\mu_2}$$

and

$$\lambda_3 = \frac{\mu_3}{\mu_2}.$$

Now, the problem is to solve (3)-(5) subject to boundary conditions (6)-(12). The problem considered here is both nonlinear and unsteady due to the boundary conditions (8), (9), (11) and (12). However, the governing equations are

linear. Therefore, as in the works of Lee and Leal (1982) and Geller, Lee and Leal (1985), we can represent the solution in terms of boundary distributions of the fundamental solution of Stokes equations due to Ladyzhenskaya (1963). In this formulation, the pressure and velocity at any point in the fluid domain are obtained in an integral representation by distributing point singularities on the boundaries of the fluid domain. Thus, for an arbitrary point $\mathbf{x}$ in the domain,

$$\mathbf{u}(\mathbf{x}) = \frac{1}{8\pi}\int_S \left[\frac{\mathbf{I}}{R} + \frac{(\mathbf{x}-\boldsymbol{\eta})(\mathbf{x}-\boldsymbol{\eta})}{R^3}\right]\cdot\mathbf{T}(\boldsymbol{\eta})\cdot\mathbf{n}dS_\eta$$

$$-\frac{3}{4\pi}\int_S \frac{(\mathbf{x}-\boldsymbol{\eta})(\mathbf{x}-\boldsymbol{\eta})(\mathbf{x}-\boldsymbol{\eta})}{R^5}\cdot\mathbf{u}(\boldsymbol{\eta})\cdot\mathbf{n}dS_\eta \qquad (13)$$

$$p(\mathbf{x}) = \frac{1}{2\pi}\int_S \left[\frac{\mathbf{I}}{R} - \frac{3(\mathbf{x}-\boldsymbol{\eta})(\mathbf{x}-\boldsymbol{\eta})}{R^5}\right]\cdot\mathbf{u}(\boldsymbol{\eta})\cdot\mathbf{n}dS_\eta$$

$$+\frac{1}{4\pi}\int_S \frac{(\mathbf{x}-\boldsymbol{\eta})}{R^3}\cdot\mathbf{T}(\boldsymbol{\eta})\cdot\mathbf{n}dS_\eta \qquad (14)$$

where $\boldsymbol{\eta}$ denotes a position on a bounding surface of the fluid domain, $\mathbf{n}$ is the outer normal to this surface, and $R = |\mathbf{x}-\boldsymbol{\eta}|$. In fluid 2, the bounding surface S includes both the drop surface and the interface. Fluids 1 and 3 each have one boundary, the drop surface and the interface, respectively. As is well known, cf. Lee and Leal (1982), the double layer potentials, i.e. the second terms in Eqs. (13) and (14), are not continuous, but suffer a jump at the boundaries.

Using the jump conditions for the double layer potentials (Ladyzhenskaya, 1963), the general solutions (13) and (14) are applied at the boundaries. First, applying (13) at the boundary of fluid 1, we obtain for $\mathbf{x}\in S_D$,

$$\frac{1}{2}\lambda_1\mathbf{u}^D(\mathbf{x}) = \frac{1}{8\pi}\int_{S_D}\left[\frac{\mathbf{I}}{R}+\frac{\mathbf{rr}}{R^3}\right]\cdot\lambda_1\mathbf{T}_1^D(\boldsymbol{\eta})\cdot\mathbf{n}_1dS_D - \frac{3}{4\pi}\lambda_1\int_{S_D}\left[\frac{\mathbf{rrr}}{R^5}\right]\cdot\mathbf{u}^D(\boldsymbol{\eta})\cdot\mathbf{n}_1dS_D$$

where $\mathbf{r} = \mathbf{x}-\boldsymbol{\eta}$ and subscripts and superscripts D indicate variables evaluated

at the surface. $\mathbf{T}_1^D$ is the stress tensor evaluated as the drop surface is approached from fluid 1. Applying (13) to the body of fluid 2, we obtain for $\mathbf{x}\in S_D$,

$$\frac{1}{2}\mathbf{u}^D(\mathbf{x}) = -\frac{1}{8\pi}\int_{S_D}\left[\frac{\mathbf{I}}{R}+\frac{\mathbf{rr}}{R^3}\right]\cdot\mathbf{T}_2^D(\eta)\cdot\mathbf{n}_1 dS_D - \frac{1}{8\pi}\int_{S_I}\left[\frac{\mathbf{I}}{R}+\frac{\mathbf{rr}}{R^3}\right]\cdot\mathbf{T}_2^I(\eta)\cdot\mathbf{n}_3 dS_I$$

$$+\frac{3}{4\pi}\int_{S_D}\left[\frac{\mathbf{rrr}}{R^5}\right]\cdot\mathbf{u}^D(\eta)\cdot\mathbf{n}_1 dS_D + \frac{3}{4\pi}\int_{S_I}\left[\frac{\mathbf{rrr}}{R^5}\right]\cdot\mathbf{u}^I\cdot\mathbf{n}_3 dS_I \qquad (16)$$

and for $\mathbf{x}\in S_I$,

$$\frac{1}{2}\mathbf{u}^I(\mathbf{x}) = -\frac{1}{8\pi}\int_{S_D}\left[\frac{\mathbf{I}}{R}+\frac{\mathbf{rr}}{R^3}\right]\cdot\mathbf{T}_2^D(\eta)\cdot\mathbf{n}_1 dS_D - \frac{1}{8\pi}\int_{S_I}\left[\frac{\mathbf{I}}{R}+\frac{\mathbf{rr}}{R^3}\right]\cdot\mathbf{T}_2^I(\eta)\cdot\mathbf{n}_3 dS_I$$

$$+\frac{3}{4\pi}\int_{S_D}\left[\frac{\mathbf{rrr}}{R^5}\right]\cdot\mathbf{u}^D(\eta)\cdot\mathbf{n}_1 dS_D + \frac{3}{4\pi}\int_{S_I}\left[\frac{\mathbf{rrr}}{R^5}\right]\cdot\mathbf{u}^I(\eta)\cdot\mathbf{n}_3 dS_I \qquad (17)$$

Here, subscripts and superscripts I indicate quantities evaluated at the bulk interface. For example, $\mathbf{T}_2^D$ is the stress tensor evaluated as the drop surface is approached from fluid 2, and $\mathbf{T}_2^I$ is the stress tensor evaluated as the interface is approached from fluid 2. Finally, applying (13) to the body of fluid 3, we obtain for $\mathbf{x}\in S_I$,

$$\frac{1}{2}\lambda_3\mathbf{u}^I(\mathbf{x}) = \frac{1}{8\pi}\int_{S_I}\left[\frac{\mathbf{I}}{R}+\frac{\mathbf{rr}}{R^3}\right]\cdot\lambda_3\mathbf{T}_3^I(\eta)\cdot\mathbf{n}_3 dS_I - \frac{3}{4\pi}\lambda_3\int_{S_I}\left[\frac{\mathbf{rrr}}{R^5}\right]\cdot\mathbf{u}^I(\eta)\cdot\mathbf{n}_3 dS_I \qquad (18)$$

where $\mathbf{T}_3^I$ is the stress tensor evaluated as the interface is approached from fluid 3.

The stress at the drop surface, $\mathbf{T}_1^D$, can be eliminated from (15) and (16) using the boundary condition (11). To do this, we add (15) and (16) together to give

$$\frac{1}{2}(\lambda_1 + 1)\mathbf{u}^D(\mathbf{x}) = -\frac{1}{8\pi}\int_{S_D}\left[\frac{\mathbf{I}}{R} + \frac{\mathbf{rr}}{R^3}\right]\cdot\mathbf{Q}^D(f)dS_D - \frac{1}{8\pi}\int_{S_I}\left[\frac{\mathbf{I}}{R} + \frac{\mathbf{rr}}{R^3}\right]\cdot\mathbf{T}_2^I(\eta)\cdot\mathbf{n}_3 dS_I$$

$$+ \frac{3}{4\pi}(1-\lambda_1)\int_{S_D}\left[\frac{\mathbf{rrr}}{R^5}\right]\cdot\mathbf{u}^D(\eta)\cdot\mathbf{n}_1 dS_D + \frac{3}{4\pi}\int_{S_I}\left[\frac{\mathbf{rrr}}{R^5}\right]\cdot\mathbf{u}^I(\eta)\cdot\mathbf{n}_3 dS_I$$

Here, the function $\mathbf{Q}^D(f)$ is the stress difference at the drop,

$$\mathbf{Q}^D(f) = \mathbf{n}_1\cdot\mathbf{T}_2 - \lambda_1\mathbf{n}_1\cdot\mathbf{T}_1$$

$$= \mathbf{n}_1\frac{1}{Ca_1}\left\{\frac{K_D}{f}(3-K^2) - \frac{K_D}{f^2}\left[\frac{\cos\theta}{\sin\theta}\left(\frac{\partial f}{\partial\theta}\right) + K_D^2\left(\frac{\partial^2 f}{\partial\theta^2}\right)\right\} - \frac{9}{2}\beta(f-L)\cos\theta\mathbf{n}_1 \quad (20)$$

with

$$K_D = \frac{1}{\left[1 + \frac{1}{f^2}\left(\frac{\partial f}{\partial\theta}\right)^2\right]^{1/2}}.$$

Similarly, Eqs. (17) and (18) can be added together to eliminate $\mathbf{T}_3^D$, using the boundary condition (8).

$$\frac{1}{2}(\lambda_3 + 1)\mathbf{u}^I(\mathbf{x}) = -\frac{1}{8\pi}\int_{S_D}\left[\frac{\mathbf{I}}{R} + \frac{\mathbf{rr}}{R^3}\right]\cdot\mathbf{T}_2^D(\eta)\cdot\mathbf{n}_1 dS_D - \frac{1}{8\pi}\int_{S_I}\left[\frac{\mathbf{I}}{R} + \frac{\mathbf{rr}}{R^3}\right]\cdot\mathbf{Q}^I(h)dS_I$$

$$+ \frac{3}{4\pi}\int_{S_D}\left[\frac{\mathbf{rrr}}{R^5}\right]\cdot\mathbf{u}^D(\eta)\cdot\mathbf{n}_1 dS_D + \frac{3}{4\pi}(1-\lambda_3)\int_{S_I}\left[\frac{\mathbf{rrr}}{R^5}\right]\cdot\mathbf{u}^I(\eta)\cdot\mathbf{n}_3 dS_I \quad (21)$$

where, $\mathbf{Q}^I(h)$ is the stress difference at the interface.

$$\mathbf{Q}^I(h) = \mathbf{n}_3\cdot\mathbf{T}_2 - \lambda_3\mathbf{n}_3\cdot\mathbf{T}_3$$

$$= \mathbf{n}_3\frac{1}{Ca_3}\left\{\frac{K_D}{r}\left(\frac{\partial h}{\partial r}\right) + K_I^3\left(\frac{\partial^2 h}{\partial r^2}\right)\right\} + \frac{1}{Cg_3}h\mathbf{n}_3 \quad (22)$$

with

$$K_I = \frac{1}{\left[1 + \left(\frac{\partial h}{\partial r}\right)^2\right]^{1/2}}.$$

For specified shapes of the drop and the interface, Eqs. (16), (17), (19) and (21) can be solved to obtain $\mathbf{u}^D$, $\mathbf{u}^I$, $\mathbf{T}_2^D$ and $\mathbf{T}_2^I$. The resulting solution satisfies the original Stokes Eqs. (3)-(5), plus the conditions (7) and (8) at the interface, (10) and (11) at the drop surface and (6) far from the drop. All that remain are the kinematic conditions (9) and (12), which can be used to increment the interface shape and the drop shape to a time Δt later, respectively.

The kinematic conditions (9) and (12) are applied in the approximate form

$$h_{j+1} = h_j + [\mathbf{u}_j^I \cdot \mathbf{n}_{3j}]\Delta t \, \frac{1}{K_{I_j}} \quad \text{for Eq. (9)} \tag{23}$$

and

$$f_{j+1} = f_j + \left[\left(\mathbf{u}_j^D + \frac{L_{j+1} - L_j}{\Delta t}\mathbf{i}_z\right) \cdot \mathbf{n}_{1j}\right]\Delta t \, \frac{1}{K_{D_j}} \quad \text{for Eq. (12)} \tag{24}$$

The variables with the subscript j are known quantities at jth time step. In Eq. (24), L_{j+1} must be known before Eq. (24) can be used to obtain a new shape. L_{j+1} is determined by the condition that the origin of the local coordinate system used to describe the drop shape is located at the center of mass of the drop at every time step. Then,

$$\hat{z}_0 = 0 \, \frac{\int \rho \hat{z} dV_D}{\int \rho dV_D} \tag{25}$$

where $\hat{z}_0$ denotes the center of mass in the local coordinate system. For constant density ρ, Eq. (25) becomes

$$0 = \int \hat{z} dV_D \tag{26}$$

In the local spherical coordinate system, Eq. (26) becomes

$$0 = 2\pi \int_{\hat{\theta}=0}^{\pi} \int_{\hat{r}_S=0}^{f} \hat{r}_S^3 \cos\hat{\theta} \sin\hat{\theta} d\hat{\theta} d\hat{r}_S \,. \tag{27}$$

after integrating in the azimuthal direction. Letting $\hat{\eta} = \cos\hat{\theta}$, Eq. (27) becomes

$$0 = \frac{2\pi}{4} \int_{\hat{\eta}=-1}^{1} f^4 \hat{\eta} d\hat{\eta} \,. \tag{28}$$

Equation (28) must be satisifed at every time step.

$$0 = \int_{\hat{\eta}=-1}^{1} f_j^4 \hat{\eta} d\hat{\eta} = \int_{\hat{\eta}=-1}^{1} f_{j+1}^4 \hat{\eta} d\hat{\eta} \,. \tag{29}$$

Then, at j+1 th time step,

$$0 = \int_{\hat{\eta}=-1}^{1} (f_j + \Delta f_j)^4 \hat{\eta} d\hat{\eta} \tag{30}$$

where

$$\Delta f_j = \frac{1}{K_{D_j}} \left(\mathbf{u}_j^p + \frac{L_{j+1} - L_j}{\Delta t} \mathbf{i}_z \right) \cdot \mathbf{n}_{1_j} \Delta t$$

as given by the kinematic condition in Eq. (24). Then, L_{j+1} is determined by satisfying Eq. (30).

The volume of the drop was conserved at each time step by calculating the volume of the drop and adjusting $f(\hat{\theta})$ to keep the constant dimensionless volume of $\frac{4}{3}\pi k^3$. The change in the volume of the drop was so small at each time step that the shape of the drop was hardly changed. However, the volume of the drop is adjusted at each time step to avoid the accumulation of the change in volume.

Since the drop is assumed to approach the interface symmetrically, the sur-

face integrals in (16), (17), (19) and (21) can be reduced to line integrals by analytically integrating in the azimuthal direction. Thus, for axisymmetric flows, Eqs. (16), (17), (19) and (21) become

$$\frac{1}{2}\begin{bmatrix} u_r^D(\mathbf{x}) \\ u_z^D(\mathbf{x}) \end{bmatrix} = -\frac{1}{8\pi}\int_{S_D} \mathbf{B}(\mathbf{x},\eta)\cdot\begin{bmatrix} T_{nr}^D \\ T_{nz}^D \end{bmatrix} dl_D - \frac{1}{8\pi}\int_{S_I} \mathbf{B}(\mathbf{x},\eta)\cdot\begin{bmatrix} T_{nr}^I \\ T_{nz}^I \end{bmatrix} dl_I$$

$$+ \frac{3}{4\pi}\int_{S_D} \mathbf{C}(\mathbf{x},\eta)\cdot\begin{bmatrix} u_r^D \\ u_z^D \end{bmatrix} dl_D + \frac{3}{4\pi}\int_{S_I} \mathbf{C}(\mathbf{x},\eta)\cdot\begin{bmatrix} u_r^I \\ u_z^I \end{bmatrix} dl_I \qquad (31)$$

$$\frac{1}{2}\begin{bmatrix} u_r^I(\mathbf{x}) \\ u_z^I(\mathbf{x}) \end{bmatrix} = -\frac{1}{8\pi}\int_{S_D} \mathbf{B}(\mathbf{x},\eta)\cdot\begin{bmatrix} T_{nr}^D \\ T_{nz}^D \end{bmatrix} dl_D - \frac{1}{8\pi}\int_{S_I} \mathbf{B}(\mathbf{x},\eta)\cdot\begin{bmatrix} T_{nr}^I \\ T_{nz}^I \end{bmatrix} dl_I$$

$$+ \frac{3}{4\pi}\int_{S_D} \mathbf{C}(\mathbf{x},\eta)\cdot\begin{bmatrix} u_r^D \\ u_z^D \end{bmatrix} dl_D + \frac{3}{4\pi}\int_{S_I} \mathbf{C}(\mathbf{x},\eta)\cdot\begin{bmatrix} u_r^I \\ u_z^I \end{bmatrix} dl_I \qquad (32)$$

$$\frac{1}{2}(\lambda_1 + 1)\begin{bmatrix} u_r^D(\mathbf{x}) \\ u_z^D(\mathbf{x}) \end{bmatrix} = -\frac{1}{8\pi}\int_{S_D} \mathbf{B}(\mathbf{x},\eta)\cdot\begin{bmatrix} Q_r^D(f) \\ Q_z^D(f) \end{bmatrix} dl_D - \frac{1}{8\pi}\int_{S_I} \mathbf{B}(\mathbf{x},\eta)\cdot\begin{bmatrix} T_{nr}^I \\ T_{nz}^I \end{bmatrix} dl_I$$

$$+ \frac{3}{4\pi}(1 - \lambda_1)\int_{S_D} \mathbf{C}(\mathbf{x},\eta)\cdot\begin{bmatrix} u_r^D \\ u_z^D \end{bmatrix} dl_D + \frac{3}{4\pi}\int_{S_I} \mathbf{C}(\mathbf{x},\eta)\cdot\begin{bmatrix} u_r^I \\ u_z^I \end{bmatrix} dl_I \qquad (33)$$

$$\frac{1}{2}(\lambda_3 + 1)\begin{bmatrix} u_r^I(\mathbf{x}) \\ u_z^I(\mathbf{x}) \end{bmatrix} = -\frac{1}{8\pi}\int_{S_D} \mathbf{B}(\mathbf{x},\eta)\cdot\begin{bmatrix} T_{nr}^D \\ T_{nz}^D \end{bmatrix} dl_D - \frac{1}{8\pi}\int_{S_I} \mathbf{B}(\mathbf{x},\eta)\cdot\begin{bmatrix} Q_r^I(h) \\ Q_z^I(h) \end{bmatrix} dl_I$$

$$+ \frac{3}{4\pi}\int_{S_D} \mathbf{C}(\mathbf{x},\eta)\cdot\begin{bmatrix} u_r^D \\ u_z^D \end{bmatrix} dl_D + \frac{3}{4\pi}(1 - \lambda_3)\int_{S_I} \mathbf{C}(\mathbf{x},\eta)\cdot\begin{bmatrix} u_r^I \\ u_z^I \end{bmatrix} dl_I \qquad (34)$$

where

$$dl_D = f\sin\theta\left[f^2 + \left(\frac{\partial f}{\partial\theta}\right)^2\right]^{1/2} d\theta$$

and

$$dl_I = r\left[1 + \left(\frac{\partial h}{\partial r}\right)^2\right]^{1/2} dr$$

The quantities **B** and **C** are tensors whose elements consist of elliptic integrals

$$\mathbf{B}(\mathbf{x},\boldsymbol{\eta}) = \begin{bmatrix} B_{rr} & B_{rz} \\ B_{zr} & B_{zz} \end{bmatrix} \quad \mathbf{C}(\mathbf{x},\boldsymbol{\eta}) = \begin{bmatrix} C_{rr} & C_{rz} \\ C_{zr} & C_{zz} \end{bmatrix}. \tag{35}$$

The elements of **B** and **C** are given by Lee and Leal (1982).

There are eight linear integral Eqs. (31)-(34) for eight unknown functions u_r^D, u_r^I, u_r^I, u_z^I, T_{nr}^D, T_{nz}^D, T_{nr}^I and T_{nz}^I. As in the works of Lee and Leal (1982) and Geller, Lee and Leal (1985), a collocation method was used to approximate the linear integral equations by a system of linear algebraic equations. To apply the collocation technique, the drop surface and the interface were divided into small elements so that $\mathbf{u}^D$, $\mathbf{u}^I$, $\mathbf{T}^D$, $\mathbf{T}^I$ could be approximated as constants within each element by the values at the center of the element. Then, we obtain a system of $(4N_D + 4N_I)$ linear algebraic equations where N_D and N_I are the numbers of elements on the drop surface and the interface, respectively. The integrals in Eqs. (25)-(28) were evaluated by Gauss quadrature, and the system of linear equations was solved by Gaussian elimination. When $\mathbf{x} = \boldsymbol{\eta}$, the integrals in (16), (17), (19) and (21) become singular. However, finite values for the integrals were obtained by analytical integration over a small neighborhood of $\mathbf{x}$ using a linear expansion of the integrands.

III. Results

Numerical calculations are carried out for the case when fluid 1 is the same as fluid 3. For this case, $Ca_1 = Ca_3 = Ca$, $\lambda_1 = \lambda_3 = \lambda$, and $Cg_3 = Cg_1 = 2/9\beta$. This is the system occurring most frequently in industrial processes (e.g. liquid-liquid extraction). When fluid 1 is the same as fluid 3, Geller, Lee, and Leal (1985) have

shown by using a macroscopic force balance for a sphere approaching an interface, that coalscence must occur via some type of film drainage mechanism (because the density of fluid 1 is the same as the density of fluid 3), though this is not true in general.

The initial configuration considered in the present calculation was always a spherical drop and a flat interface. For non-zero Ca's, the drop shape is spherical only when the drop is far away from the interface, i.e. rising in an unbounded fluid. As the drop approaches the interface, the drop deforms due to the hydrodynamic interactions with the interface. Therefore, an idealized initial condition would be to start the numerical calculation with a spherical drop located very far from a flat interface. But starting the calculation with the drop too far from the interface is clearly not practical. Therefore, we start with the drop at a finite distance from the interface, after first evaluating the effect of the initial position of the drop via numerical calculations. In Figs. 2 and 3, drop shapes and interface shapes are shown for three different initial positions of the drop ($L_{t=0}$ = 1.2, 3 and 7) with Ca = 2.0, λ = 0.5 and Ca = 2.0, λ = 10.0, respectively. It can be seen that at L = 0.01, the drop and interface shapes become identical for the two initial positions, $L_{t=0}$ = 3 and 7. But for $L_{t=0}$ = 1.2, the drop and interface shapes differ significantly from the shape for $L_{t=0}$ = 3 and 7. Physically, the drop "rests" very near the interface until a rupture occurs due to instability. Since there is very little motion of the drop and the interface in this "rest" state, no matter where the calculation was started, the drop and interface shapes should converge to one shape very near the interface. Thus, the shapes with $L_{t=0}$ = 1.2 should eventually become the same as the shapes obtained with $L_{t=0}$ = 3 and 7 if the calculation is continued until the film becomes extremely thin. In the current calculation, as the film between the drop and the upper bulk fluid becomes thin the time step must become smaller, and the

computation is terminated when the cost of further calculation is unacceptably large. In the following sections, the calculations are started at $L_{t=0} = 3$ to observe the evolution of the shapes as the drop approaches the interface. In Fig. 4, the velocity of the center of mass of the drop is plotted against L for the three different initial positions ($L_{t=0} = 3, 5, 7$) and Ca = 2.0, $\lambda = 0.5$. As can be seen in the figure the velocities becomes identical beyond $L \sim 0.7$. This again confirms the fact that starting at $L_{t=0} = 3$ will simulate the approach of an initially spherical drop toward an initially flat interface from far away from the interface.

A. Preliminary Calculations

When the collocation method is applied to the integral Eqs. (25)-(28), the domain of the interface must be truncated at some large, but finite distance from the central symmetry line. It was shown by Lee and Leal (1982) that the integrals decay like $1/\rho_2$ for large r for the case of a solid sphere approaching an interface. In Fig. 5, $\mathbf{u}^I \cdot \mathbf{n}_3$ on the interface is plotted as a function of r for Ca = 2.0 and $\lambda = 0.5$ when the domain of the interface is truncated at r = 13. It can be seen that $\mathbf{u}^I \cdot \mathbf{n}_3$ becomes almost zero beyond $r \sim 10$. Thus, it appears to be reasonably accurate to truncate the interface around r = 10. In the calculations reported later, the interface was usually truncated at r = 13.

In this numerical study, the drop surface and interface were discretized into small elements in which $\mathbf{u}^D$, $\mathbf{T}^D$, $\mathbf{u}^I$, $\mathbf{T}^I$ are constant. Non-uniform elements were used on the drop. For the initially spherical drop, uniform elements were used and as the drop approaches close to the interface, more elements were given to the region where $\mathbf{u}^D$, $\mathbf{T}^D$ varied rapidly. Usually 20 elements were used for a spherical drop, and up to 30 elements were used as the drop deforms. On the interface, the region close to the drop is descretized with smaller elements and

as the distance between the interface and the drop increases, the element size becomes increasingly large.

The drop shape and interface shape were changed using the kinematic conditions (9) and (12) that

$$h_{j+1} = h_j + [\mathbf{u}_j^I \cdot \mathbf{n}_{3j}]\Delta t \, \frac{1}{K_{Ij}} \quad \text{for the interface} \tag{23}$$

$$f_{j+1} = f_j + \left[\left(\mathbf{u}_j^D + \frac{L_{j+1} - L_j}{\Delta t}\,\mathbf{i}_z\right)\cdot \mathbf{n}_{1j}\right]\Delta t \, \frac{1}{K_{Dj}} \quad \text{for the drop} \tag{24}$$

as explained earlier. Typically, Δt varied from 0.02 to 0.06. For the initial spherical drop 3 radii away from the interface, Δt of 0.06 was used. As the drop approaches close to the interface, shorter time steps were used because the rate of deformation of the drop and interface increased. When a shorter time step was introduced, calculations are done again using the shorter time step for the overlap region with the old larger time step. If the difference in the shapes was greater than 2%, then the overlap region was increased until the difference was 2%.

B. Comparison with Previous Results

Calculations were carried out for two cases to compare present theoretical results with the previous published experimental results of Hartland (1967b,1969). In figure 6, the shapes of the drop and interface for the two cases when Ca = 0.5, λ = 5.0 and Ca = 1.0, λ = 0.02 are compared with the experimental pictures of Hartland. In these experimental investigations, the drop was formed at the tip of a needle almost touching the interface. So the drop was already deformed during the formation at the tip prior to the release from the needle. However, current calculations are started with a spherical drop 3 radii away from a flat interface. Therefore, a quantitative comparison of the results

would not be expected to add much to our understanding. However, our present results agree well, on qualitative basis, with the Hartland's results. Particularly, in Fig. 6b, the film drains uniformly, while in Fig. 6a, a "dimple" occurs so that the film is thinnest in the region away from central symmetry axis. Different drainage mechanisms will be discussed more in detail below.

An attempt to compare current result with film drainage theory is illustrated in Fig. 7 where the present numerical solution is for Ca = 0.05, λ = 30 and the film drainage result is for Ca = 0.019, λ = 32.8. The film drainage solution was taken from the work of Lin and Slattery (1984) where the initial shape was taken as a dimpled shape for calculation. In the film drainage theory, the typical film thickness is $O(10^{-3})$ whereas our computations are terminated when the thickness is ~ 0.05. Therefore, the comparison cannot be of quantitative nature. Only qualitative agreement is shown in Fig. 7.

C. Numerical Results

Calculations were carried out for cases when λ = 0.1, 1, 10 and Ca = 0.2, 1, 10. In the present calculations, the evolution of the overall drop shape and the interface shape as the drop approaches the interface was observed by starting the calculations with the initial position of the drop three radii away from the interface. The motion inside the drop and in the upper fluid was included in the calculations. Therefore, the effects of the physical properties, namely viscosity ratios, of the drop fluid and the upper bulk fluid, which are not included in the film drainage theory, are studied. Resulting shapes as the drop approaches the interface are shown in Figs. 8, 9 and 10. The film thickness at the symmetry line, H_{cen}, and the minimum film thickness, H_{min}, are plotted against time, t, in Fig. 11. In Fig. 12, drop velocities are plotted against L as the drop approaches the interface.

1. Shapes and Film Profiles

In the following part of this section, the effects of λ and Ca on the shapes of the drop and the interface as the drop approaches the interface are discussed. In Figs. 9 and 10, the drop and interface shapes are drawn for three distances, L, relative to the interface, L = 1.0, 0.5, 0.01 when Ca = 1.0 and 10.0. In Fig. 8, when Ca = 0.2, the dotted lines represent L = 0.36, 0.29, 0.28 for λ = 0.1, 1, 10, respectively, because L = 0.01 cannot be reached by the drop in this case.

Effect of λ

When Ca = 0.2, as λ increases, the drop shape becomes slightly more flattened and the interface becomes more deformed as the drop approaches the interface. In additon, for λ = 0.1, the film between the drop and the interface is thinnest at r = 0.0, and the film thickness increases as r increases. This type of film profile is associated with "rapid drainage" and occurs for systems with low λ for which the drop approaches toward the interface faster than for high λ systems. For λ = 1.0, the variation of the film thickness with r is so slight that the film appears to have almost uniform thickness up to r = 0.7, i.e. between $0 \leq r \leq 0.7$, and the film drains almost uniformly as the drop moves closer to the interface. However, for λ = 10.0, dimpled drainage occurs for which the film is thinnest at the rim radius r = 0.66, rather than the center r = 0. This is also shown in Fig. 9 where the dotted line for H_{min} diverges from the solid line for H_{cen} at t = 6.12. When the minimum thickness occurred at the rim, Charles and Mason (1960), Hodgen and Wood (1969), and Burrill and Wood (1973) observed that rupture occurred off-center as an apparent physico-chemical instability set in. However, current calculations are terminated before we can observe the instability, although the spatial resolution of our solution algorithm is such that disturbances on the scale of the minimum film thickness could be decreased if

they were present. All three types of drainage were observed in the experiments by Hodgen and Wood (1969) and Burrill and Wood (1973) for the systems with surfactants. They attributed the different mechanisms to the effect of surfactants. However, present results show that these different types of drainage, namely rapid drainage, uniform drainage, and dimpled drainage, can also occur as the result of different viscosity ratios between the upper phase (also drop fluid) and the lower phase fluids, at least for Ca = 0.2.

Let us now consider the effect of the viscosity ratio for larger values of Ca. In particular, when Ca = 1.0, the results in Fig. 7 show that the drop shape is more flattened as λ increases. Further, for any given λ, the interface is more deformed compared to Ca = 0.2, because the interfacial force is reduced relative to viscous forces all else being equal. The film thickness shows the same trend as λ varies as was seen for Ca = 0.2.

Finally,when Ca = 10.0, the drop becomes flatter and flatter at the rear for λ =0.1 and 1.0, until eventually an indentation appears at the rear stagnation point of the drop. The indentation is more significant for λ = 0.1 than λ = 1.0. For λ = 10.0, the drop retains fore-aft symmetry to a good degree of approximation. However, as λ varies, and same trend in film thickness is seen as for Ca = 0.2 and Ca = 1.0. By considering the motion inside the drop and in the upper bulk fluid, the current calculations identified the three distinct mechanisms of film drainage which are rapid drainage, uniform drainage and dimpled drainage. These distinct drainage mechanisms arise as a result of the variation of the viscosity ratio between the drop (and the upper bulk) fluid and the lower bulk fluid. In the film drainage theories, the motion inside the drop and in the upper bulk fluid is not considered. Instead, either no-slip (immobile interface) or zero tangential stress (mobile interface) is used as boundary conditions to solve the motion in the thin film region between the drop and the interface. Therefore,

the thin film theories are not able to predict the different drainage mechanisms described above.

Effect of Ca

We can also use the same results to deduce the effect of variations in Ca for fixed λ. When $\lambda = 0.1$, as Ca increases, the drop shape changes from spherical to oblate spheroidal in shape. The rear of the drop becomes flatter and flatter and for Ca = 10.0, the indentation appears at the rear, while the front of the drop remains as a spherical cap. As Ca increases the deformation of the interface also becomes broader because a larger region of the interface is affected by the presence of the drop as the drop becomes flatter. As mentioned previously rapid drainage occurs for all Ca when $\lambda = 0.1$.

The same trends can be seen for $\lambda = 1.0$. However, in this case, the rigion of uniform film thickness appears and persists thereafter during further approach of the drop. Therefore, uniform drainage occurs for all Ca.

Finally, for $\lambda = 10.0$, as the drop becomes flatter, fore-aft symmetry is maintained and no indentation forms at the rear of the drop. The difference in the film thickness between the centerline and the rim increases as Ca increases. This can be seen in Fig. 9 where dotted curve diverges from the solid curve further for $\lambda = 10.0$. This is caused by the fact that the drop flattens out more for high λ sysyems due to the resistance of the more viscous upper bulk fluid. In this case, then so-called "dimple" drainage occurs for all Ca.

2. Velocity of Drop

The dimensionless velocity of the center of mass of the drop as it approaches the interface is plotted against L in Fig. 12. The velocity obtained for a solid sphere approaching a solid wall, obtained by letting $\lambda = 100$ in the current calculation, is also plotted in Fig. 12. The velocity of the solid sphere approaching a

solid wall coincides with the analytical result of Brenner (1961). For all λ's and Ca's considered, the velocity of the drop approaches zero abruptly as the drop approaches the interface, indicating that the drop seems to reach the "rest" state very close to the interface.

As can be seen in Fig. 12, more viscous drops move slower that less viscous drops. However, it should be noted that the drop velocity shown here is nondimensionalized with the characteristic velocity

$$u_c = U_\infty = \frac{2}{9} \frac{ga^2(\rho_2 - \rho_1)}{\mu_2} \frac{1}{\beta}$$

where $\beta = \dfrac{1 + \dfrac{2}{3\lambda}}{1 + \dfrac{1}{\lambda}}$.

Since $1/\beta$ = 1.4347, 1.2000, 1.0312 for λ = 0.1, 1.0, 10.0, respectively, it is evident that if all parameters except the viscosity of the drop are same, the dimensional velocity of the more viscous drop will be relatively smaller than the velocity that appears in Fig. 12.

As Ca increases, the interface and the drop becomes less resistant to deformation due to the increase of the viscous force relative to the interfacial force. Though the drop becomes more flattened as Ca increases, the velocity of the drop increases as Ca increases for all viscosity ratios.

As the drop approaches the interface, the drop slows down due to the hydrodynamic interactions with the interface. In Fig. 12, it is illustrated that the velocity of the drop with smaller Ca is always less that that with larger Ca for fixed λ. Up to L ~ 1.5, the velocity decreases at almost the same rate for all Ca as L decreases, i.e. as the drop approaches the interface. Beyond L of 1.5, the velocity of the drop with smaller Ca, particularly Ca = 0.2 decreases more rapidly

than the drop with larger Ca. Though the drop shape becomes flatter for larger Ca, the hydrodynamic resistance of the interface has more domimant effect on the velocity of the drop. Therefore, the drop with smaller Ca slows down more because the interfacial tension tends to maintain the interface in its initial flat configuration. For Ca = 0.2, the drop velocity becomes almost zero, i.e. the drop reaches the "rest" state, at L = 0.36, 0.29, 0.28 for λ = 0.1, 1.0, 10.0, respectively. For Ca = 10.0, the velocity decreases almost at the same rate as Ca = 1.0. while the drop with Ca=10.0 always moves faster than that with Ca = 1.0.

IV. Conclusions

Numerical study of the axisymmetric approach of a deformable drop toward a deformable interface under the action of a constant buoyancy force has been carried out. In the present study, the initial configuration has a drop located some distance (usually three radii) away from an undeformd flat interface so that the evolution of the overall drop shape and the interface shape as the drop approaches the interface was observed.

The motion inside the drop and in the upper bulk fluid was included in the calculations. Therefore, the effect of the physical properties, namely viscosity ratios, of the drop fluid and the upper bulk fluid, which are not included in the film drainage theory, are studied. In the film drainage theories, instead of solving the motion inside the drop and in the upper bulk fluid, either no-slip (immobile interface) or zero tangential stress (mobile interface) are used as boundary conditions on the drop surface and the interface. We have shown that three distinct mechanisms of film drainage arise as a result of the variation of the viscosity ratios between the drop (and the upper bulk) fluid and the lower bulk fluid. For λ = 0.1, rapid drainage occurs, and uniform drainage occurs for λ = 1.0. Dimple drainage for which minimum film thickness appears at a rim occurs for

λ = 10.0. These drainage patterns were observed experimentally by Hodgen and Wood (1969) and Burrill and Wood (1973) by varying the concentration of the surfactants. However, the current study illustrates, for pure interfaces, that these different patterns can arise as the viscosity ratio varies.

The drop becomes flatter as Ca increases. For λ = 0.1 and 1.0, indentation appears at the rear of the drop when Ca = 10.0, and this indentation is more pronounced for λ = 0.1 than λ = 1.0. As the drop approaches the interface, the velocity of the drop decreases more rapidly for smaller Ca because the interfacial tension tends to maintain the interface in its initial flat configuration.

As the film between the drop and the interface becomes very thin, the time step must become smaller in the present calculations, and the calculations were terminated when the cost for further calculation became unacceptably large. Consequently, the film drainage of a very thin film was not studied. The drainage of very thin film between the drop and the interface can be solved by film drainage models which employ lubrication approximation in the thin film region. In order to use the film drainage models, initial shapes of the drop and the interface must be proovided. The final shapes of the drop and the interface of the current calculation can be used as initial shapes of the film drainage models in the very thin film region.

As mentioned previously, the motion inside the drop and in the upper fluid is not considered in the film drainage models. Since our calculation was terminated before the film became very thin where the thin film theories can apply, it is not possible to estimate the effect of considering the motion inside the drop and in the upper fluid for the very thin film.

Appendix

In dimensional form, Eq. (11) is

$$\mathbf{n}_1\cdot\mathbf{T}_2 - \mathbf{n}_1\cdot\mathbf{T}_1 = \gamma_{12}\nabla\cdot\mathbf{n}_1\mathbf{I}\cdot\mathbf{n}_1 - (\rho_2-\rho_1)g z\mathbf{I}\cdot\mathbf{n}_1 \,. \tag{A1}$$

Rearranging Eq. (A1), we obtain

$$\mathbf{n}_1\cdot\mathbf{T}_2 = \mathbf{n}_1\cdot\mathbf{T}_1 + \gamma_{12}\nabla\cdot\mathbf{n}_1\mathbf{n}_1 - (\rho_2-\rho_1)g z\mathbf{I}\cdot\mathbf{n}_1 \,. \tag{A2}$$

Then, the drag force on the drop is

$$\mathbf{F}_D = \int \mathbf{n}_1\cdot\mathbf{T}_2 dS_D = \int \mathbf{n}\cdot\mathbf{T}_1 dS_D + \int \gamma_{12}\nabla\cdot\mathbf{n}_1\mathbf{n}_1 dS_D - \int(\rho_2-\rho_1)g z\mathbf{I}\cdot\mathbf{n}_1 dS_D \tag{A3}$$

Applying the divergence theorem to the first term of the RHS of Eq. (A3), it can be shown that

$$\int \mathbf{n}_1\cdot\mathbf{T}_1 dS_D = \int \nabla\cdot\mathbf{T}_1 dV_D = 0 \tag{A4}$$

because

$$\nabla\cdot\mathbf{T}_1 = 0$$

for Stokes equations.

Now, consider the second term in the RHS of Eq. (A3). Surface divergence theorem states that for any scalar function φ on a surface S

$$\int \varphi(\nabla\cdot\mathbf{n})\mathbf{n} dS_D = \int \nabla\varphi dS - \int_c \varphi\mathbf{t} dl \tag{A5}$$

where c denotes any closed curve on the surface S, and $\mathbf{t}$ denotes the unit vector that is normal to the curve c and tangent to the surface at each point. Then, by applying the surface divergence theorem, the second term of the RHS of Eq. (A3) becomes

$$\int \gamma_{12}(\nabla \cdot \mathbf{n}_1)\mathbf{n}_1 dS_D = \int \nabla \gamma_{12} dS_D - \int_c \gamma \mathbf{t} dl \tag{A6}$$

The first term of the RHS of Eq. (A6) is zero because $\nabla \gamma = 0$ for constant γ. And the second term of the RHS of Eq. (A6) is zero because

$$\int_c \gamma \mathbf{t} dl = 0$$

for a closed volume. Finally, applying the divergence theorem to the third term in the RHS of Eq. (A3)

$$-\int (\rho_2 - \rho_1) g z \mathbf{I} \cdot \mathbf{n}_1 dS_D = -(\rho_2 - \rho_1) g \int \nabla \cdot z \mathbf{I} dV_D \tag{A7}$$

The RHS of Eq. (A7) is then

$$-(\rho_2 - \rho_1) g \mathbf{i}_z \int dV_D = -(\rho_2 - \rho_1) g \mathbf{i}_z \frac{4}{3} \pi a^3 \tag{A8}$$

where a is the undeformed drop radius. Then, the third term of the RHS of Eq. (A3) represents buoyancy force. Therefore, the above result confirms the fact that the stress conditions in Eq. (11) satisfy the force balance on the drop.

References

Allan, R. S., Charles, G. E. and Mason, S. G. 1961 The approach of gas bubbles to a gas/liquid interface. J. Coll. Int. Sci. **16**, 150.

Brenner, H. 1961 The slow motion of a sphere through a viscous fluid toward a plane surface. Chem. Eng. Sci. **16**, 242.

Burrill, K. A. and Woods, D. R. 1969 Change in interface and film shapes for a deformable drop at a deformable liquid-liquid interface. J. Coll. Int. Sci. **30**, 511.

Burrill, K. A. and Woods, D. R. 1973 Film shapes for deformable drops at liquid-liquid interfaces. II. The mechanism of film drainage. J. Coll. Int. Sci. **42**, 15.

Charles, G. E. and Mason, S. G. 1960 The coalescence of liquid drops with flat liquid-liquid interfaces. J. Coll. Int. Sci. **15**, 236.

Chen, J. D., Hahn, P. S. and Slattery, J. C. 1984 Coalescence time for a small drop or bubble at a fluid-fluid interface. A.I.Ch.E. J. **30**, 622.

Chervenivanova, E. and Zapryanov, Z. 1985 The slow motion of one or two droplets towards a deformable flat fluid interface. J. Fluid Mech. (submitted).

Frankel, S. P. and Mysels, K. J. 1962 On the 'dimpling' during the approach of two interfaces. J. Phys. Chem. **66**, 190.

Geller, A. W., Lee, S. H. and Leal, L. G. 1985 The creeping motion of a spherical particle to a deformable interface. J. Fluid Mech. (accepted).

Hartland, S. 1967 The coalescence of a liquid drop at a liquid-liquid interface. Part I. Drop Shape. Trans. Inst. Chem. Engrs. **45**, T97.

Hartland, S. 1967 The coalescence of a liquid drop at a liquid-liquid interface. Part II. Film thickness. Trans. Inst. Chem. Engrs. **45**, T102.

Hartland, S. 1967 The coalescence of a liquid drop at a liquid-liquid interface. Part III. Film rupture. Trans. Inst. Chem. Engrs. **45**, T109.

Hartland, S. 1967 The coalescence of a liquid drop at a liquid-liquid interface. Part V. The effect of surface active agents. Trans. Inst. Chem. Engrs. **45**, T275.

Hartland, S. 1969 The effect of circulation pattersons on the drainage of the film between a liquid drop and a deformable liquid-liquid interface. Chem. Eng. Sci. **24**, 611.

Hartland, S. 1970 The profile of the draining film between a fluid drop and a deformable fluid-liquid interface. Chem. Eng. J. **1**, 67.

Hodgson, T. D. and Woods, D. R. 1969 The effect of surfactants on the coalescence of a drop at an interface. II. J. Coll. Int. Sci. **30**, 429.

Jones, A. F. and Wilson, S. D. R. 1978 The film drainage problems in drop coalescence. J. Fluid Mech. **87**, 263.

Lee, S. H. and Leal, L. G. 1982 Motion of a sphere in the presence of a deformable interface. Part 2: Numerical study of the translation of a sphere normal to an interface. J. Coll. Int. Sci. **87**, 81.

Lin, C. Y. and Slattery, J. C. 1982 Thinning of a liquid film as a small drop or bubble approaches a fluid-fluid interface. A.I.Ch.E. J. **28**, 786.

MacKay, G. D. M. and Mason, S. G. 1963 The gravity approach and coalescence of fluid drops at liquid interfaces. Can. J. Chem. Eng. **203**.

Princen, H. M. 1963 Shape of a fluid drop at a liquid-liquid interface. J. Coll. Int. Sci. **18**, 178.

Princen, H. M. and Mason, S. G. 1963 Shape of a fluid drop at a fluid-fluid interface. I. Extension and test of two-phase theory. J. Coll. Int. Sci. **29**, 156.

Woods, D. R. and Burrill, K. A. 1972 The stability of emulsions. J. Electroanal. Chem. **37**, 191.

Figure Captions

Figure 1: Description of the coordinate systems. O_L, origin of the local coordinate systems; O_G, origin of the global coordinate systems.

Figure 2: Shapes of the drop and the interface for Ca = 2.0, λ = 0.5; —· · —$L_{t=0}$ = 1.2; —$L_{t=0}$ = 3; ——· · ——$L_{t=0}$ = 7.

Figure 3: Shapes of the drop and the interface for Ca = 2.0, λ = 10.0; —· · — $L_{t=0}$ = 1.2; —$L_{t=0}$ = 3; ——· · ——$L_{t=0}$ = 7.

Figure 4: Dimensionless velocity of the center of mass of the drop dL/dt as a function of the dimensionless distance of the center of mass of the drop from the undeformed flat interface L for Ca = 2.0, λ = 0.5; —$L_{t=0}$ = 3; ———$L_{t=0}$ = 5; ----- $L_{t=0}$ = 7.

Figure 5: Dimensionless normal velocity on the interface $\mathbf{u}^I \cdot \mathbf{n}_3$, as a function of the dimensionless radial distance, r. —— Ca = 10, λ = 0.1; ----- Ca = 10, λ, = 10.0.

Figure 6: Comparison of the calculated drop shapes and the interface with the experimental photographs. —— Ca = 1.0, ----- L = 0.5, —-- —L = 0.1.

Figure 7: Comparison of the calculated drop shapes and the interface with the results of the film drainage theory for the drop with undeformed drop radius of 6.2 x 10^{-2} cm obtained by Lin and Slattery (1982).

Figure 8: Shapes of the drop and the interface for Ca = 2.0, λ = 0.1, 1.0, 10.0; ——L = 1.0; ———L = 0.5; ---- L = 0.36, 0.29, 0.28 for λ = 0.1, 1.0, 10.0, respectively.

Figure 9: Shapes of the drop and the interface for Ca = 1, λ = 0.1, 1.0, 10.0; —— L = 1.0; ———L = 0.5; ---- L = 0.01.

Figure 10: Shapes of the drop and the interface for Ca = 10, λ = 0.1, 1.0, 10.0; ——L = 1.0; — — —L = 0.5; ---- L = 0.01.

Figure 11: Dimensionless film thickness at the centerline, H_{cen}, and at the rim, H_{min}, as a function of the dimensionless time.

Figure 12: Dimensionless velocity of the center of mass of the drop |dL/dt| as a function of the dimensionless distance of the center of mass of the drop from the undeformed flat interface L. ——Ca = 0.2; — — —Ca = 1.0; ---- Ca = 10.0.

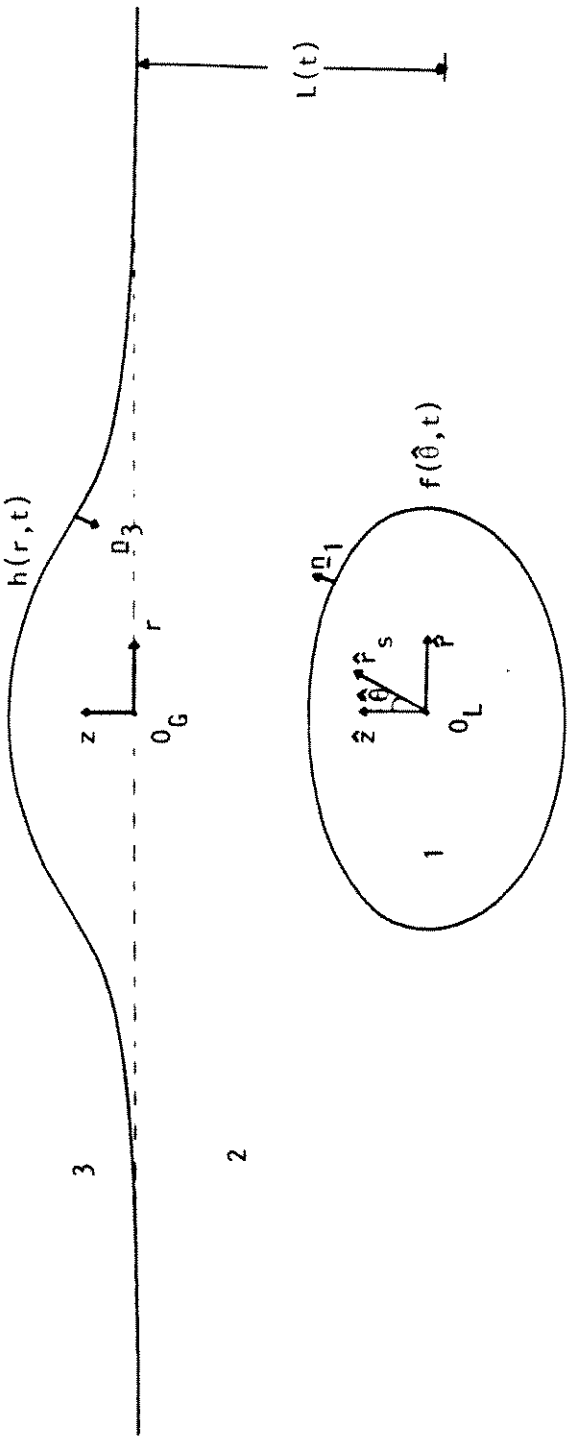

Figure 1

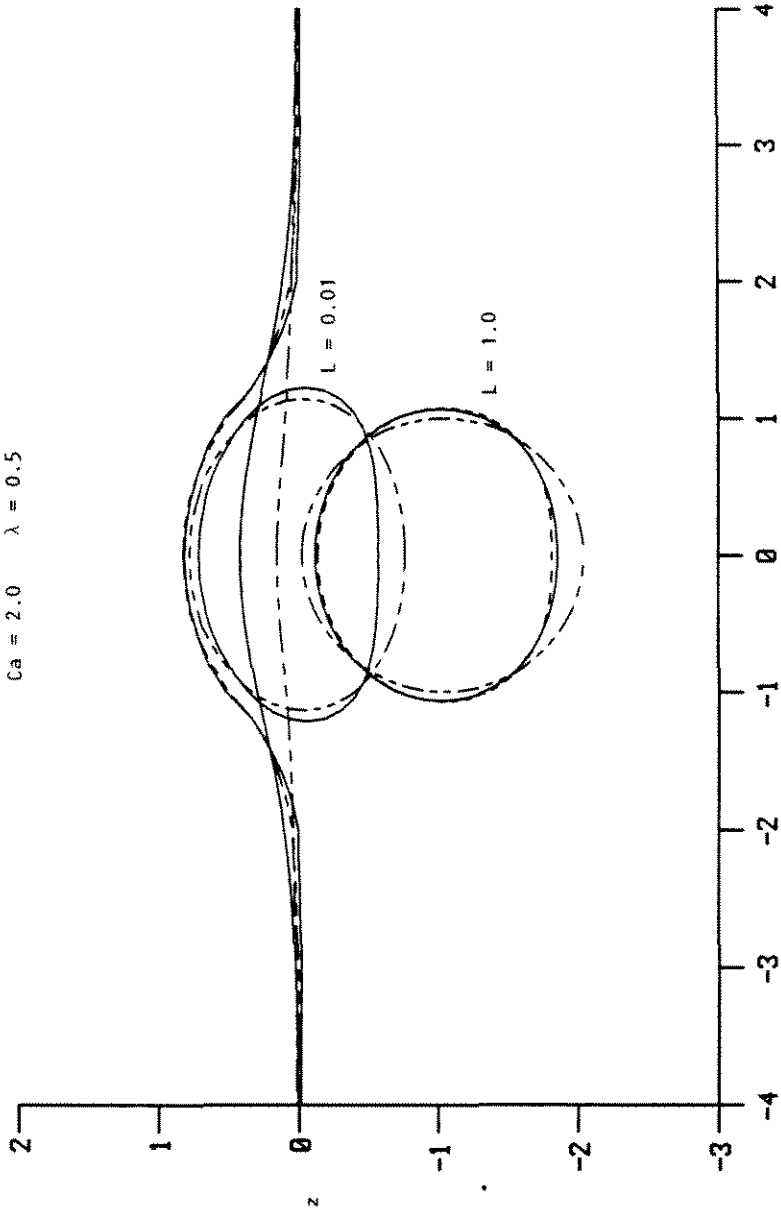

Figure 2

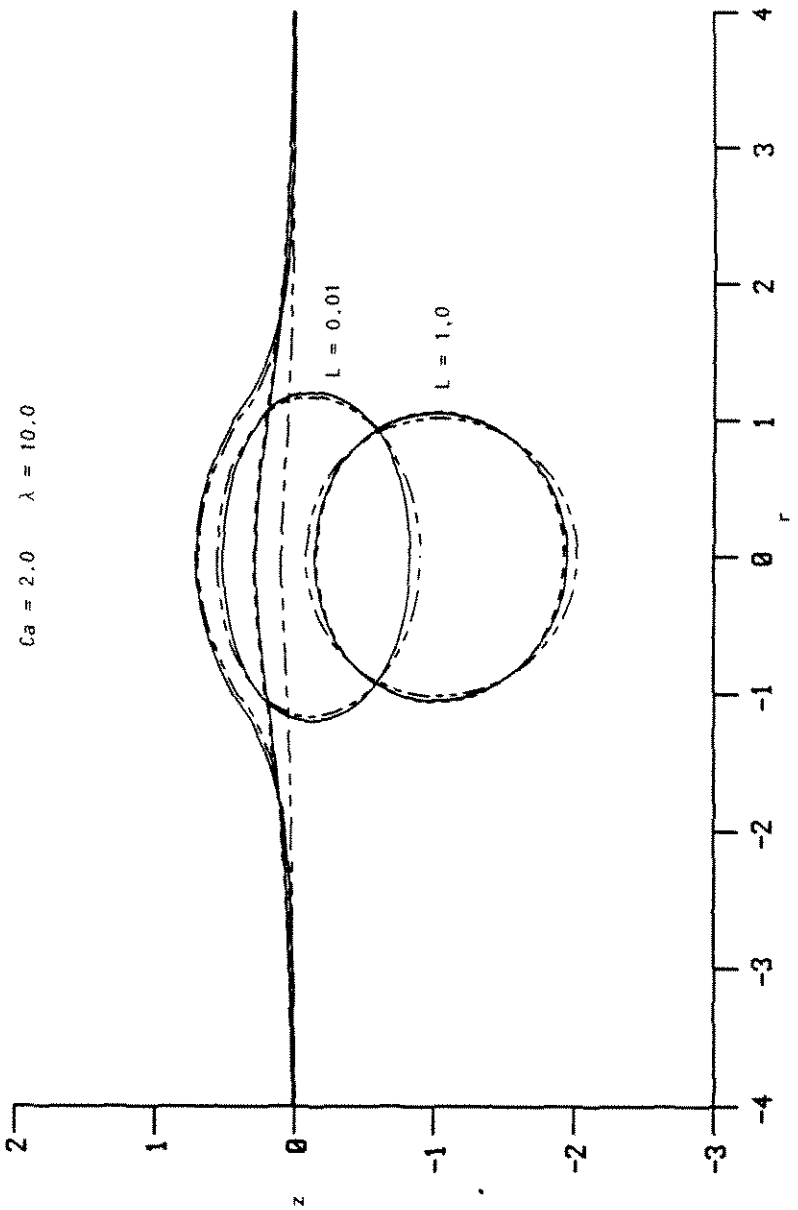

Figure 3

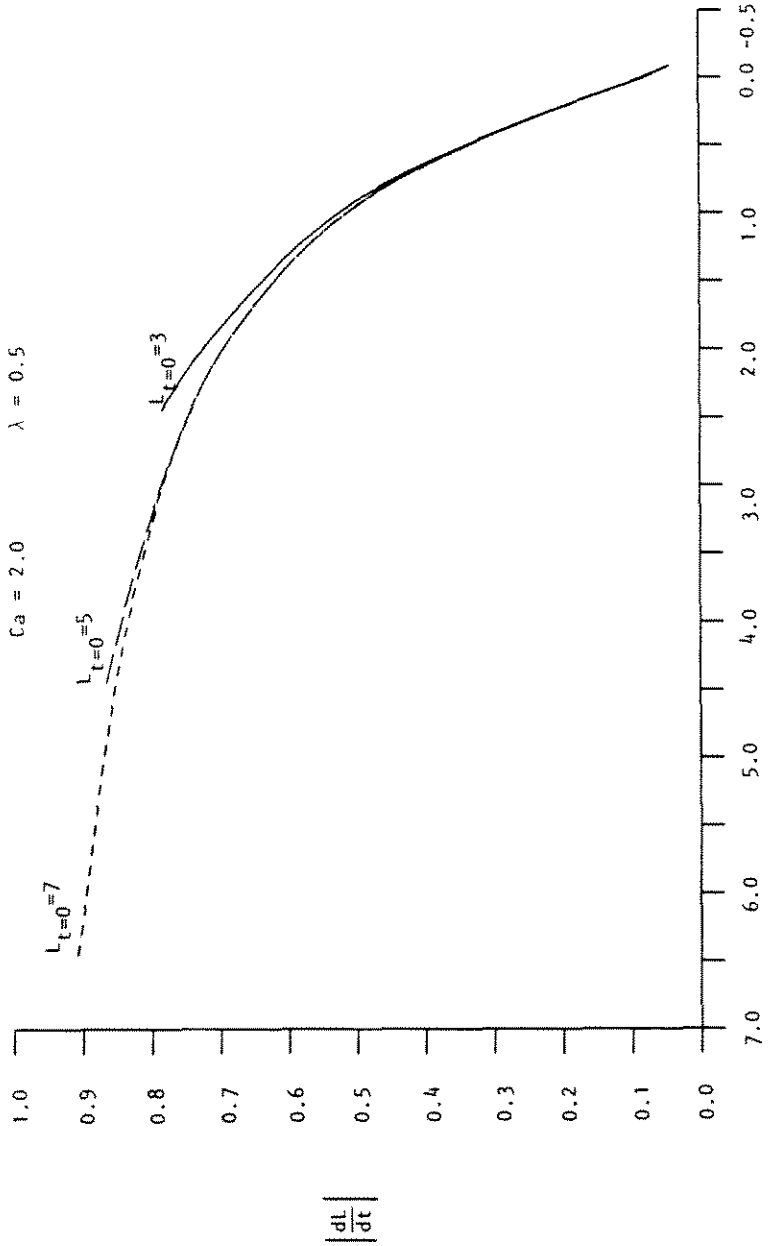
Ca = 2.0
λ = 0.5
$L_{t=0}=7$
$L_{t=0}=5$
$L_{t=0}=3$
$\left|\frac{dL}{dt}\right|$
1.0
0.9
0.8
0.7
0.6
0.5
0.4
0.3
0.2
0.1
0.0
7.0
6.0
5.0
4.0
3.0
2.0
1.0
0.0 -0.5
L

Figure 4

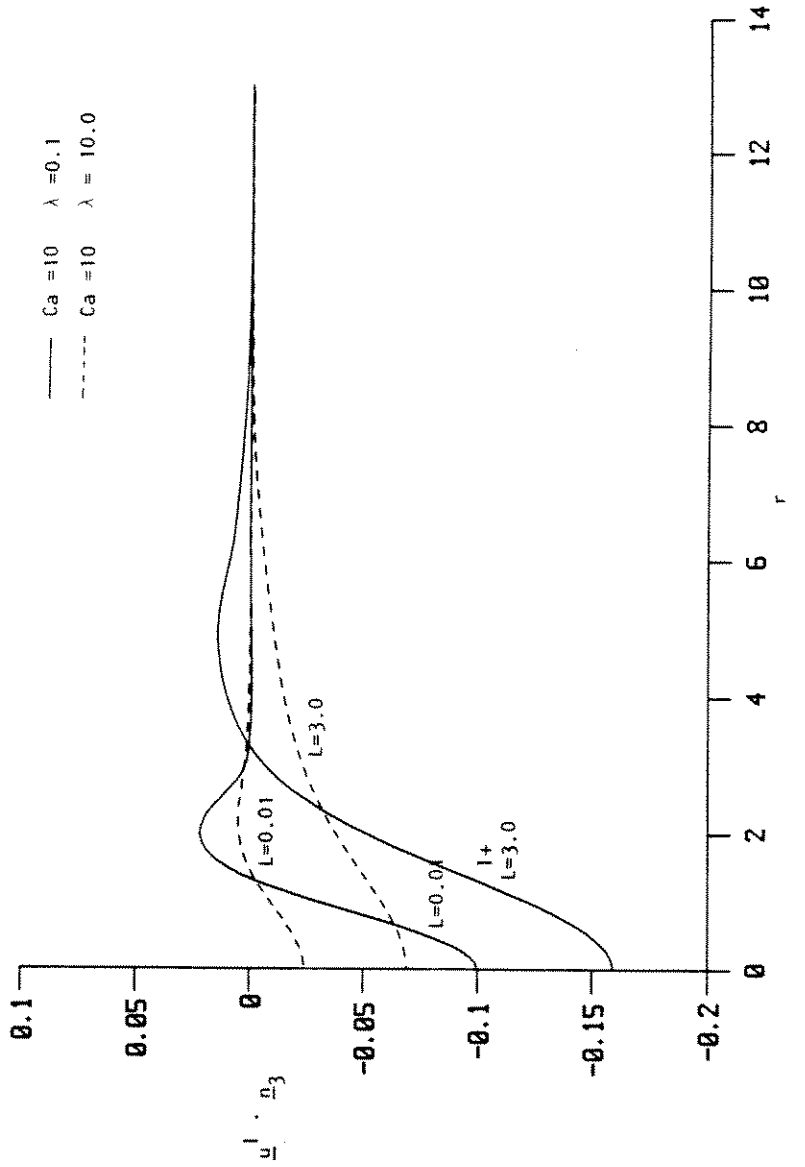
Ca =10 λ =0.1
Ca =10 λ = 10.0
L=0.01
L=3.0
L=0.01
L=3.0
0.1
0.05
0
-0.05
-0.1
-0.15
-0.2
0
2
4
6
8
10
12
14
r

Figure 5

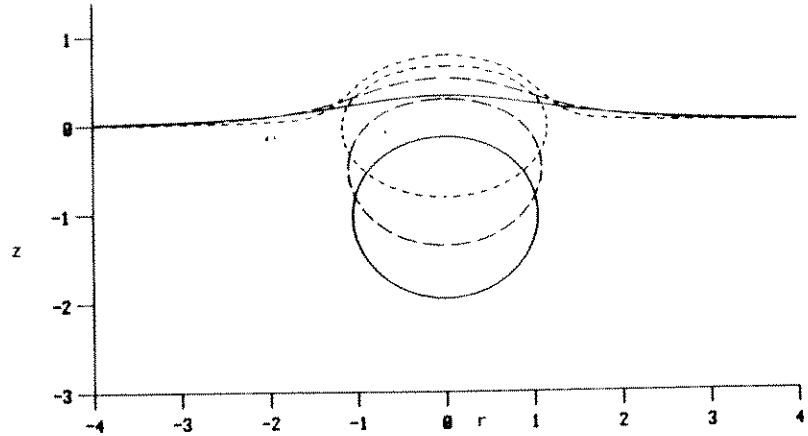

Calculated Shapes

Ca = 0.5 λ=5

(a)

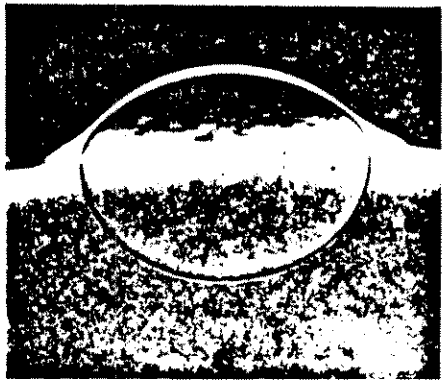

Hartland (1967b)

Ca = 0.507 λ = 4.76

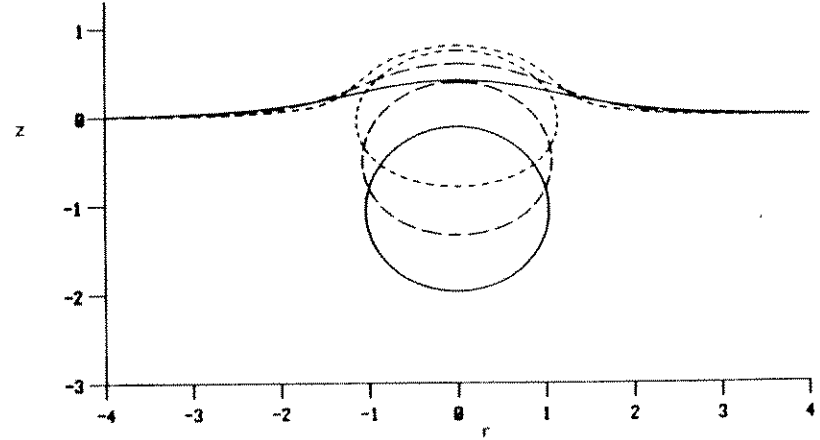

Calculated Shapes

Ca = 1 λ = 0.02

(b)

Figure 6

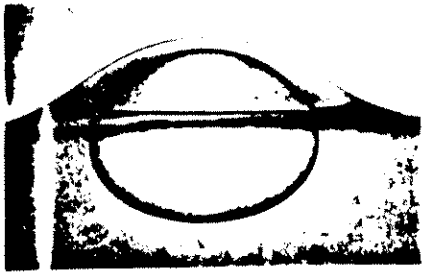

Hartland (1969)

Ca = 1.037 λ = 0.021

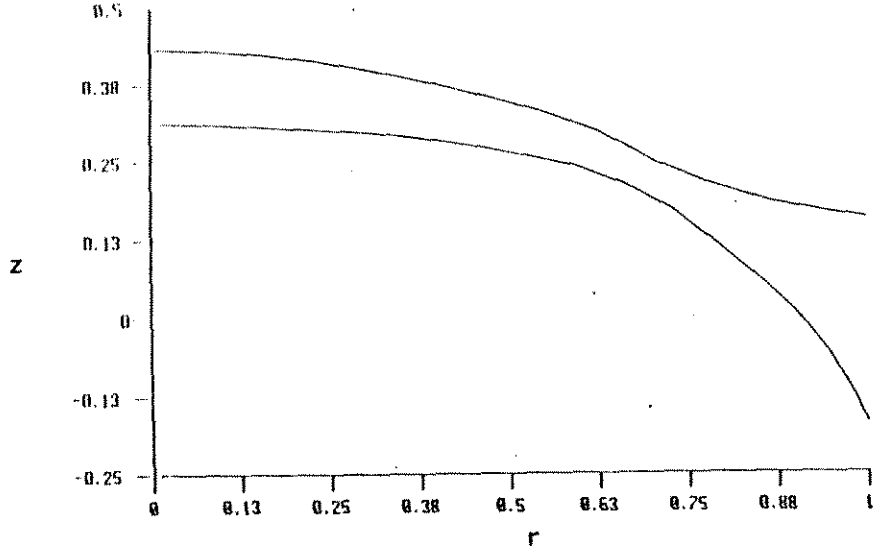

Calculated Shapes

Ca =0.05 λ = 30

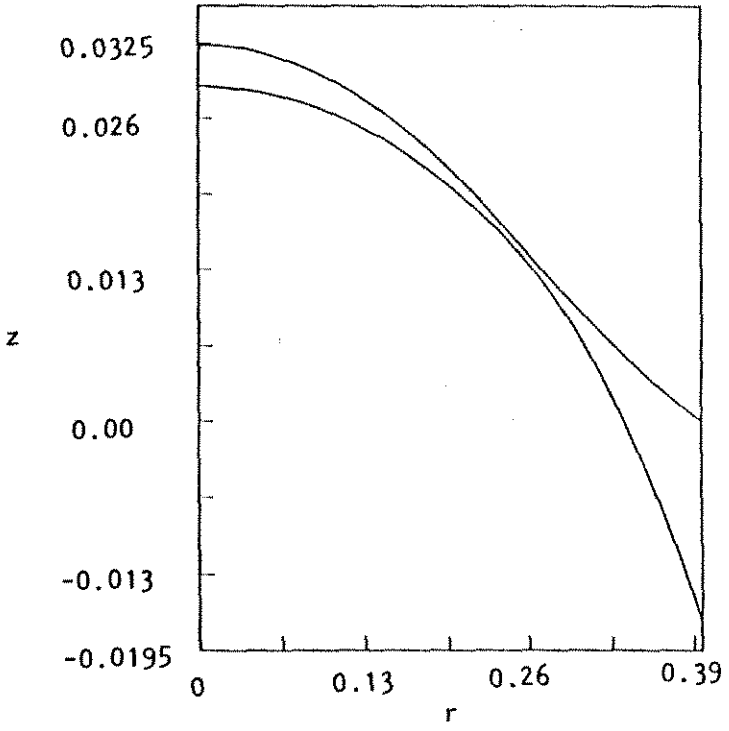

Lin and Slattery (1982)

Ca = 0.0109 λ = 32.8

Figure 7

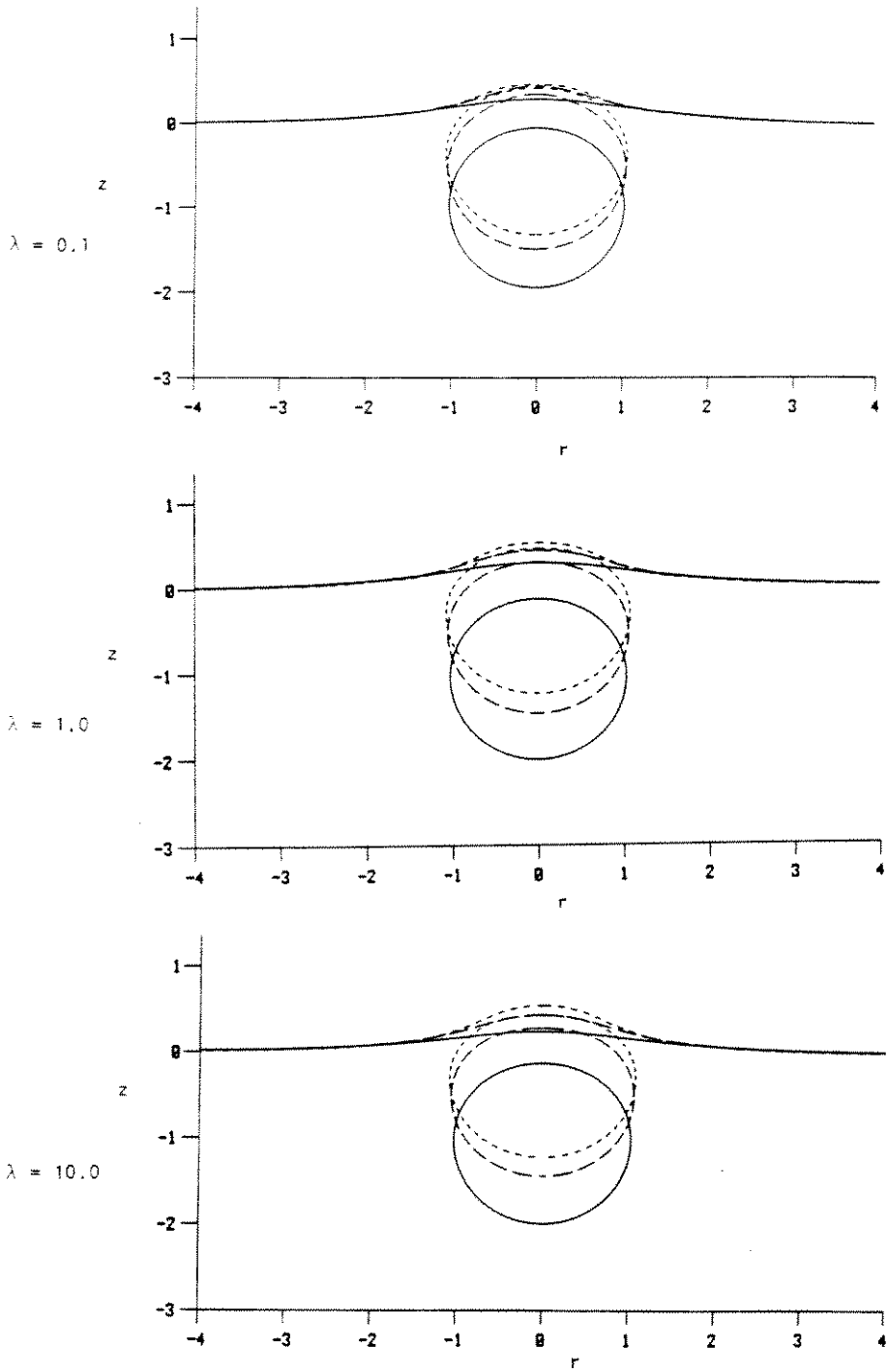

Ca = 0.2

Figure 8

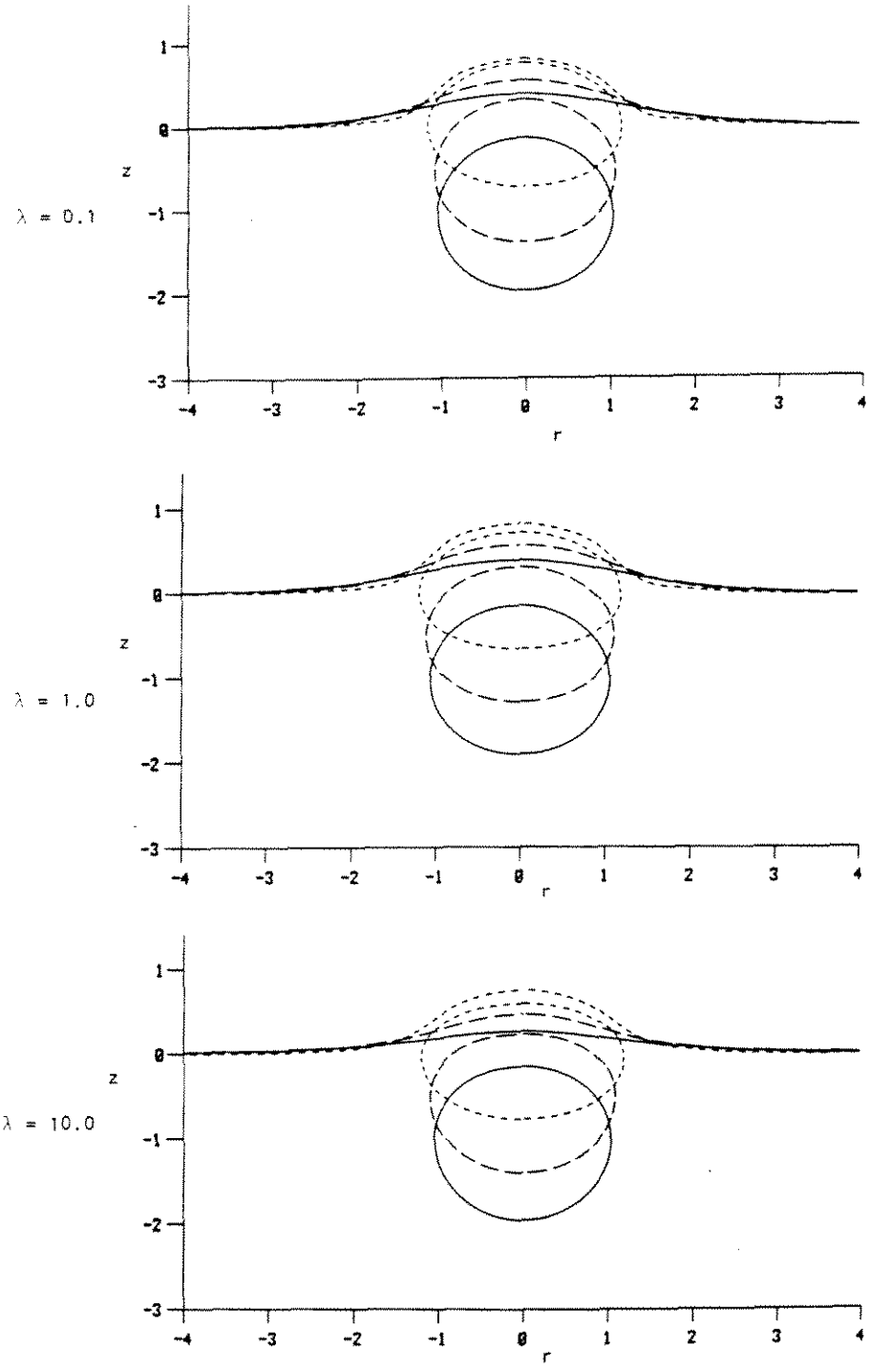

Ca = 1.0

figure 9

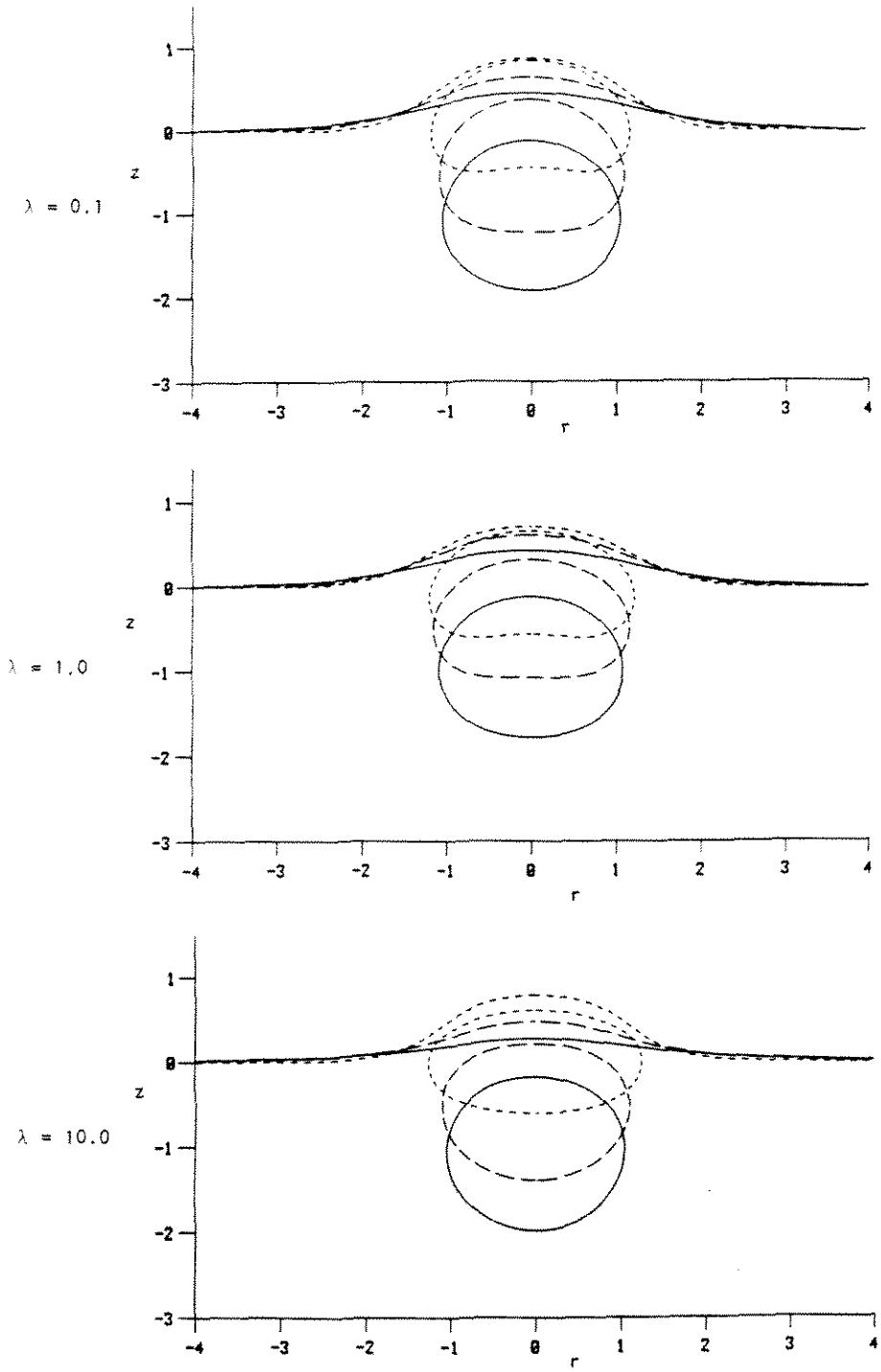

Ca = 10.0

Figure 10

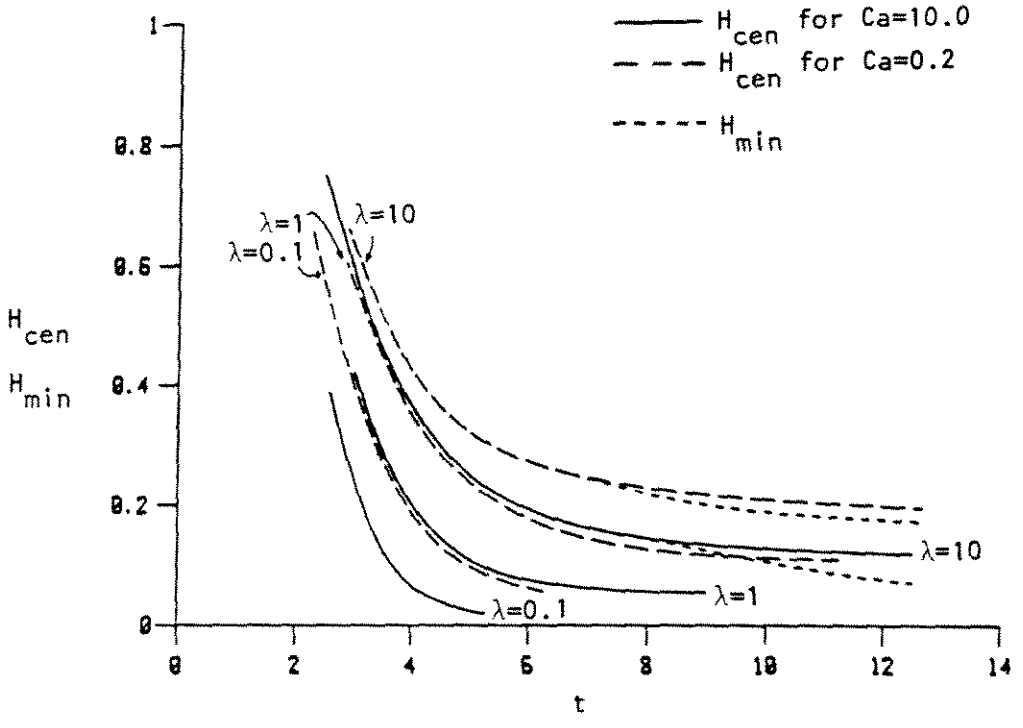
H cen for Ca=10.0
H cen for Ca=0.2
H min
λ=1
λ=0.1
λ=10
λ=10
λ=1
λ=0.1
H cen
H min
t
1
0.8
0.6
0.4
0.2
0
0
2
4
6
8
10
12
14

Figure 11

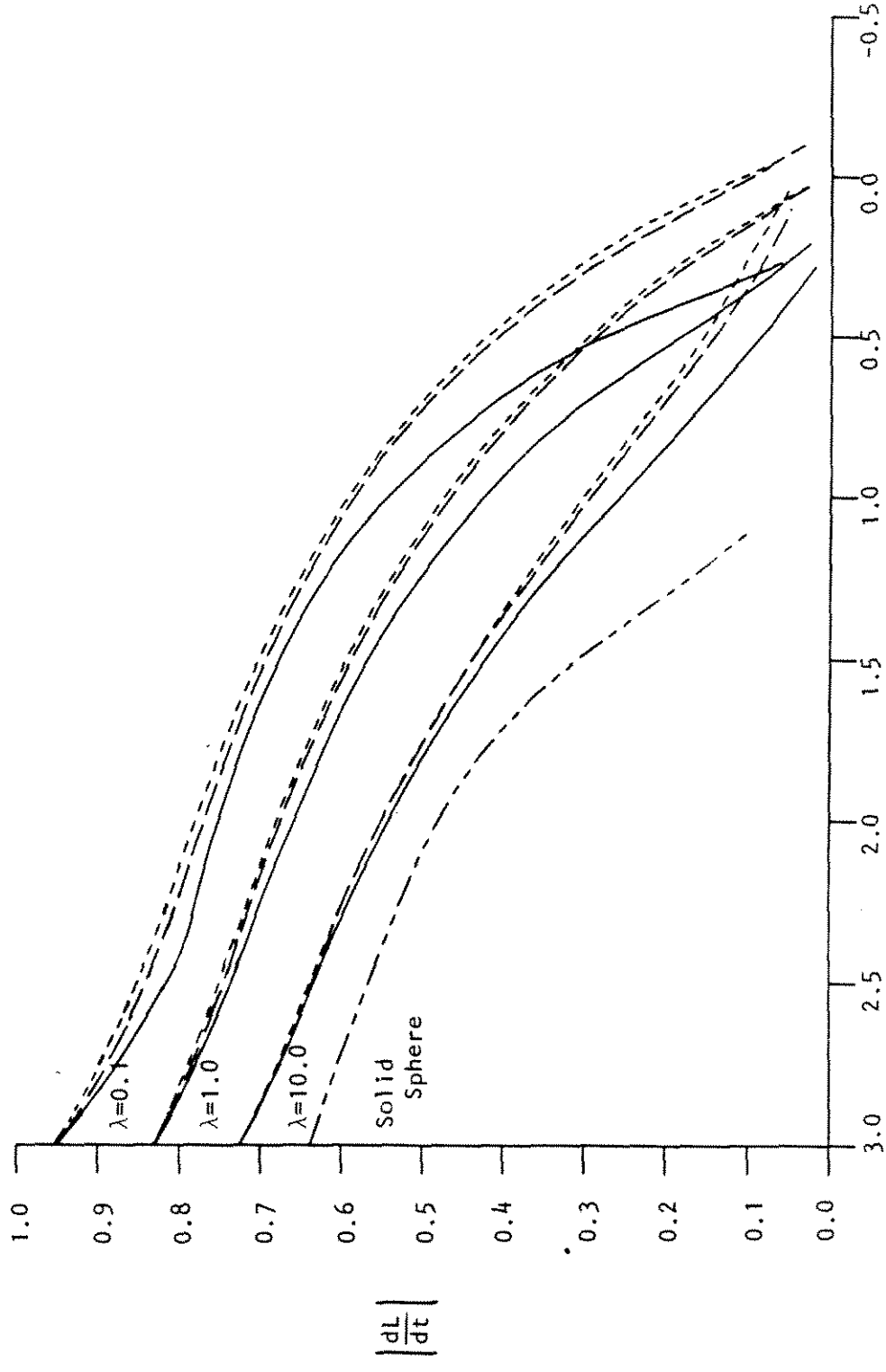
1.0
0.9
0.8
0.7
0.6
0.5
0.4
0.3
0.2
0.1
0.0
|dL/dt|
λ=0.1
λ=1.0
λ=10.0
Solid Sphere
3.0
2.5
2.0
1.5
1.0
0.5
0.0
-0.5
L

Figure 12